

Impacts of Asymmetric Supernova Explosions on Binary Populations and Gravitational Waves Archaeology



Jingqi Sun

Department of Physics
The University of Auckland

Supervisor: Associate Professor Jan Jamie Eldridge

A dissertation submitted in partial fulfilment of the requirements for the degree of BSc(Hons)
in Physics, The University of Auckland, 2022.

Abstract

We discuss impacts of asymmetric supernova explosions (SNe) on a theoretical binary population by analysing distributions and fitting observations. By adopting models and results of asymmetric SNe, an original study called gravitational waves (GW) archaeology are successfully constructed and investigations into GW archaeology are undertaken. We aim to develop a higher efficient method to compute simulations of asymmetric SNe, which are also known as the ‘kicks’. Base on a simplified version of the kick dynamical model constructed by Tauris & Takens in 1997, we investigate the dependence and relationships of kick parameters on a binary population generated by the BPASS model. We assume an isotropic distribution for kick orientations and a Maxwellian speed distribution with a Hobbs’ root-mean-square width $\sigma_w = 265$ km/s for the entire research. GW archaeology methods and programs are then advanced to match transient observations. We start by defining a GW permissible time τ , which combines the time for system formation, binary evolution and gravitational radiation, thus it measures the time from Big Bang to a GW event. Prior computations of τ generate a giant look-up table, we are then able to search for suitable τ s that coincide the look-back time of any specific GW transient. Analysis on multiple outcomes suggests kick orientation usually has maximum effects around 135° from the pre-SN orbital velocity \mathbf{v} . Statistics provide an IMF-weighted runaway probability $\sim 88\%$ for the theoretical binary population. Our results also suggest that a SN-dependent kick model would have higher observational consistencies. Matching results of GW archaeology can be summarised to a preferable kick speed 343.4 ± 88.7 km/s and a kick angle $143.5^\circ \pm 16.8^\circ$ from \mathbf{v} . We also find that the first or preexist compact remnants usually have higher probability to be the more massive object than the second or last supernova remnants (SNR) in most GW transient observations. The practicability of the prototypical program of GW archaeology is confirmed by several experimental verification, further developments are expected to significantly improve accuracy and efficiency of the program.

Contents

Abstract	1
1 Introduction	5
2 Models and Methods	7
2.1 Original Model	7
2.1.1 Pre-SN Stage	7
2.1.1.1 Basic parameters	7
2.1.1.2 Reference frame and coordinate system	7
2.1.2 SN-kicking Stage	8
2.1.2.1 The kick	8
2.1.2.2 Shell impact	8
2.1.2.3 Indicative parameters	9
2.1.3 Post-SN Stage	9
2.1.3.1 Unbounded systems	9
2.1.3.2 Bounded systems	10
2.1.3.3 Merged systems	10
2.2 Simplified Model	10
2.2.1 Assumptions	10
2.2.2 Reduced velocities with no dimension	11
2.3 Populations of the BPASS Model	12
2.4 Analysis Methodologies	12
2.4.1 Bounded threshold surface	12
2.4.2 Kick distributions	14
2.4.3 Bray & Eldridge kick model	14
2.4.4 Runaway probability	14
2.5 Gravitational Wave Archaeology	15
2.5.1 Mass constraints	15
2.5.2 Time constraints	15
2.5.2.1 Cosmological measurements of time	15
2.5.2.2 Gravitational decay time	16
2.5.2.3 Typical formation time	17
2.5.2.4 Combined constraints	17
2.5.3 Tabulation of GW permissible time under discrete kicks	18
3 Results and Analysis	21
3.1 Asymmetric Supernova Explosions on Binary Populations	21
3.1.1 Probability Distributions	22
3.1.2 Eccentricity Distributions	25
3.1.3 Velocity Distributions	26

3.2	Gravitational Wave Archaeology	28
3.2.1	Gravitational Decay Time	28
3.2.2	Events Matching Results	30
4	Discussion	35
4.1	Further Steps of Models	35
4.2	Further Steps of Methods	36
5	Conclusions	39
A	BPASS Populations	45
B	Additional Methods	51
B.1	Codes	51
B.2	Keep-only algorithm	51
B.3	Determination of true peaks of the formation time	51
B.4	Data reduction process of printed outcomes	52
C	All Plots of Distributions	55
D	Full Results of GW Archaeology	69

Chapter 1

Introduction

Asymmetric supernova (SN) explosions, also known as the ‘kicks’, are important for studying post-SN configurations and binary populations. Consider typical massive stars, for instance main sequence stars of initial masses about $8M_{\odot}$. After most of the hydrogen being exhausted in their dense cores, further nuclear reactions will keep burning the cores up to the production of heavier elements till iron group isotopes. In the meanwhile of core burning, density and temperature of the inner regions of the star keep increasing. When the central iron core continues to grow and approaches Chandrasekhar mass $M_{\text{ch}} \approx 1.4M_{\odot}$, two processes are active to lead to core-collapse: nuclear photodisintegration and neutronisation, which together transform almost all of nucleons to neutrons. Then a new born neutron star (NS) is formed in the core of the star, and the outer layers of matter fall onto the surface of this newly formed NS and give rise to an astrophysical shock wave that propagates outward and blows off the stellar outer shells [1]. These events are observed as supernova explosions (SNe). Due to complicated mechanisms of shocks, a SN may not be isotropically symmetric, so the net impact can create an additional velocity to a random direction on the NS, in which like a kick. In general cases, we call the compact remnant of the star as the supernova remnant (SNR). If the SNR mass exceeds the maximum allowed NS mass about $2.16M_{\odot}$, the SNR will further collapse to a black hole (BH) under complex mechanisms.

In binary systems, evolution of massive stars could get more complicated by involving accretion and mass transfer between the two stars, and the binary might experience SNe twice. If one star undergoes an asymmetric SN explosion, combined effects of sudden mass loss and additional velocity can disrupt their gravitational bounds. However, binaries still get chance to survive an asymmetric SN explosion under certain conditions. Orbits of naturally formed binaries can be circularised under gravity, if a binary survive its first SN, then its orbit is very likely to be eccentric and the orbital semi-major axis may also be changed. After sufficiently long time, the orbit may be circularised again, and the second SN would happen in most cases. If a binary is lucky enough to survive both SNe and become bounded binary compact objects (NS or BH), they are relatively stable, and will finally merge under losing of energy and momentum by gravitational radiation. At the last moment before they merge together, if they spin fast enough, this process can create a gravitational wave (GW) transient which will then spread to surrounding space-time. Through the life-time of binary stars, thus the study of asymmetric SNe can predict the destiny of a population of binary systems, and can also predict observations.

To describe and investigate the exact mechanism behind asymmetric supernova explosions (SNe), T. M. Tauris and R. J. Takens introduced their kick kinematics and dynamics in 1997. They published detailed calculations and analysis for disrupted binary systems in 1998 [2], and later in 1999 they published their research on survival cases for an observational example Circinus X-1 [3]. For purposes of this research project, we use a simplified version of the Tauris & Takens’ kick model by ignoring shell impacts and reducing velocity parameters. For purposes of analysing

particular impacts of the simplified kick model on a population of binary systems, we use the Binary Populations And Spectral Synthesis (BPASS) code v2.2 (Stanway & Eldridge, 2018 [4]). The BPASS code provides reliable simulations of binary stellar populations and evolution, from initial formation to supernova explosion. Binary populations that generated by the BPASS model will be adopted as our standard sample for the entire project.

Problems of efficiency arises from current developments of the BPASS model. Simulating asymmetric SNe at an acceptable level of precision is an essential mission for binary evolution models. Current simulations in BPASS are created by computing for millions of different kicks by conducting a Monte Carlo method to generate random kicks, and this methods require a huge amount of time to reach certain accuracy. For instance, it can take up to a few weeks of CPU time to fully simulate a binary configuration. We try to solve this issue by pre-computing specific astrophysical quantities of a large population under different combinations of kick conditions, to create a giant look-up table, so that we can search in these recorded values and find estimated ranges to narrow down simulating domains and avoid repeating computations.

To test our methodologies, we need to compare simulating results to observations. However, if the binary system was disrupted in a SN explosion, current technologies are not capable to trace two single stars back to an earlier binary phase. Thus, we have to focus on bounded survivors of SNe. Recent detection and observational confirmations of GWs and black holes provide exciting possibility to verify our models and methods by fitting those real events. Along with the idea of matching GWs in our binary population, we initiate and propose an original study called *gravitational waves archaeology*. Each GW transient observation has two key measurements, the masses of the two objects and the luminosity distance for where this event happened. By using the Λ CDM cosmological model, we can transfer the luminosity distance to a look-back time to find when the event happened in the history of the universe. Even though we are unable to obtain information directly from GW signals, we can select candidate systems by a time constraint. Since for SN survivors, different kicks can lead to different pre-SN separations and eccentricities, thus different gravitational decay time (the time interval required from SN event to merging). We combine the formation time (required for system forming from the Big Bang), the evolution time (required from system formation to SN event) and the gravitational decay time to create a GW permissible time τ . Then we try to coincide τ with the event look-back time, so we are able to find suitable binary systems that coincide GW masses with specific kicks that can cause the GW transient.

Due to limitation of resources and time available to this research project, models and programs of GW archaeology are basically prototypes, a lot of feasible developments and improvements can be taken as further steps. It is reasonable to expect future versions of GW archaeology programs reach much more higher accuracy and efficiency, and the study of GW archaeology can help astrophysicists to understand better on exact relationships between asymmetric supernova explosions, gravitational waves and binary evolution.

In Chapter 2, we explain our assumptions and models, construct methodologies and GW archaeology. In Chapter 3, we present significant results and plots by performing methods on models introduced in Chapter 2, key matching results of GW archaeology are also included. Chapter 4 are discussions of feasible developments which can improve accuracy and efficiency of further results, as well as suggestions on further investigations. The last Chapter 5 summarises results of Chapter 3 and confirm the successful construction of GW archaeology. Full contents of methods and results are attached in appendixes. Appendix A explain details of the binary population provided by the BPASS model, Appendix B give additional methods that can increase efficiency for some situations, Appendix C are all plots of Chapter 3 with detailed explanations and captions, finally Appendix D tabulates all matching results of GW transients in GWTC.

[words count estimate: 23,000]

Chapter 2

Models and Methods

2.1 Original Model

The reference model that we used for analysing asymmetric supernova (SN) explosions (the ‘kick’) in binaries was described in 1998 by Tauris and Takens[2] [3]. This dynamical model includes the geometry to describe the binary system as well as calculations of post-SN final configurations. For clarity, we separate the SN explosion event into three stage, pre-SN, SN-kicking and post-SN. In the pre-SN stage, the coordinate system and any initial conditions are introduced, with noticeable assumptions. In the SN-kicking stage, kinematics and mathematical descriptions of the kick is constructed, and any interactions caused by SNe are considered, we also define the indicative parameters that corresponding to different outcomes. In the final post-SN stage, we give the general and final status of the resulting systems for each cases, depends on different indicative parameters.

2.1.1 Pre-SN Stage

2.1.1.1 Basic parameters

One ideal binary system has a *primary star* (S_1) of mass M_1 and a *secondary star* (S_2) of mass M_2 . A typical S_1 is a He-star which will explode soon, and it will finally form a newborn neutron star (or other compact supernova remnants, SNR) with a mass M_{NS} through the asymmetric SNe. S_2 could be any massive singular star-like body, it could be another main-sequence star just like S_1 , or a compact remnant (e.g. a NS or BH) after another previous SN explosion. By approximation, S_2 will not experience any self stellar evolution during physical processes of the whole explosion. We also circularise the pre-SN orbit, that is, a circular orbit with a zero eccentricity. Thus, the separation r between S_1 and S_2 is a constant before the SN explosion. As a result, their relative velocity is given by the constant pre-SN orbital velocity $v = \sqrt{G(M_1 + M_2)/r}$, where G is the gravitational constant.

2.1.1.2 Reference frame and coordinate system

Our coordinate system of the pre-SN binary is illustrated in Figure 2.1. The origin of the Cartesian coordinates is defined by the location of S_1 . Let \mathbf{r} be the pre-SN position vector pointing to S_1 with respect to S_2 and \mathbf{v} be the pre-SN relative velocity vector of S_1 with respect to S_2 . Then the positive x -axis is defined by pointing in the same direction of \mathbf{v} and the positive y -axis is defined by pointing towards S_2 from S_1 , that is, $\mathbf{v} = v\hat{\mathbf{x}}$ and $\mathbf{r} = -r\hat{\mathbf{y}}$. Now the positive z -axis $\hat{\mathbf{z}} = \hat{\mathbf{x}} \times \hat{\mathbf{y}}$ is pointing in the same direction of the pre-SN orbital angular momentum, as $\mathbf{h} = \mathbf{r} \times \mathbf{v} = -r\hat{\mathbf{y}} \times v\hat{\mathbf{x}} = rv\hat{\mathbf{x}} \times \hat{\mathbf{y}} = rv\hat{\mathbf{z}}$. (In fact, one should start from defining $\hat{\mathbf{z}}$ since \mathbf{h} is always a constant vector in any reference frames for two-body motions.)

3D Illustration of the Coordinate System

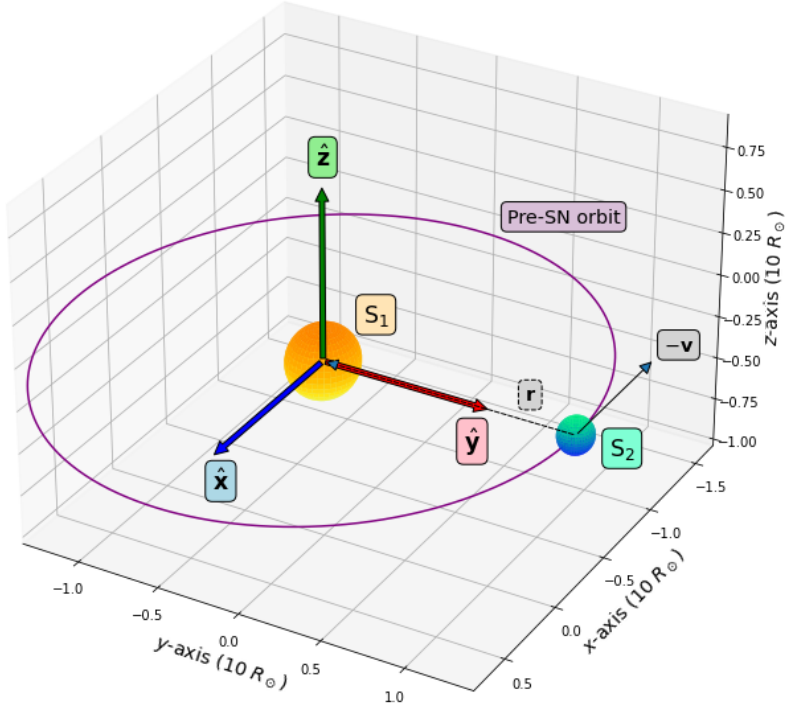


Figure 2.1: A 3D geometry of our reference frame and coordinate system. All plots are labeled and related by their colors. Here we assume S_1 is a star with a radius of two solar radii and S_2 has one solar radius, their separation is fifteen solar radii ($\log_{10}(r/R_\odot) = 1.176$). The scales of objects may not be consistent for all situations.

2.1.2 SN-kicking Stage

2.1.2.1 The kick

The kick can be now described in above Cartesian coordinates. By approximation, the mathematical result of an asymmetric SN can be simplified to a kick vector \mathbf{w} adding to the newborn NS, in the dimension of velocity. The magnitude or speed of the kick is $w = |\mathbf{w}|$. To determine the orientation of the kick vector, introduce two position angles, $\theta \in [0, \pi]$ and $\phi \in [0, 2\pi)$. θ is the angle between \mathbf{w} and \mathbf{v} , ϕ is the angle taken such that $w_y = w \sin \theta \cos \phi$. To relate polar and Cartesian representation of the kick vector, write down:

$$\mathbf{w} = (w_x, w_y, w_z) = (w \cos \theta, w \sin \theta \cos \phi, w \sin \theta \sin \phi). \quad (2.1)$$

2.1.2.2 Shell impact

Except direct effects caused by the asymmetric explosion, there could be further potential influences on S_2 as the explosion shell impact. For clarity, call the resulting S_2 after all exploding effects have been operated as the *companion star*, and label it as S_{2f} . One possible and remarkable difference between S_{2f} and S_2 is their masses, related by $M_{2f} = M_2(1 - F)$, where $F \in [0, 1]$ is a combined fraction of stripped and ablated mass of S_2 .

Similar to the kick, the shell impact can be mathematically simplified to a velocity vector $\mathbf{v}_{im} = v_{im}\hat{\mathbf{y}}$ adding to the companion star. Here v_{im} is *an effective speed taking into account the combined effects of incident shell momentum and the subsequent momentum resulting from*

mass loss owing to stripping and ablation of stellar material from the surface layers heated by the passing shock wave [2], and was estimated (Wheeler, Lecar & McKee 1975; see also Fryxell & Arnett 1981). In this research project, the full formula for calculating v_{im} and F will not be given, since it will be over-complicated to be added to our current simplified models.

2.1.2.3 Indicative parameters

Just after shell decoupling, the velocity vector of the newborn NS with respect to S_2 is:

$$\mathbf{u} = \mathbf{v} + \mathbf{w} - \mathbf{v}_{\text{im}} = (v + w_x, w_y - v_{\text{im}}, w_z) = (u_x, u_y, u_z). \quad (2.2)$$

Now one significant quantity is the mass ratio of final to initial total mass, defined by:

$$\tilde{m} \equiv \frac{M_{\text{post}}}{M_{\text{pre}}} = \frac{M_{\text{NS}} + M_{2f}}{M_1 + M_2} = \frac{1 + m_{2f}}{m_1 + m_2} \in (0, 1), \quad (2.3)$$

where the reduced mass is defined by $m_i \equiv M_i/M_{\text{NS}}$. With this mass ratio \tilde{m} , we can define the following principal indicative parameter:

$$\xi \equiv \frac{u^2}{\tilde{m}v^2} = \frac{v^2 + w^2 + v_{\text{im}}^2 + 2(vw_x - w_yv_{\text{im}})}{\tilde{m}v^2} \geq 0. \quad (2.4)$$

By analysing the orbital energy of the new binary system, the system will be disrupted if $\xi \geq 2$ and will remain to be bounded if $\xi < 2$. For simplicity, introduce two more quantities:

$$P \equiv \sqrt{\tilde{m}|\xi - 2|} \quad \text{and} \quad Q \equiv \xi - 1 - \frac{u_y^2}{\tilde{m}v^2} = \frac{(v + w_x)^2 + w_z^2}{\tilde{m}v^2} - 1. \quad (2.5)$$

Finally we are able to calculate the final eccentricity of the system:

$$e = \sqrt{1 + (\xi - 2)(Q + 1)}. \quad (2.6)$$

Note that, the eccentricity exists for both cases, even though it follows from orbital dynamics that $e > 1$ implies an unbounded hyperbolic orbit, but it still has physical significance.

2.1.3 Post-SN Stage

According to above definitions of the principal indicative parameter ξ , there are generally three cases for the final outcomes of a binary system that has been experienced an asymmetric SNe, to be unbounded ($\xi \geq 2$), to be still bounded ($\xi < 2$) or to be merged. In this section, we will give final astrophysical configurations for each cases.

2.1.3.1 Unbounded systems

In the case of disrupted binaries, $P = \sqrt{\tilde{m}(\xi - 2)}$ since $\xi - 2 \geq 0$. Two more quantities are defined for shortening the expressions:

$$R \equiv \left(\frac{Pu_y}{\tilde{m}v} + 1 - \xi \right) \frac{1 + m_{2f}}{m_{2f}} \quad \text{and} \quad S \equiv \frac{1 + m_{2f}}{m_{2f}} e^2. \quad (2.7)$$

Then we can write down the final velocities of the stellar components in the original reference frame as defined in Section 2.1.1.2. For the neutron star (i.e. \mathbf{u} at infinity):

$$\mathbf{v}_{\text{NS}} = \left[w_x \left(\frac{1}{R} + 1 \right) + \left(\frac{1}{R} + \frac{m_2}{m_1 + m_2} \right) v, w_y \left(1 - \frac{1}{S} \right) + \frac{1}{S} v_{\text{im}} + \frac{QP}{S} v, w_z \left(\frac{1}{R} + 1 \right) \right], \quad (2.8)$$

as well as for the companion star:

$$\mathbf{v}_{2f} = \left[\frac{-w_x}{m_{2f}R} - \left(\frac{1}{m_{2f}R} + \frac{m_1}{m_1 + m_2} \right) v, \frac{w_y}{m_{2f}S} + \left(1 - \frac{1}{m_{2f}S} \right) v_{\text{im}} - \frac{QP}{m_{2f}S} v, \frac{-w_z}{m_{2f}R} \right]. \quad (2.9)$$

2.1.3.2 Bounded systems

If the original binary system survives in the SN explosion, its new eccentricity $e < 1$ and its new semi-major axis is $a = r/(2 - \xi)$. The new critical orbital velocity (the post-SN equivalence of the pre-SN orbital velocity v) is given by:

$$v_c = \sqrt{\frac{G(M_{\text{NS}} + M_{2f})}{a}} = \sqrt{\frac{G(M_1 + M_2)}{r} \tilde{m}(2 - \xi)} = Pv. \quad (2.10)$$

By Kepler's third law, the period for this survival bounded system is:

$$T = 2\pi \sqrt{\frac{a^3}{G(M_{\text{NS}} + M_{2f})}} = 2\pi \frac{a}{v_c} = \frac{2\pi r}{Pv(2 - \xi)}. \quad (2.11)$$

It is able to find an additional velocity to the survival system, as a result of the conservation of momentum. Define a new mass ratio:

$$\tilde{M} = \frac{M_{\text{NS}}M_2 - M_1M_{2f}}{M_1 + M_2} \frac{1}{M_{\text{NS}}} = \frac{m_2 - m_1m_{2f}}{m_1 + m_2}, \quad (2.12)$$

then the change in momentum is:

$$\Delta \mathbf{p} = [\Delta p_x, \Delta p_y, \Delta p_z] = M_{\text{NS}}(\mathbf{w} + [\tilde{M}v, m_{2f}v_{\text{im}}, 0]). \quad (2.13)$$

Thus the systemic velocity of a binary which survives the SN is:

$$v_{\text{sys}} = |\mathbf{v}_{\text{sys}}| = \frac{|\Delta \mathbf{p}|}{M_{\text{NS}} + M_{2f}}. \quad (2.14)$$

2.1.3.3 Merged systems

There is another possibility if the system is not disrupted. If the perigee $q = a(1 - e)$ is not greater than the radius of the companion star, then the two stars will merge and the system will coalesce. However, the mergence case is an extreme event in the statistical sense, especially when we assume that the companion has already been a compact object in the simplified model.

2.2 Simplified Model

For purposes of effectively analysing, some simplifications of the above original model have to be taken based on further assumptions. Even some expressions have already been rearranged, further modifications are still needed to take place for reducing some parameters. Some constraints and applications of this simplified model are listed in Section 2.4.

2.2.1 Assumptions

The main simplification we take is to ignore the shell impact. It has two reasons. First, the calculation will be much more complicated if we import all considerations of the shell impact, the shell impact also has many complex parameters which we do not understand very well so far. Secondly, Tauris (1998[2]) also indicated that the shell impact only takes significant effects when the two stars of the original system get very closed before SN explosion, and this case is not considered as an ordinary situation for binary SNe. Hence, for a large sample of population, we can safely assume that the shell impact dose not take place for the majority of the population in our statistical analysis. Mathematically, we assume $v_{\text{im}} = 0$ and $F = 0$, thus $M_{2f} = M_2$. This is equivalent to assume that the companion star remains unchanged during the SN event.

We also assume that the resulting SNR of S_1 (which labeled as NS previously) could be more general types of compact remnant, like black holes. So now we can assume an S_1 with much more larger initial mass, and its compact remnant could be either a neutron star (NS) or a black hole (BH). And for clarity, we relabel the compact remnant as SNR_3 and its mass $M_3 = M_{\text{NS}}$. The denotation $m_i \equiv M_i/M_3$ will be kept using. As a summary, the initial parameters are collected into two sets of parameters, called the *binary system parameter set* $\mathbf{B} = \{M_1, M_2, r, M_3\}$ and the *kick parameter set* $\mathbf{w} = \{w, \theta, \phi\}$. Also notice that the mass ratios are now:

$$\tilde{m} = \frac{M_3 + M_2}{M_1 + M_2} \geq 0 \quad \text{and} \quad \tilde{M} = \frac{(M_3 - M_1)M_2}{(M_1 + M_2)M_3} \leq 0. \quad (2.15)$$

2.2.2 Reduced velocities with no dimension

Velocities play an important role in both indicative parameters and final configurations. However, the actually effective aspects of these velocities are their ratios to the pre-SN orbital velocity v , rather than their magnitudes in km/s. Thus, we would like to express all velocities in the unit of the pre-SN orbital velocity, as $\boldsymbol{\eta}_i \equiv \mathbf{v}_i/v$ and $\eta_i \equiv v_i/v$. We start from defining the reduced kick κ , as:

$$\kappa \equiv \frac{w}{v} = w\sqrt{\frac{r}{G(M_1 + M_2)}} \quad \text{and} \quad \boldsymbol{\kappa} = \begin{bmatrix} \kappa_x \\ \kappa_y \\ \kappa_z \end{bmatrix} = \kappa \begin{bmatrix} \cos \theta \\ \sin \theta \cos \phi \\ \sin \theta \sin \phi \end{bmatrix}. \quad (2.16)$$

Then the reduced velocity of the newborn compact SNR_3 is $\mathbf{u}/v = (1 + \kappa_x, \kappa_y, \kappa_z)$. Now the indicative parameters are reduced to:

$$\xi = \frac{1 + \kappa^2 + 2\kappa \cos \theta}{\tilde{m}} \quad \text{and} \quad Q = \xi - 1 - \frac{\kappa^2 \sin^2 \theta \cos^2 \phi}{\tilde{m}}. \quad (2.17)$$

For disrupted systems, we have:

$$R = \left(\frac{P\kappa_y}{\tilde{m}} + 1 - \xi \right) \frac{1 + m_2}{m_2} \quad \text{and} \quad S = \frac{1 + m_2}{m_2} e^2. \quad (2.18)$$

$$\boldsymbol{\eta}_3 \equiv \frac{\mathbf{v}_{\text{NS}}}{v} = \left[\kappa_x \left(\frac{1}{R} + 1 \right) + \frac{1}{R} + \frac{m_2}{m_1 + m_2}, \kappa_y \left(1 - \frac{1}{S} \right) + \frac{QP}{S}, \kappa_z \left(\frac{1}{R} + 1 \right) \right], \quad (2.19)$$

$$\boldsymbol{\eta}_2 \equiv \frac{\mathbf{v}_{\text{2f}}}{v} = \left[-\frac{\kappa_x + 1}{m_2 R} - \frac{m_1}{m_1 + m_2}, \frac{\kappa_y - QP}{m_2 S}, -\frac{\kappa_z}{m_2 R} \right]. \quad (2.20)$$

For survival systems, we have:

$$\frac{\Delta \mathbf{p}}{v} = M_3 (\boldsymbol{\kappa} + [\tilde{M}, 0, 0]) \quad \text{and} \quad \eta_{\text{sys}} \equiv \frac{v_{\text{sys}}}{v} = \frac{\sqrt{\kappa^2 + 2\kappa_x \tilde{M} + \tilde{M}^2}}{1 + m_2}. \quad (2.21)$$

In addition, for survival cases, we also need to investigate their final separations a as well as final eccentricities e , which depend only on ξ and Q . By inspection, the explicit variables of ξ and Q are \tilde{m} , κ , $\cos \theta$ and $\cos^2 \phi$, since we can write $\sin^2 \theta = 1 - \cos^2 \theta$. Thus we can replace θ and ϕ with $c_1 \equiv \cos \theta \in [-1, 1]$ and $c_2 \equiv \cos^2 \phi \in [0, 1]$ for all analysis except for $\boldsymbol{\eta}_2$ and $\boldsymbol{\eta}_3$. That is, the kick parameter set could be written as $\{\kappa, c_1, c_2\}$ for certain cases. Now the two indicative parameters become:

$$\xi = \frac{1 + \kappa^2 + 2c_1 \kappa}{\tilde{m}} \quad \text{and} \quad Q + 1 = \xi - c_2 \frac{\kappa^2 (1 - c_1^2)}{\tilde{m}}. \quad (2.22)$$

2.3 Populations of the BPASS Model

One further piece of information we require is how stars evolve in binary star systems. We use the Binary Populations And Spectral Synthesis (BPASS) code [4]. The BPASS code provides detailed simulations of binary stellar populations and follows their evolution until dying in such a supernova explosion. All population data [5] of binary systems we used in this project are generated by the BPASS model. The following is a list of key physical properties of a typical BPASS binary system:

- M_1/M_\odot : The mass of the primary star, just before the SN.
- M_2/M_\odot : The mass of the secondary star. Note that, for purpose of concentrating on single explosions, we assume all companion stars have already been compact objects.
- $\log_{10}(r/R_\odot)$: The separation of the binary in solar radii.
- M_3/M_\odot : The mass of the compact remnant of the exploded primary star.
- IMF: Initial mass function (IMF) weight, this is “the number of such binaries one would expect being born for a stellar population of total mass $10^6 M_\odot$ ”. This theoretical calculation is based on distribution models of Kroupa & Tout (1993 [6]) and Moe & Di Stefano (2017 [7]). In a nutshell, this quantity is a measure of the probability for such a system to exist in a galaxy.
- P : Period of the binary in days, just before the SN. This is equivalent to the separation r by Kepler’s third law.
- t_{evo} : Evolution age in million years, this is the time required from the binary initially forming to exploding. Typically, the evolution age is dozens of million years, and some is a few of million years. For the sample used in this project, $1 \text{ Myr} < t_{\text{evo}} < 100 \text{ Myr}$.
- Z : The initial metallicity of the star in mass fraction. We use discrete metallicities, as $Z \in \{0.00001, 0.0001, 0.001, 0.002, 0.003, 0.004, 0.006, 0.008, 0.01, 0.014, 0.02, 0.03, 0.04\}$.
- $M_{1,i}$: The initial mass of the primary star at the time of system formation.
- $M_{2,i}$: The initial mass of the companion compact object at the time of system formation.
- P_i : The initial period of the binary at the time of system formation.

Note that, some values like periods are not directly useful for computations, but they can give a more intuitive illustration of the properties of a binary system, or like the initial values which can help us understand formation history about a certain system when we trace back to them from recent observations. Samples of BPASS populations for each metallicity are attached in Appendix A according to their IMF weights.

2.4 Analysis Methodologies

By reducing parameters in the simplified model (2.2), we are able to conduct more analytical approaches to visualise the theoretical results. In this section, several methods will be explained. Furthermore, some additional methods are attached in Appendix B.

2.4.1 Bounded threshold surface

One useful outcome of our simplified model is that the principal indicative parameter ξ is now dependent only on initial inputs $\{\tilde{m}, \kappa, c_1\}$. As we have stated above, $\xi = 2$ is a boundary for whether the binary will survive the asymmetric SNe or not. Since there are only three parameters

to determine this general result, we are able to sketch the level surface $\xi(\tilde{m}, \kappa, c_1) = 2$, or equivalently, $1 + \kappa^2 + 2c_1\kappa = 2\tilde{m}$, for $0 < \tilde{m} < 1$, $-1 \leq c_1 \leq 1$ and $\kappa \geq 0$. Figure 2.2 is the 3D plot of this level surface. In this 3D space, every point represents a binary system of \tilde{m} with a kick speed κ and an orientation indicator c_1 .

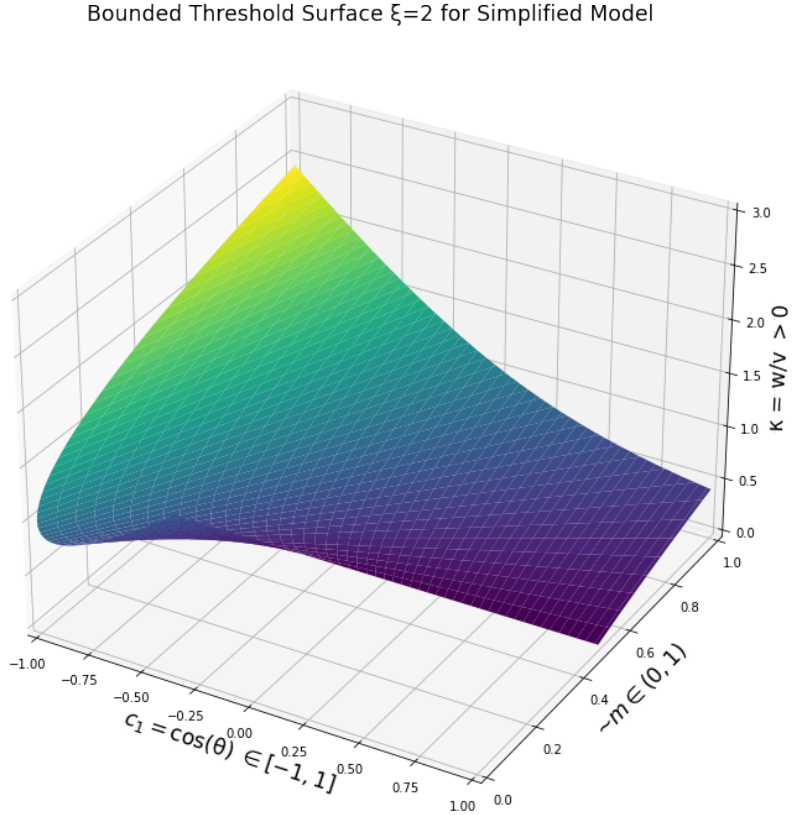


Figure 2.2: A 3D sketch of the threshold surface. Spaces inside the surface represent all binaries which will be still bounded after such a SN explosion, and everywhere else, including points on the surface, represent all unbounded systems.

As we can see, allowed κ reaches a maximum value at $\tilde{m} = 1$ and $c_1 = -1$, which has an analytical value of $\kappa_{\max} = 1 + \sqrt{2} \approx 2.414$. This means, for any binary system, if it has a kick with a magnitude $w > 2.414v$, then it must be disrupted. Another interesting phenomenon happens when $c_1 = \cos\theta < 0$ (i.e. $\theta \in [90^\circ, 180^\circ]$) and $\tilde{m} < 0.5$. In this quadrant, the lower bounds of κ for survival systems are no longer zeros, but are greater than zeros. The physical interpretation here is, when a kick vector has components in the opposite direction of the pre-SN orbital velocity \mathbf{v} , it requires an appropriate kick to keep the system being bounded, a smaller kick may not be sufficient to sustain the momentum to stay in the system.

Alternatively, if the binary parameter set \mathbf{B} is known, then we are able to find its threshold (maximum value to be bounded) kick w_{\max} . w_{\max} is the kick magnitude when assuming $\theta = 180^\circ$ and reaching $\xi = 2$. Theoretically, this is the maximum kick speed for a system with a certain \mathbf{B} , that can survive after it. In terms of \mathbf{B} , it is given by:

$$w_{\max}(\mathbf{B}) \equiv (1 + \sqrt{2\tilde{m}})v = \sqrt{G \frac{M_1 + M_2}{r}} + \sqrt{2G \frac{M_2 + M_3}{r}}. \quad (2.23)$$

2.4.2 Kick distributions

In practice, knowing the parameter set \mathbf{B} by observations or population models is not sufficient to predict the exact values of \mathbf{w} . However, if we assume the kick is not totally random but obeys basic physical laws, we can know some possible distributions for the parameter \mathbf{w} . It is easy to find certain distributions for angles if we assume the orientation of the kick is isotropic, i.e. distributes evenly on the sphere:

$$\Theta(\theta) d\theta = \frac{\sin \theta}{2} d\theta \quad \text{and} \quad \Phi(\phi) d\phi = \frac{1}{2\pi} d\phi. \quad (2.24)$$

For kick speeds w , we can use a Maxwell-Boltzmann (MB) distribution of speeds:

$$D(w, \sigma_w) dw = \sqrt{\frac{2}{\pi}} \frac{w^2}{\sigma_w^3} \exp\left(-\frac{w^2}{2\sigma_w^2}\right) dw, \quad (2.25)$$

where σ_w is the root-mean-square width. One suitable value is known as the “Hobbs’ kick” (G. Hobbs & D. R. Lorimer etc., 2005 [8]), which provides a specific value $\sigma_w = 265$ km/s.

2.4.3 Bray & Eldridge kick model

One recent study (Bray & Eldridge 2018 [9]) of neutron star kick suggests a simple kick formula:

$$v_{\text{kick}} = \alpha \left(\frac{M_{\text{ejecta}}}{M_{\text{remnant}}} \right) + \beta = \alpha \left(\frac{M_1 - M_3}{M_3} \right) + \beta = \alpha(m_1 - 1) + \beta. \quad (2.26)$$

Here α and β are two constants to be determined. The suggested values by Bray & Eldridge are $\alpha = 100$ km s⁻¹ and $\beta = -170$ km s⁻¹. This kick formula provides a feasible approach to remove the kick magnitude w , for purposes of analysing some certain situations. Since it is a SN-dependent kick, it might also be used as the root-mean-square width σ_w for the MB distribution, as a comparison to the Hobbs’ kick. Furthermore, we are also going to take several combinations of α and β to test the “Bray’s kick” with the simplified model combined with populations of the BPASS model.

2.4.4 Runaway probability

With above kick distributions, for any given initial parameter set \mathbf{B} , one can calculate the overall runaway probability, which is the chance for any random kick that obeys above distributions for the particular system with \mathbf{B} to be disrupted.

First of all, given both \mathbf{B} and \mathbf{w} , by using the model, one can certainly know whether the system will be disrupted or not. If $\xi \geq 2$, the probability for the system being unbounded after the explosion is 100%, and if $\xi < 2$, it is impossible to be a disrupted binary. This fact can be formulated by a Heaviside step function:

$$P_0(\mathbf{B}, \mathbf{w}) = H(\xi(\mathbf{B}, \mathbf{w}) - 2) = \begin{cases} 1, & \text{if } \xi \geq 2, \\ 0, & \text{if } \xi < 2. \end{cases} \quad (2.27)$$

Then, we can integrated over the kick distributions to find the weighted chance:

$$P(\mathbf{B}) = \int_0^\infty \int_0^\pi \int_0^{2\pi} P_0(\mathbf{B}, \mathbf{w}) \Phi(\phi) d\phi \Theta(\theta) d\theta D(w, \sigma_w) dw. \quad (2.28)$$

Since the angle ϕ is evenly distributed over $[0, 2\pi]$ as well as our simplified ξ is independent of ϕ , the integral over ϕ should be removed. In practice, when we conduct numerical integration for a MB distribution, we don’t have to integrate it till ∞ , an upper bound of a few σ_w shall

be sufficient. Here we choose $6\sigma_w \approx 1590$ km/s, which is about the speed of the fastest neutron star known. Now the above triple integral is reduced to the following double integral:

$$P(\mathbf{B}) = \frac{1}{\sqrt{2\pi}} \frac{1}{\sigma_w^3} \int_0^{6\sigma_w} \int_0^\pi H(\xi - 2) \sin \theta \, d\theta \, w^2 \exp\left(\frac{-w^2}{2\sigma_w^2}\right) \, dw. \quad (2.29)$$

Using this formula, we can find the runaway probability for any set \mathbf{B} . Given a specific population of \mathbf{B}_{pop} (an array-like object of sets \mathbf{B}) with a normalised statistical weight W_{pop} (array-like), the overall runaway probability of the population is computed by the following dot product:

$$P_{\text{pop}} = P(\mathbf{B}_{\text{pop}}) \cdot W_{\text{pop}}. \quad (2.30)$$

In our practice, we use the BPASS model, and the typical W_{pop} is the IMF weight.

2.5 Gravitational Wave Archaeology

We want compare our models and results with observations. However, for disrupted binaries, it is almost impossible to trace two faraway stars back to a bounded binary system, as most single stars seem unconnected. Although a recent research [10] in 2021 confirms only one unbounded binary, known as HD 37424, that has been successfully traced back to its initial bounded configuration. Fortunately, we can work on the binaries that remain bounded, especially the many current detection of gravitational wave (GW) events, which are certainly constituted by two compact objects (NS or BH), and they must be compact remnants created in SNe. Hence, one important application of our model is to determine for GW transients and find the most likely binary in our population model with certain kicks that can finally cause the event that we detected. We call this original study as the *gravitational wave archaeology*, as we are inferring the initial configurations of binaries via present observations.

For each GW transient detection, there are three most important measurements, the masses of the two compact objects, say $M_a|_{-\sigma_a}^{+\sigma_A}$ and $M_b|_{-\sigma_b}^{+\sigma_B}$ (without loss of generality, assume $M_a \geq M_b$), and the event luminosity distance d_L in Mpc as well as their error bars σ_i .

2.5.1 Mass constraints

One essential but simple constraint we could immediately apply on our binary population for fitting a certain GW detection is mass. Recall that we suppose all companion S_2 of our binary population are already NS or BH. Then for all \mathbf{B} , both M_2 and M_3 represent the masses of some NS or BH. Let $m_a = \max\{M_2, M_3\}$ and $m_b = \min\{M_2, M_3\}$, to ensure that $m_a \geq m_b$. Now we can search in our population for which $M_a - \sigma_a < m_a < M_a + \sigma_A$ and $M_b - \sigma_b < m_b < M_b + \sigma_B$. In the other words, find all binary systems whose $\{M_2, M_3\}$ coincide $\{M_a, M_b\}$. A few successful matching candidates for any GW observations are expected with a sufficiently large sample of binary populations.

2.5.2 Time constraints

To narrow down the candidates from mass-constraint selection, a further complicated constraint which also involve kick parameters is necessary to be constructed. Measured luminosity distances are also useful. In this subsection, a few pivotal time nodes will be introduced to create a strict limitation.

2.5.2.1 Cosmological measurements of time

In modern cosmology, the Λ CDM model implies an expanding universe, which is confirmed by many observations. Thus, the luminosity distance d_L cannot be used directly with the speed of

light c to find when the detected event actually happened in the history of the universe. We must integrate over the history of the universe to determine the look-back time t_{LB} .

Physical cosmology relates the luminosity distance with the red-shift z of an observed event and energy density parameters of ingredients of the universe [11], as :

$$d_L(z) = (1+z)d_M(z) = (1+z)\frac{c}{H_0} \int_0^z \frac{dz'}{E(z')}, \quad (2.31)$$

where H_0 is the Hubble constant and:

$$E(z) \equiv \frac{H(z)}{H_0} = \sqrt{\Omega_{r,0}(1+z)^4 + \Omega_{m,0}(1+z)^3 + \Omega_{k,0}(1+z)^2 + \Omega_{\Lambda,0}}, \quad (2.32)$$

where $\Omega_{i,0}$ is the present density parameter of ingredient i. Specifically, r for radiation, m for matter (including dark matters), k for space-time curvature and Λ for a cosmological constant (i.e. dark energy). In most cosmological models, we can safely ignore radiation and curvature, set $\Omega_{r,0} = 0 = \Omega_{k,0}$. For other cosmological parameters, the Planck 2018 results VI [12] provides recently published measurements. We shall use values in the last column (TT,TE,EE+lowE+lensing+BAO) of Table 2 of that paper. They are:

- Hubble constant: $H_0 = 67.66 \pm 0.42 \text{ km s}^{-1} \text{ Mpc}^{-1}$.
- The age of the universe: $t_{\text{uni}} = 13.787 \pm 0.020 \text{ Gyr}$.
- Present density parameters: $\Omega_m = 0.3111 \pm 0.0056$ and $\Omega_\Lambda = 0.6889 \pm 0.0056$.

These values will be used henceforth. Now $E(z) = \sqrt{0.3111(1+z)^3 + 0.6889}$. The look-back time corresponding to a certain red-shift z is [11]:

$$t_{\text{LB}}(z) = \frac{1}{H_0} \int_0^z \frac{dz'}{(1+z')E(z')} \quad (2.33)$$

This t_{LB} is the actual time when the event happens. Even though there is no analytical solution to express $z(d_L)$, via the one-to-one relations of $d_L \mapsto z \mapsto t_{\text{LB}}$, we are able to find a numerical fit of $t_{\text{LB}}(d_L)$, for a specific range of d_L . In practice, we use a 12th order polynomial to fit $t_{\text{LB}}(d_L)$ for $d_L < 10 \text{ Gpc}$, this is greater than the maximum luminosity distance of observed GW transients so far.

2.5.2.2 Gravitational decay time

In 1964, P. C. Peters published a landmark study (Phys.Rev.136, B1224 [13]) outlining the mechanisms for the radiation of GWs. As a subsequent event after the asymmetric SNe, if after the explosion the binary is still bounded, and both S_2 and SNR_3 are compact objects (NS or BH), we are able to find their gravitational decay time T_{GD} for which they will merge due to loss of energy and angular momentum after this time. For a circular orbit, the decay time is given by $T_c = a^4/(4\beta)$, where:

$$\beta = \frac{64}{5} \frac{G^3 m_a m_b (m_a + m_b)}{c^5} \approx 1.2356 \times 10^{19} \left(\frac{m_a}{M_\odot} \right) \left(\frac{m_b}{M_\odot} \right) \left(\frac{m_a + m_b}{M_\odot} \right) \text{ m}^4 \text{ s}^{-1}. \quad (2.34)$$

For eccentric cases, we can use the recently published analytical fit (I. Mandel, 2021 [14]):

$$T_{\text{GD}} \approx T_c (1 + 0.27e^{10} + 0.33e^{20} + 0.2e^{1000}) (1 - e^2)^{7/2}. \quad (2.35)$$

Given initial parameter sets \mathbf{B} and \mathbf{w} , we are able to tell when systems are still bounded. When this is the case, we can exactly calculate their new separation a and new eccentricity e . Thus, in the context of our simplified model, this gravitational decay time can be written as $T_{\text{GD}}(\mathbf{B}, \mathbf{w})$.

2.5.2.3 Typical formation time

One consensus of modern cosmology is that the stellar formation did not start immediately after the Big Bang, so it requires a formation time t_{for} for our binaries to initially formed after the Big Bang. This time can be indicated by metallicity Z . The FIRE simulations (the Milky Way on Feedback in Realistic Environments [15]) provide mass distributions of stars formed at different metallicities in discrete time bins. There is no simple one-to-one relations between metallicities and formation time, and it will be over-complicated to use multiple distributions, thus we approximate the formation history to typical formation time points $T_{\text{for}}(Z)$ by concentrating each distribution to a single peak value, for each discrete metallicity. The method of finding the true peaks from discrete time bins is explained in Appendix B.3. Approximations for each metallicity are tabulated below.

Z	0.00001	0.0001	0.001	0.002	0.003	0.004	0.006
$T_{\text{for}}/\text{Gyr}$	12.530	12.235	11.014	9.986	9.764	9.475	9.190
Z	0.008	0.010	0.014	0.02	0.03	0.04	-
$T_{\text{for}}/\text{Gyr}$	8.563	7.959	7.474	6.051	4.806	3.576	-

Note that, this $T_{\text{for}}(Z)$ is not the time needed from the Big Bang to system formation, but is the time from system formation to now, related by $T_{\text{for}}(Z) = t_{\text{uni}} - t_{\text{for}}(Z)$. Henceforth with this format, we can abandon the universal age t_{uni} , but replace it by $T_{\text{for}}(Z)$ as a metallicity-dependent maximum allowed time for any astrophysical event in binary systems.

2.5.2.4 Combined constraints

Now with calculations of all major epochs, we can see how to combine these time nodes into a single constraint. Define a new GW permissible time $\tau = T_{\text{for}}(Z) - T_{\text{GD}}(\mathbf{B}, \mathbf{w}) - t_{\text{evo}}$, this is a kind of maximum time allowed for a GW event to occur. Figure 2.3 is an illustration of the time line of key events and pivotal time intervals for a typical binary evolution.

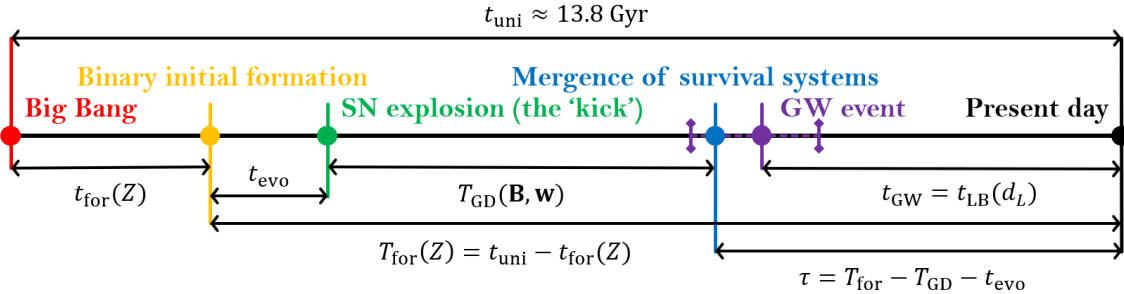


Figure 2.3: Illustration of the binary evolution time line. The yellow, green and blue events are corresponding to a binary system on the history, and the purple time point is a GW event with an error bar of the same color, which is determined by measurements.

According to above time line, given a specific GW event with a luminosity distance d_L , apparently, in order to match the event in our binary populations, candidate systems must satisfy both the mass constraints and the time coincidence $\tau \sim t_{\text{LB}}(d_L)$. In practice, an observed GW event usually has an error bar in its luminosity distance, and after transferring this error bar into a look-back time interval $[t_{\min}, t_{\max}]$, we are able to get a strict time constraint as $t_{\min} \leq \tau \leq t_{\max}$. In some extreme cases, for instance a nearby GW event, the distance error bar is very narrow, and in these cases it is also acceptable to use only $\tau \geq t_{\min}$ for our matching.

In summary, this time constraint can be written as $\tau \gtrsim t_{\text{LB}}(d_L)$. As an instruction, after mass selection, we firstly conduct a search for these candidate systems with different kick parameters

that satisfy $\tau \in [t_{\min}, t_{\max}]$. Then, if no outcome is produced, we will then try to remove the constraint $\tau \leq t_{\max}$ to perform a wider retrieval. Finally, we record all (\mathbf{B}, \mathbf{w}) combinations that satisfy $\tau \gtrsim t_{LB}(d_L)$.

2.5.3 Tabulation of GW permissible time under discrete kicks

In order to efficiently match a GW measurement in binary populations, we construct a method of pre-computing τ s for each theoretical binary system under different combinations of kick parameters. In fact, for any given system with \mathbf{B} , we can sketch a three dimensional level surface $\tau(\mathbf{B}, \mathbf{w}) = t$ for some time t , just like what we have done in Section 2.4.1. The 3D solid contains all kicks which can lead to bounded cases of which will merge under gravitational radiations in the given time limit $t \leq \tau$. However, when we do analysis on a large sample of population, it will take unacceptably excessive time to search in the complex 3D solid. Alternatively, to balance efficiency and accuracy, we will instead use discrete combinations of \mathbf{w} .

We first partition the kick parameters $\mathbf{w} = \{c_1, c_2, w\}$ into continuous intervals, and select intermediate values as representatives. Then we calculate the normalised weights corresponding to each partition by integrating over their intervals. We may also select minimum and maximum values of kick parameters as representative values, and for these cases we will calculate their one-side weights. Then for all possible combinations of those representatives of kick parameters (c_1, c_2, w) , we calculate their multiplied equivalent weights, then we compute τ values for each system in our binary population under these parameter combinations. Finally, we tabulate the recorded values of τ , where each column is corresponding to a combination of (c_1, c_2, w) , and each row is corresponding to a binary system. The final giant matrix constitutes a look-up table of τ . With this table, for any GW observations, we can screen τ s that satisfy appropriate condition $\tau \gtrsim t_{LB}(d_L)$, and trace rows and columns back to see which binaries with which kicks can lead to this GW event, as well as their combined weights (IMF+kick).

We start from $c_1 = \cos \theta \in [-1, 1]$. Since we will use c_1 rather than θ , we partition c_1 into intervals of 0.25, as shown as in the following table. Here the index relation is $c_1 = 1 - 0.25n_\theta$.

n_θ	0	1	2	3	4	5	6	7	8
θ	0°	41.4°	60°	75.5°	90°	104.5°	120°	138.6°	180°
c_1	1	0.75	0.5	0.25	0	-0.25	-0.5	-0.75	-1
W_n	6.25%	12.5%	12.5%	12.5%	12.5%	12.5%	12.5%	12.5%	6.25%

Note that, since $D(\theta) = \frac{1}{2} \sin \theta$, when calculating weights with respect to $c_1 = \cos \theta$, we get an even distribution. For ϕ , since the only explicitly dependent term of ϕ is $c_2 = \cos^2 \phi$, and c_2 values only have one-to-one relations in the interval $[0, \pi/2]$. Thus when trace back actual values of ϕ , we can only get a family of ϕ , denoted by $\phi^* \in [0^\circ, 90^\circ]$ and related by $\phi = n180^\circ \pm \phi^*$, where n is any integer. The index relation is $c_2 = 0.25n_\phi$ and the table is below.

n_ϕ	0	1	2	3	4
ϕ^*	90°	60°	45°	30°	0°
c_2	0	0.25	0.5	0.75	1
W_n	23%	19%	16%	19%	23%

When computing the distributions of the kick speed, we might meet a problem of the undetermined root-mean-square width σ_w . Although we can use the Hobbs' kick $\sigma_w = 265$ km/s, further observations and different models may suggest a different value. To eliminate this effect, we will express all kick speed w in units of the MB rms width σ_w . Due to the property of the MB distribution, the integrated weights are constant in the unit of σ_w and independent of choices of σ_w . To see this, let $s = w/\sigma_w$, it follows that $ds = dw/\sigma_w$. Then the distribution becomes $D(s) ds = \sqrt{2/\pi} s^2 e^{-s^2/2} ds$. When integrate in any interval $[a, b]$ with respect to s , it

is equivalently doing integral of the original MB distribution on $[a\sigma_w, b\sigma_w]$, and integration on $D(s)$ is independent of our choice of σ_w . In our practice, we choose an interval of $0.5\sigma_w$, so the index relation is $w = 0.5n_w\sigma_w$ and the table is below.

n_w	0	1	2	3	4	5	6	7	8	9
w/σ_w	0	0.5	1.0	1.5	2.0	2.5	3.0	3.5	4.0	4.5
W_n	0.41%	9.10%	23.7%	28.6%	21.5%	11.1%	4.16%	1.15%	0.24%	0.04%

We want to construct an algorithm to encode (n_θ, n_ϕ, n_w) to the columns of our look-up table. One simple algorithm is $n(n_\theta, n_\phi, n_w) = 50n_\theta + 10n_\phi + n_w$, and its inverse can be given by:

$$\begin{bmatrix} n_w \\ n_\phi \\ n_\theta \end{bmatrix}(n) = \begin{bmatrix} \langle n \rangle_{10} \\ \langle n - n_w \rangle_{50}/10 \\ (n - n_w - 10n_\phi)/50 \end{bmatrix}, \quad (2.36)$$

where $\langle x \rangle_y$ stands for $x \bmod y$, i.e. the remainder of x dividing y . Now we have both a binary system index n_p of the populations in the rank of their IMF weight as well as a kick index n_k where any n_k is corresponding to a certain kick with some (c_1, c_2, w) . Now assign n_p to be the row index and n_k be the column index. Since each coordinate (n_p, n_k) is corresponding to some known (\mathbf{B}, \mathbf{w}) , we can calculate and print a giant $n_p \times n_k$ matrix of entries τ .

In practice, if an entry (n_p, n_k) is corresponding to a runaway system, which has no τ , or a survival system with a negative value of τ , we will set them to an "not a number" ("nan") entry by a `Keep_Only` algorithm, as explained in Appendix B.2. Keeping positive numbers needs the simplest algorithm as $(\sqrt{x})^2$. In general, a binary system usually has a smaller chance to be still bounded, adding the constraint of non-negative τ will significantly reduce the remain number of survivors' GW permissible time τ . Thus, we would expect the majority of the giant matrix being "nan". We can further reduce the size of the giant matrix by using methods as explained in Appendix B.4.

Chapter 3

Results and Analysis

In this chapter, main results and corresponding analysis will be presented. As described in the dissertation title, contents of this research project can be divided into two parts. The first half are investigations of the physical model of asymmetric SNe acting on populations of the BPASS model, and the second half will be analysis on matching results of our prototypical methodologies and programs of GW archaeology.

In consideration of placing the appropriate amount of contents and materials in the main text, only the most significant and representative results are presented in this chapter, while we put our full outcomes for both parts in Appendixes. The full outcomes of Section 3.1.2 and 3.1.3 are attached in Appendix C and full matching results of Section 3.2.2 form the Appendix D. We will also often refer to the plots and tables in these appendixes, there are also explanations and captions included in details in these appendixes.

3.1 Asymmetric Supernova Explosions on Binary Populations

We present many plotting distributions in this section, from general properties like overall probabilities to specific properties like reduced final velocities (RFVs). The aim of these investigations is to see what statistically patterns could emerge from combining the simplified model (Section 2.2) and the BPASS model (Section 2.3) with methods introduced in Section 2.4.

Another essential analysis shall be comparisons between the Hobbs' kick model and Bray's kick model (Section 2.4.3). When we say a Hobbs' kick model, we actually mean assuming the kick is a constant value $w = 265$ km/s, while the use as a root-mean-square width for the MB distribution is applied only when we discuss kick speed distribution by default. Thus, when we do comparisons between these two kick models, we want a Bray's equivalence of some fixed α and β values. To find these values, we use a simple fit. Since we already got a binary population with their M_1 and M_3 , for any given α and β , we can immediately compute their corresponding Bray's kick. Then, we can calculate their IMF-weighted mean ratio, by dividing each of their Bray's kick value by 265 km/s and computing a IMF-weighted mean for them. An ideal fit should have a such ratio ≈ 1 . However, the suggested values by Bray & Eldridge in 2018 [9], as $\alpha = 100$ km/s and $\beta = -170$ km/s, dose not fit the Hobbs' kick well. Also by suggestion of Eldridge, a more appropriate Bray's model for this research could set $\beta = 0$. After removing β , we find the $\alpha = 100$ km/s Bray's kick gives a good fit with an IMF-weighted ratio ≈ 1.01 for the statistically effective (9089 systems of $\text{IMF} \geq 0.1$) samples. Henceforth, when we say a Bray's kick model without specifying, we mean a kick $w = 100(m_1 - 1)$ km/s.

3.1.1 Probability Distributions

In the context of this research project, there could be two sorts of probabilities. The first kind is a direct statistical result of a large population under a certain set of kick parameters \mathbf{w} , by counting how many systems are disrupted or survival, then renormalise it with IMF weight, like \mathcal{R}_H and \mathcal{R}_B as introduced in Section 3.1.3 and Appendix C. The other sort of probability is much more general, by assuming the kick distributions in Section 2.4.2, and using integrals as formulated in Section 2.4.4. Examples can be found in the P_{run} columns of tables of Appendix A.

However, if we use a fully numerical integration of the formula in Eq 2.29, for example using `integrate dblquad` from `scipy` in `Python`, it will take too much CPU time to work out results for a large population. Thus, in considering our available computational resources and capability, when dealing with large populations, we will instead use a partially numerical integration, that is, using a numerical integration with greater step sizes. In practice, we integrate θ from 0 to π , and integrate kick speed w from 0 to 2000 km/s. The partial step sizes are 1° for θ , and 5 km/s for w , equivalently, 180 steps for θ and 400 steps for w .

Finally, we fully integrate the first 250 theoretical binary systems and partially integrate the first 9089 theoretical binary systems (also known as the statistically effective samples, see Appendix A), then record and print these values. Recall that these binary populations are provided by the BPASS model, and they are ranked in the manner of their IMF weight which is stellar birth probability. We then perform an error analysis between the 250 full integration and their partially integrated equivalences. We find, for the 250 samples, between full and partial integration, the direct absolute mean error is 0.0097%, the direct root-mean-square error is 0.014% and the IMF-weighted root-mean-square error is 0.015%. With errors as small as this level, we could confirm that the partial integration is an acceptable approximation for the runaway probability.

We also find, for the 224 statistically principal (IMF values ≥ 1) samples, their overall (IMF-weighted) runaway probability is 80.681%. That is, after adding a random kick which obeys distributions to this population, about four-fifth systems will be disrupted, and the other one-fifth will remain bounded. For the 9089 statistically effective (IMF values ≥ 0.1) samples, which computed by partial integration, their overall runaway probability is 88.156%. At this stage, we could conclude, for a binary population which is consistent with BPASS predictions, after an asymmetric supernova explosion that obeys isotropic orientation distribution and Maxwell distribution of speed with a Hobbs' root-mean-square width $\sigma_w = 265$ km/s, about 88% of the binaries will be disrupted, and the rest 12% will survive the explosion and be still bounded.

Before we move on more probability distributions based on populations, we would like to present a result that is independent of population. The most common binary compact objects are neutron stars to neutron stars (NS-NS). Hence, we want to inspect, fix the resulting two Supernova remnants (SNRs) being two identical neutron stars, how varying the other two binary system parameters M_1 and r would lead to different runaway probabilities. In practice, we set $M_2 = M_3 = 1.4M_\odot$, and for varying combinations of $M_1 \in [1.5, 10]M_\odot$ and $r \in [10^{0.4}, 10^{2.2}]R_\odot$, we perform a full integration over kick distributions to find the runaway probability at this **B**. We plot the result in a 3D environment, as in Figure 3.1. As we can see from the 3D plot, as increasing of the separation r , the effects of pre-SN primary star mass M_1 is abating. While for lower separations, the mass M_1 is still the dominant factor. One direct and general result is, the runaway probability is increasing as the growing of M_1 and/or of r . Another interesting but weird result is, at large $M_1 \sim 10M_\odot$, there is a tiny valley locating around $r \sim 6R_\odot$, which not suggest the conclusion that increasing of r can always rise the runaway probability. One possible physical interpretation is that at large mass of M_1 , if the binary stars get too closed (e.g. $r \sim 3R_\odot$), it might be easier for them to be disrupted or merged, and it is time to include consideration of the shell impact.

Runaway Probability for NS-NS Configuration

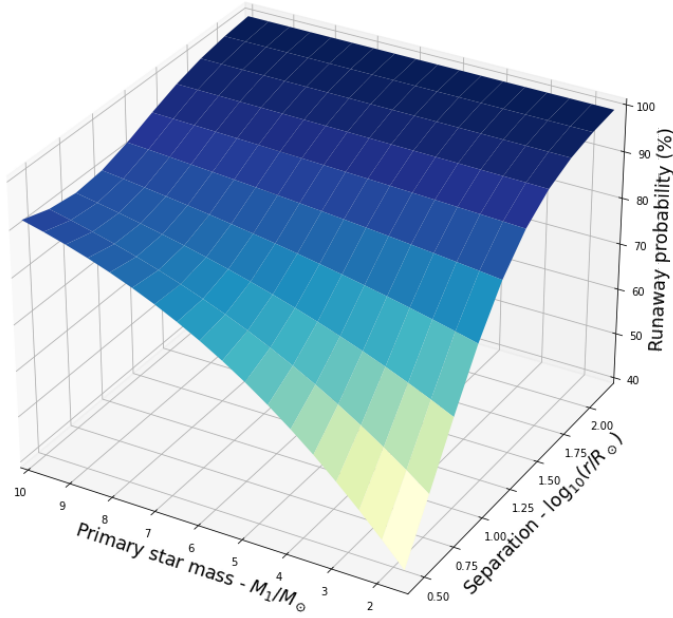


Figure 3.1: The 3D plot of runaway probability for NS-NS binaries with different initial mass M_1 and pre-SN separation r . Note that the r -axis is in logarithm scales. A general trend of increasing M_1 and/or r can increase P_{run} is observed.

Now we can come back and go on to see the probability distribution of the 9089 statistically effective samples, with respect to pre-SN period P in days. The plot is shown in Figure 3.2:

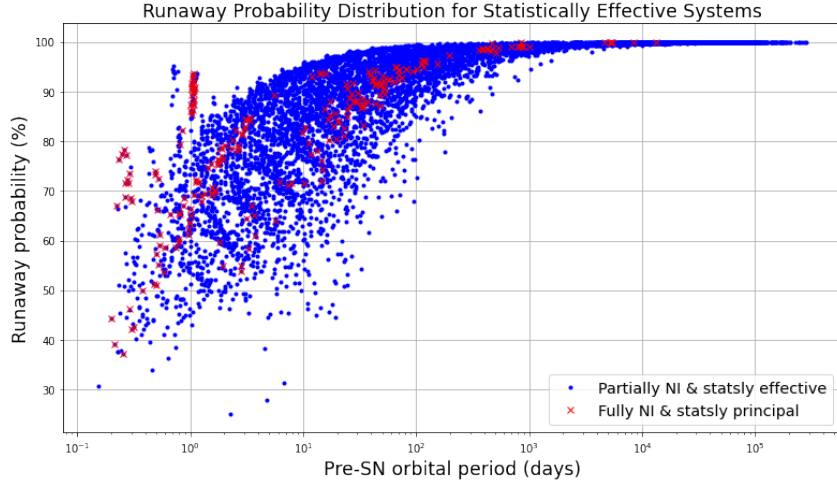


Figure 3.2: NI is an abbreviation for “numerical integration”. As shown in the legend, blue dots are statistically effective samples calculated by partially NI, and red crosses are statistically principal samples computed by fully NI. With respect to period, the runaway probabilities show a reflected negative exponential pattern.

Another good comparable distribution shall be the threshold (maximum bounded) kick w_{\max} , as formulated in the Eq 2.23. By computing the w_{\max} for the the same statistically effective sample that are plotted in Figure 3.2, we can give a comparison plot Figure 3.3:

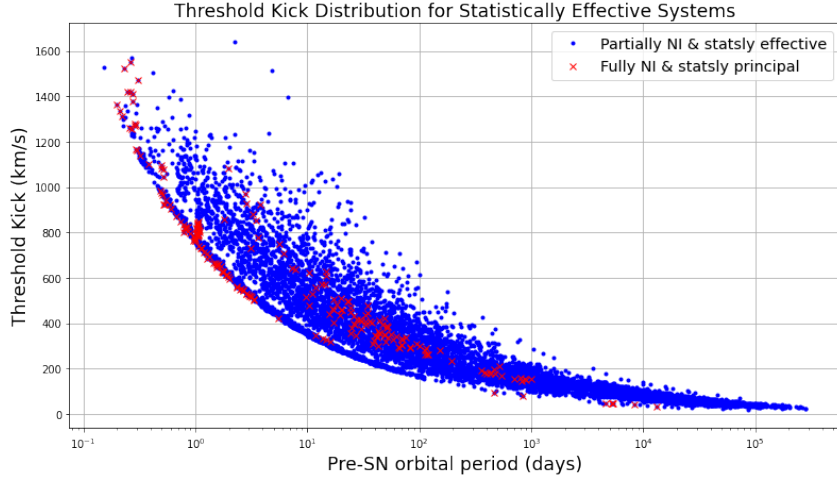


Figure 3.3: Correction: since the threshold kick w_{\max} can be computed analytically, there is no such integration types, so the legend is simply the same as in previous figure, blue dots for 9089 samples and red crosses for 224 samples.

As we can see, w_{\max} shows a similar but reflected pattern as the runaway probability. This phenomenon is easy to understand: with a higher threshold kick, it is harder for a random kick to disrupt the system, while with a very low threshold kick, any random kick could break the gravitational bounds. Since w_{\max} is calculated analytically, and directly depends on \mathbf{B} , its shape and pattern is more clear and compact. While the runaway probability is a result of complicated numerical processes, so its distribution is not regular as w_{\max} . Many systems with $P \sim 1$ day have higher runaway probabilities than its general trend, but they converge to 100% quicker for high periods than w_{\max} .

Finally, we want to see how the specific runaway probability is affected by θ . Recall from the simplified model, the principal (bounded-unbounded) indicator ξ is independent of ϕ , so do the runaway probability. We plot for the Hobbs' kick, and as comparisons, we also plot several Bray's kick with different parameters α , and assuming $\beta = 0$ for all Bray's kick.

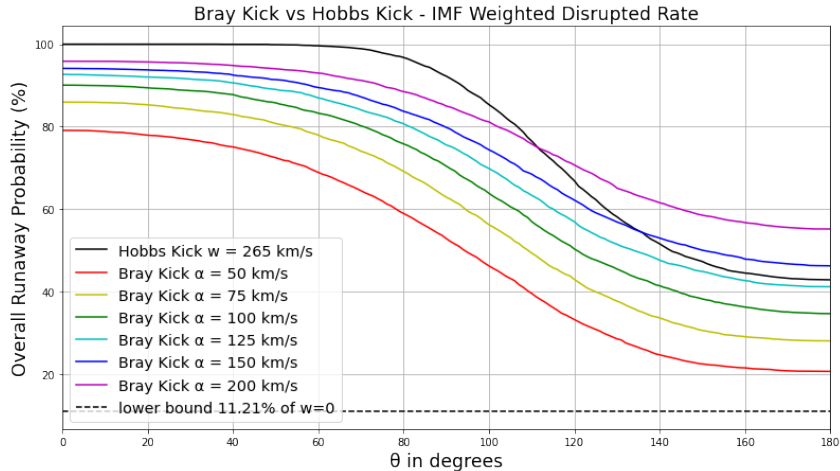


Figure 3.4: The green line is the typical Bray's kick we use for comparing with the Hobbs' kick, which is the black line. In summary, higher kick magnitude implies higher probability.

As we can see, there is a dashed line bounds below of the plot, this is the disrupted rate when the SN explosion is symmetric, i.e. $w = 0$, and it is the natural minimum probability for such a

population to be disrupted, since losing mass is enough for some system to be unable to sustain gravitational connection.

3.1.2 Eccentricity Distributions

We have investigated the most general characteristic, runaway probability P_{run} , which could be even independent of specific kick parameters, in last section. Now we are going to consider a less general property, the eccentricity e . Its generality follows from the fact it is an astrophysical property that exists for both bounded and unbounded cases, and its value can indicate how much influential of the kick to the shape of the post-SN orbit, since we have assumed a circular orbit ($e_0 = 0$).

There are ten groups of plots of eccentricity distributions, each contains four panels of plots. Each group of plots corresponds to a $\theta \in [30^\circ, 165^\circ]$, with a step size of $\Delta\theta = 15^\circ$. The reason why we did not go over the whole domain $[0^\circ, 180^\circ]$ is because one main goal of eccentricity analysis is to conclude the effects of ϕ -family (i.e. ϕ^*), and for θ closed to 0° or 180° , $\sin\theta \rightarrow 0$ and thus contributions of ϕ^* in e are vanished. Hence we only plot the distributions with observable ϕ^* distinctions. The four panels correspond the Hobbs's kick or Bray's kick with respect to primary star mass M_1 or pre-SN separation r . To avoid to put too many figures and too lengthy contents in the main text, full results and plots of this section are presented in Appendix C, Figure C.1 to C.10.

Four panels from different θ are selected and presented as representatives for results of this section, in Figure 3.5.

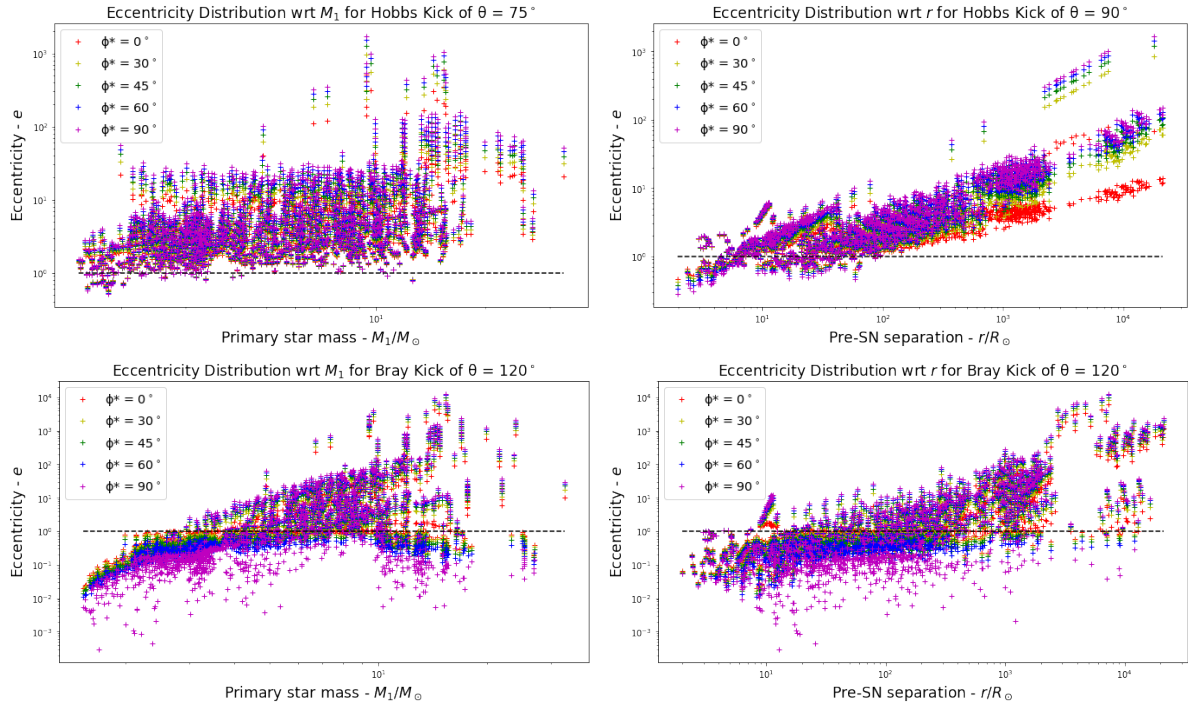


Figure 3.5: Selected plots for eccentricity distributions, please see all figures in Appendix C.

A common pattern for all types of plots is that, for the same system of same θ , with higher $\phi^* \in [0^\circ, 90^\circ]$, equivalently with lower $c_2 = \cos^2\phi$, its eccentricity will be further from the boundary line. This is a directly mathematical result. Another common pattern happens for large $\theta \geq 105^\circ$, this is when the kick has components in the negative direction to the pre-SN orbital velocity \mathbf{v} . For $105^\circ \leq \theta < 180^\circ$, and for survival systems with large $\phi^* \sim 90^\circ$ only, they

could have extremely low eccentricities $e \sim 0.001$. One possible interpretation is, for large θ and $\phi \approx 90^\circ$ or $\phi \approx 270^\circ$, it is possible for certain kicks to relaunch the SNR into a perpendicular, new and nearly circular orbit. For $\phi^* \approx 90^\circ$, $w_y \sim 0$, so only x and z kick components are considerable. For a lucky kick, w_x component cancels v , and $w_z \sim \sqrt{G(M_2 + M_3)/r}$, the orbital velocity required to circularise the new orbit again. In this case, we see that the new orbit is in the y - z plane with respect to the pre-SN coordinate system as illustrated in Figure 2.1.

In particular, for each types of plots, we found the following trends and analysis:

- Hobbs' kick wrt M_1 : There is no strong patterns for this kind. As presented and stated in previous section in Figure 3.4, more binary system will survive the SN explosion as increasing of θ . Hence, in the context of eccentricities, more data points will go across the boundary (black dashed) line from above to below. One remarkable result is there are disrupted systems with very large eccentricities $e \sim 1000$ of $M_1 \sim 10M_\odot$. This only happens for extremely large ξ , which corresponds to sufficiently small v and \tilde{m} , so for these systems a great amount of ejecta is expected.
- Hobbs' kick wrt r : A strong linearity appears, but this linearity start being broken down from $\theta = 105^\circ$. At least for $\theta \leq 90^\circ$, we could confirm a linear relationship between the final eccentricity and pre-SN separation. Without changing masses, greater separations mean slower orbital velocity, which is easier for any kick velocity to take stronger effects. This physical fact is no longer true for higher θ , since the kick start slowing and even reversing the motion of the SNR.
- Bray's kick wrt M_1 : A weak logarithm trend appears for lighter M_1 , and similar to the linearity of Hobbs vs r , it eventually disrupted for higher θ . There also several systems with larger M_1 , that has extremely high eccentricities. Unlike Hobbs, Bray's eccentricity peak locates about $M_1 \sim 15M_\odot$. This mass is closed to the upper bound of the pre-SN mass of a star that going to collapse to a neutron star, so it could have a small \tilde{m} , and Bray's model provides a even intense kick.
- Bray's kick wrt r : It has a similar linearity to of Hobbs' kick, but much weaker. This might be a result of implicit relationship between the Bray's kick value and the separation, since Bray's kick entirely depends on the Supernova process of the star, and longer separation only contributes to reduce the pre-SN orbital velocity.

In summary, variations usually become notable at some where between $\theta = 90^\circ$ and $\theta = 105^\circ$, which corresponds to the beginning of negative direction of the kick adding the velocity. For comparison between Hobbs' kick and Bray's model, a weak conclusion could be constant kick depends more on separations, while a SN-dependent kick is definitely affected by the stellar mass.

3.1.3 Velocity Distributions

One last important distributions we want to compare will be reduced final velocity (RFV). Keep in mind, when we are discussing velocities for a binary after a SN explosion, we mean the reduced one that divided by its pre-SN orbital velocity v . The reason to do this is straight-forward - a binary's final velocity has direct dependence on v , with a higher v will definitely lead to higher final velocity, thus comparisons between final velocities in km/s for a binary population will be less evident.

By the same reasons for eccentricity figures, the full results and plots of this section are attached in same Appendix C, Figure C.11 to C.23. However for RFV, its range runs over the whole domain $\theta \in [0^\circ, 180^\circ]$ with the same step size $\Delta\theta = 15^\circ$, so it has thirteen figure groups, each

contains four panels of plots. The relevant models and variables (i.e. x -axis) are at the same location in each figure as for eccentricities.

One more notable assumption for this section's plots is for clarity, we have set $\phi^* = 0$ and then ignored the effects of ϕ^* for these plots. This simplification is made to avoid too much figures (if we consider all ϕ^* as in Section 3.1.2, it will need $15 \times 13 \times 4 = 780$ more plots, which requires 98 more pages!), for which most of them have very closed distributions, and relevant investigations in previous section suggest that ϕ^* dose not play an essential role in most cases. In addition, we want to focus on the effects to final velocities by θ .

Similar to eccentricities, we select four panels from different θ as representatives for results of this section, and they are presented below in Figure 3.6.

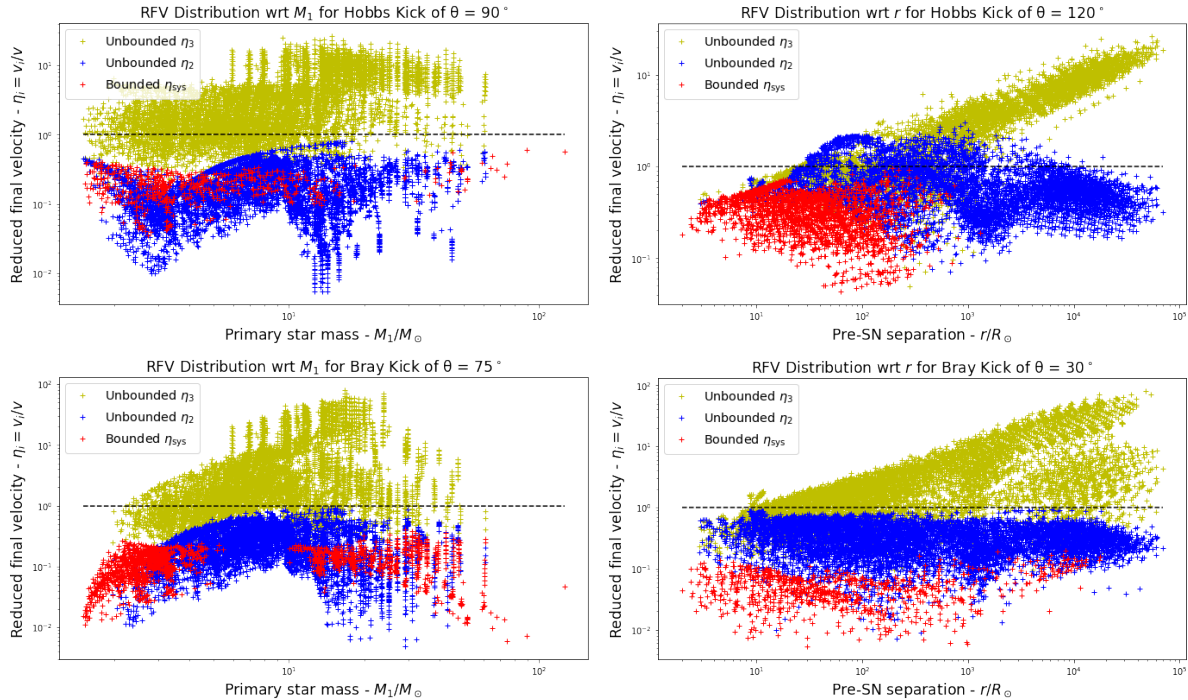


Figure 3.6: Selected plots for reduced final velocity (RFV) distributions, please see all figures in Appendix C.

As predict in Section 3.1.1, higher θ yields more survivors. Even though the numbers of survivors are not identical for Hobbs' kick and Bray's kick, they share similar trends. Except most patterns are dramatically changed after $\theta \sim 105^\circ$, which is consistent with results of eccentricities, there is only one remarkable common phenomenon for RFVs. Recall that the black dashed lines are unit lines, which are $\eta = 1$ and equivalent to pre-SN orbital velocities v of each binary systems. Hence being above or below this line means the relevant velocity is higher or lower than its pre-SN velocity. The common pattern is, before $\theta = 105^\circ$, all companion velocities η_2 (blue + in plots, the norm of Eq 2.20, the FRV of the companion compact object) are below the unit line, suddenly at and after a threshold angle $\theta = 105^\circ$, many data points of η_2 exceed the unit line and reach a high tide. After then, there are always data points regularly over the unit line and gradually stabilise to a low plain of data points. The same thing happens for systematic FRV η_{sys} (red + in plots, Eq 2.21) of survival cases, but much less intense compare to η_2 and its threshold angle is $\theta = 135^\circ$.

In particular, for each types of plots, we found the following trends and analysis:

- Hobbs' kick wrt M_1 : Similar to eccentricities, no strong patterns are observed. One valley

of η_2 appears around $M_1 = 3M_\odot$ at $\theta = 90^\circ$, and many systems around this valley become survival from being disrupted. Then just like the ebb before flood, data points of η_2 rapidly rise and exceed the unit line at $\theta = 105^\circ$.

- Hobbs' kick wrt r : Again similar to eccentricity distributions, a strong linearity of η_3 (yellow + in plots, the norm of Eq 2.19, the FRV of the compact SNR) is confirmed, which last over the whole range of θ . Unlike the high tide with respect to M_1 , a weak peak pattern emerges after the threshold angle, and subside later. Furthermore, we can confirm that for all cases, only systems with relatively shorter separations are able to survive, or specifically, for $r \lesssim 10^3 R_\odot$. This is again a simple physical result as in Section 3.1.1, with longer separation it has a slower orbital velocity, and so a lower threshold kick, and so being difficult to survive.
- Bray's kick wrt M_1 : A similar but even weaker logarithm trend observed for lower M_1 . If we treat all three kinds of RFVs as a whole, unlike eccentricities that the pattern get disrupted and dissolve as growing of θ , the logarithm patterns of the “RFV union” get stronger as θ increasing. One significant difference between Bray's kick and Hobbs' constant kick, is that Bray's model predicts survivors of very low or high M_1 , at smaller θ angles. The lower-massive survivors are neutrons stars, since their former stars are not very massive, their M_1/M_3 ratios is relatively small, thus lower kick speed for Bray's model; similar for those more massive survivors, they are black holes, their M_1/M_3 ratios are also small enough for they to be bounded.
- Bray's kick wrt r : Once again, similar but weaker linearity to both of eccentricity equivalence and Hobbs' model. Hence the reason to explain this shall be the same as stated in previous section. Notice that even survivability has dependence on r for Bray's kick, but much weaker. We see there could be eventually bounded systems from all r ranges, although more survivors are predicted for shorter separations. This should be closer to observations.

In summary, along with similar conclusions follow from eccentricity section, the velocity distributions predicted by Hobbs' constant kick is dominated by pre-SN separations r rather than star mass M_1 , while the same RFV distributions suggested by Bray's model are reversal, it shows a stronger dependence on M_1 and relatively fair scatters on r , which have better consistency with observations. Therefore, at this stage, we can barely confirm that dependence on M_1 and r are better predicted by Bray's model than constant kick models.

3.2 Gravitational Wave Archaeology

As one of practical applications of the asymmetric supernova explosion model, final configurations of survival systems can be applied to predict gravitational wave events, under effects of gravitational radiations. In the second half chapter of results, we are going to present our investigations on how different kicks can lead to different ages required for the two compact objects to merge, as well as general results of our numerically matching prototypical program.

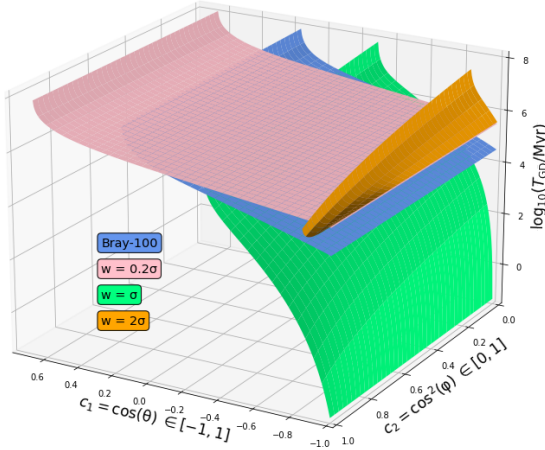
3.2.1 Gravitational Decay Time

Before conducting analysis on specific gravitational wave observations, a brief exploration on the direct impacts of kick parameters on gravitational decay time T_{GD} is necessary to reveal the physical dependence of kicks and time constraints. Four 3D plots of T_{GD} level surfaces with respect reduced orientation parameters $(c_1, c_2) = (\cos \theta, \cos^2 \phi)$ are listed in Figure 3.7. Four plots correspond to four typical compact binaries, NS-NS, NS-BH, BH-NS, BH-BH.

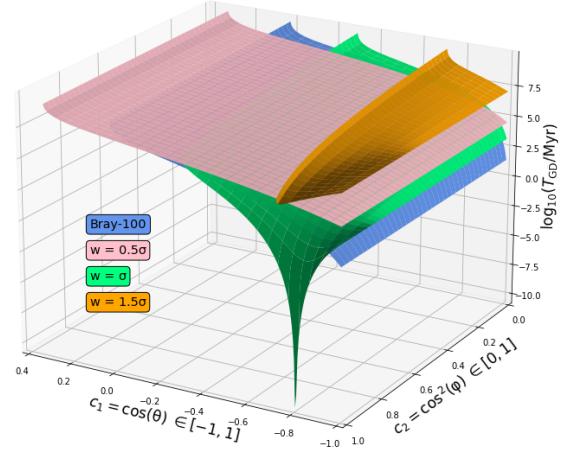
Table 3.1: Parameters table of Figure 3.7

plot location	SNR_3	S_2	$M_1 (M_\odot)$	$M_2 (M_\odot)$	$M_3 (M_\odot)$	$r (R_\odot)$
Upper left	NS	NS	3	1.4	1.4	10
Upper right	NS	BH	4	20	1.4	100
Lower left	BH	NS	60	1.4	50	100
Lower right	BH	BH	60	50	50	1000

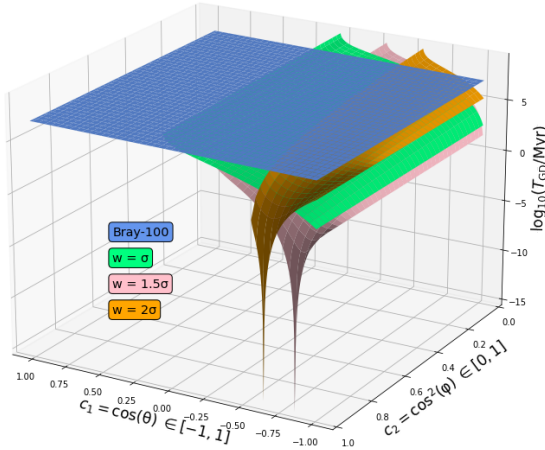
Gravitational Decay Time Level Surfaces for NS-NS System



Gravitational Decay Time Level Surfaces for NS-BH System



Gravitational Decay Time Level Surfaces for BH-NS System



Gravitational Decay Time Level Surfaces for BH-BH System

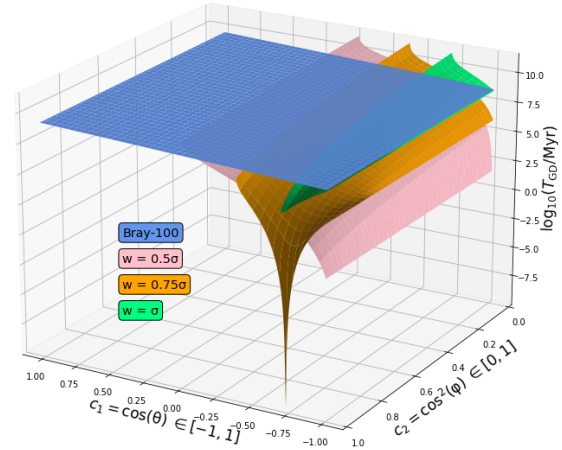


Figure 3.7: Each of the four 3D plots contains four level surfaces, each surface corresponds to different kick assumptions. For all cases, the blue surface is the typical Bray's model with $\alpha = 100$ km/s and $\beta = 0$. All other three are constant kicks with speed of multiples of $\sigma = 265$ km/s, and the specific values are chosen for appropriate displaying clarity.

Note that by convention, the first compact object is the supernova remnant (SNR) of the primary star S_1 , which is M_3 , and the second compact object is the companion star S_2 . Hence we present both NS-BH and BH-NS, since the different permutations represent different astrophysical configurations, and sequence is important here. We also list the binary system parameters

set for these four plots in Table 3.1.

For all plots, if a level surface ends at some boundary for some θ , it simply means at this θ with its kick magnitude w , the binary system is no longer bounded hence there is no such time to merge. One clear pattern is that c_2 only take considerable effects when closed to its maximum value 1 with small values of c_1 , which are corresponding to $\phi = 0^\circ$ and $\phi = 180^\circ$, and $\theta \sim 135^\circ$ by inspection. One more common pattern is applicable for small c_2 , corresponds to higher ϕ^* , that T_{GD} increases smoothly as the increasing of c_1 , or decreasing of θ . Together, when $\phi^* \approx 0^\circ$ and $\theta \sim 135^\circ$, T_{GD} can reach extremely low values about a few minutes or even a few seconds. Hence for certain kicks and orientations, the binary system will merge immediately after the SN explosion, and we would say the physics at these extreme cases should be consider more carefully.

The lower two plots, which corresponds to the SNRs being black holes, both are $60M_\odot \rightarrow 50M_\odot$. In this setting, their Bray's kick will be very low, with only $100(60/50 - 1) = 20$ km/s. And at this low speed of kick, their T_{GD} reach a high and stable plain. Hence we can predict, with extremely low kick speed or even no kick, if the system survives the SN, their T_{GD} can reach the maximum value for which they can. But when the kick speed is higher, the pattern is not clear. We see, except for BH-BH configuration, the level surfaces of the intermediate values of kick speed have been placed with the lower T_{GD} . This observation means, the T_{GD} dose not strict depend on w linearly, but instead reach minimum levels for appropriate values of w for example the Hobbs' root-mean-square width $\sigma = 265$ km/s for some systems.

In summary, the results of this section suggest that in most cases, the gravitational decay time T_{GD} will increase if θ increases, and ϕ only take significant effects when it is closed to 0° or 180° . And if we also have $\theta \sim 135^\circ$, it is possible for the survival systems to merge under gravitational radiation immediately after SN. Furthermore, with minimum kick speed w , T_{GD} will form a stable plain of maximum values, but it requires appropriate ranges of kick speeds to reach a minimum level. Hence, unless $\theta \sim 135^\circ$ and $\cos^2 \phi \approx 1$, one can safely omit considering contributions of ϕ if suitable. And in most cases, focusing a kick speed $\sigma \leq w \leq 2\sigma$ is enough for us to find a relatively low values of T_{GD} .

3.2.2 Events Matching Results

The models and results correspond to this section can be recognised as the most important achievements in this research project. We have investigate and match the whole gravitational wave detection list from the Gravitational Wave Transient Catalog (GWTC) [16]. In specific, totally 90 GW events are considered in this project, and they have three different versions of event confirmations. There are seven version 3 events, five version 2 events and the rest of events are version 1. We finally matched 87 events with theoretical systems in the BPASS population with full time constraints. One of each version 1, 2 and 3 transients were unsuccessful, GW191219_163120 (version 1) is currently fail to match since it has $M_b = 1.17^{+0.07}_{-0.06} M_\odot$, which has an upper bound lower than the minimum BPASS mass $\sim 1.259 M_\odot$. However, if we use a weaker time constraint by removing the upper limit of the look-back time $t_{\text{LB}}(d_L)$, GW170817 (version 3) and GW190814 (version 2) can be successfully matched in BPASS populations, where they cannot be matched with full time constraint.

For clarity, we present matching results of all version 2 and version 3 events in the form of Table 3.2, and results of all version 1 events are listed in landscape tables with a few eliminated columns. For appropriate length of text, all matching results of this section are presented in Appendix D. All matching parameters are generated by our prototypical program of Python code, in a published Kaggle notebook linked in Appendix B.1. Some details of the table contents are explained in Appendix D, but in addition and for emphasis, RNW is the abbreviation for re-normalised weight, this is the matching confidence, which is the probability that this system

or kick is the one that brought out the detected event. In addition, for sustainable tabular width, we delete several less-relevant columns in the landscape tables of version 1 events, and we replace the kick parameters w and θ by their weighted mean values.

Table 3.2: GW Archaeology Match Result Example (GW150914)

Event name	Version	$M_a (M_\odot)$	$M_b (M_\odot)$	$d_L (\text{Mpc})$	$t_{\text{LB}} (\text{Myr})$
GW150914	3	$35.6^{+4.7}_{-3.1}$	$30.6^{+3.0}_{-4.4}$	440^{+150}_{-170}	1256^{+363}_{-447}
Binary RNW (%)	$M_1 (M_\odot)$	$M_2 (M_\odot)$	$M_3 (M_\odot)$	$r (R_\odot)$	$t_{\text{evo}} (\text{Myr})$
78.28	41.34	27.25	35.76	172.52	2.87
IMF weight	$M_{1,i} (M_\odot)$	$M_{2,i} (M_\odot)$	$P_i (\text{day})$	$P (\text{day})$	Z
0.090	150.0	10.0	63.21	31.74	0.008
Kick RNW (%)	$w (\text{km/s})$	θ	ϕ^*	e	$\tau (\text{Myr})$
100.0	397.5	180°	-	0.785	898.50

One summarised result is given by the average values of the weighted mean values of w and θ for version 1 events. We get $w_{\text{avg}} = 343.4 \pm 88.7 \text{ km/s} \approx 1.3\sigma_w$ and $\theta_{\text{avg}} = 143.5^\circ \pm 16.8^\circ$ with $\cos \theta_{\text{avg}} \approx -0.8$.

Another applicable and essential investigation we would like to take is which of S_2 and SNR_3 consists the more massive compact object detected in GW transients, and how much of the mass remain or transfer from M_1 to M_3 for these successful matches. Once again, in consideration of the length of this dissertation, we focus only on version 2 and version 3 events that are successful matched in BPASS populations under fully strict time constraints. One magnified example plot of GW150914 mass transfer is displayed below in Figure 3.8, and plots of the other nine events are arranged in Figure 3.9.

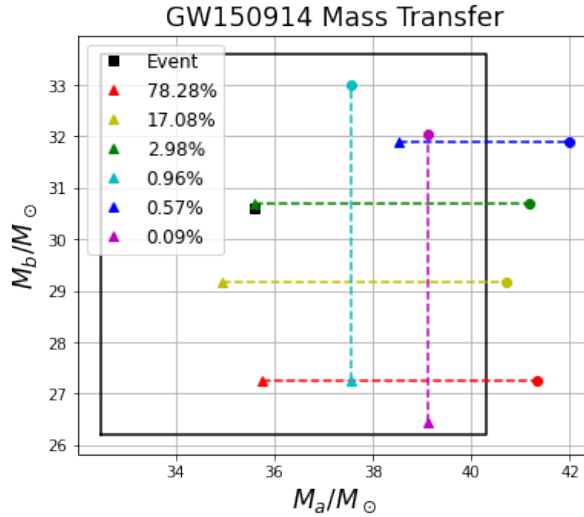


Figure 3.8: An example plot of gravitational wave mass transfer. For clarity, the black square dot is the observed masses of the GW transient event, and the outer rectangle that consists of solid black lines is the mass constraint given by the detection error bar. Circular dots are the pre-SN masses and triangle dots are the post-SN masses, which are the matching masses. Specifically for GW150914, The first three matches with higher RNW values have horizontal traces, implies the fact that the more massive black hole of GW150914 is very likely the compact remnant of the second SN.

In each GW mass transfer plot, the x -axis is corresponding to the more massive compact object A, and the y -axis is corresponding to the less massive compact object B. Hence, a vertical trace (i.e. dashed line) means the companion star S_2 is the more massive compact objects, while a horizontal trace means the supernova remnant SNR_3 is the more massive compact objects. In the legend, each matches is assembled with a Binary renormalised weights (RNW), in percentage. Only the first six matching binaries are shown according to their binary RNW values for each GW events, colors are also assembled for each matches to distinguish them. However, note that the sequences of the events as listed in legends are not ranked according to their binary RNW values, but according to IMF weights of this theoretical systems.

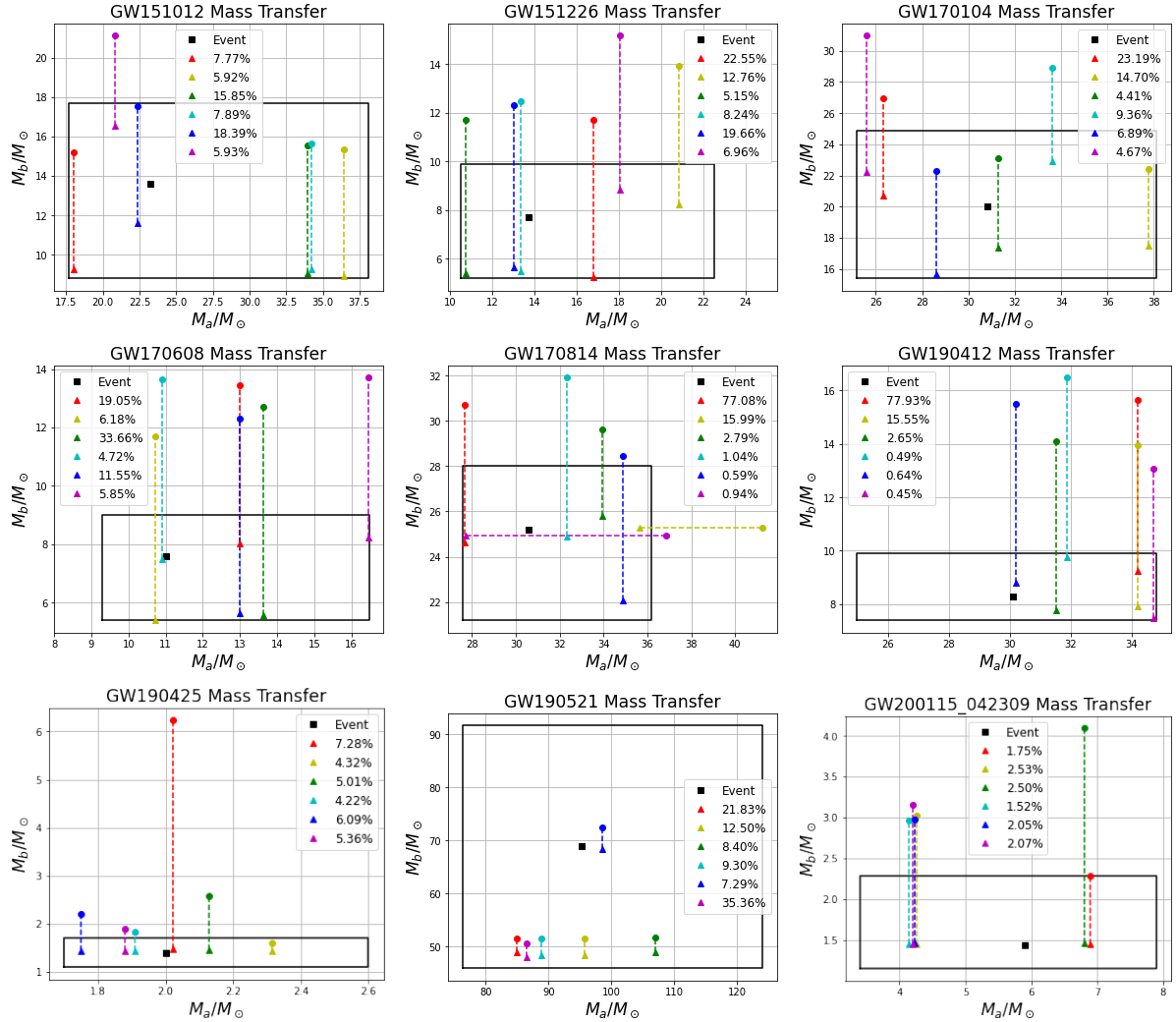


Figure 3.9: Gravitational wave mass transfer plots of the other nine version 2 and 3 events. The plotting types are identical to Figure 3.8. Unlike GW150914, these vertical lines in all the nine plots suggest a conclusion that the preexist compact object S_2 usually have a larger mass than the new SN compact remnant.

In Figure 3.9 of all other events, the absolute dominance of vertical traces implies that the companion compact objects are usually more massive in GW transients. Although only for GW170814, there are two horizontal traces, but their sum confidences only take 17.2% in the first six matches of highest weights, so this distinction dose not break the dominant position of vertical traces down in GW170814. Moreover, the dominant match (red) of GW170814 has a coincident final mass pair as another one (magenta), but they come from different types of mass transfer, one has more massive companion and one has more massive SNR. The matching kick

of the dominant binary match (red) can be found in Table D.4, there is only one kick with lower kick speed at $\theta \sim 180^\circ$. Furthermore, other few matches also have remarkable properties:

- GW190425: The dominant match (red) dose not have significantly higher weight than others, but it has significantly higher pre-SN star mass than others. According to Table D.10, its matching kick is $w = 265$ km/s, $\theta = 138.6^\circ$ and $\phi = 30^\circ$. A Bray's kick with $\alpha = 100$ km/s and 60 km/s can fit well to this kick.
- GW190521: This event consists of two massive black holes, with the secondly highest masses in all GW transients. One apparent feature of its mass transfer is smaller ratio of ejecta, as its traces are relatively short compare to the whole error bar. There are two reasons for this to happen, one is astrophysics, more massive stars have more capability to maintain its remnants, another one is measurement, more massive objects have larger uncertainties. The best match of this event also has much more suitable matching kicks compare to other events, as listed in Table D.7. However, in considering its typical ratio of ejecta, if we reproduce the result by assuming a Bray's kick, we would expect kicks with lower speed will have more weights.
- GW200115_042309: This a typical NS-BH binary transient. The first significant observation is the RNW of its first six matching binaries, these RNW have similar values, and their sum only takes 12.42% of the total. This result implies that GW200115_042309 has a great amount of candidates that can survive a asymmetric supernova explosion and merge in a specific time interval. The second inspection is that many of these matching binaries have similar masses, both initial and final. Hence, in further studies, a clever solution can be adding the weights of similar candidates and find the best fit kind with weighted mean kick parameters.

Surely there could be more interesting and extraordinary results and patterns can be generate from the rest of version 1 events, but due to the limit of space and time of this research project, further suggestions and expectations of this study will be explained in the Discussion Chapter 4.

In summary, we test our simplified model and theory and get instructive matching and fitting results by a constructive methodology, the gravitational wave archaeology. Some of gravitational wave transients can be generated by a certain system with a single kick, corresponding to strict kick conditions. We also found, by direct averaging of the version 1 matching results, the most preferable values of the kick speed is about 1.3 times of the Hobbs' root-mean-square width $\sigma_w = 265$ km/s, and the orientation concentrates about $\cos\theta \approx -0.8$. Illustration of the mass transfers of version 2 and 3 matching results suggests that the companion stars usually have higher masses, and the new born supernova remnants are usually lighter. One exception is GW150914. For detected transients with a sufficiently amount of suitable binary or kick candidates, we might want to combine similar candidates up to different kinds, and search for the most likely kind by accumulating weights of single samples.

Chapter 4

Discussion

The astrophysical model of asymmetric supernova explosions (SNe) is simplified, the methods and programs of the gravitational waves (GW) archaeology are also incipient. Hence, we are going to discuss feasible developments and improvements to our models and methods in order to reach a widely usable tool with higher efficiency and accuracy.

4.1 Further Steps of Models

One complicated astrophysical process that we choose to ignore in our simplified model is the shell impact. As we stated in Section 2.2.1, in most cases, the shell impact can be safely omitted for simplicity. But in order to match observations more precisely, it is necessary to consider some extreme cases. Relative parameters for the shell impact can be generated or fitted in the BPASS model. It is reasonable to expect that adding considerations of shell impact will create less SN survivors, and may also increase the gravitational decay time T_{GD} for some bounded systems that have shorter pre-SN separations.

In the binary population that provided by the BPASS model, every companion compact object S_2 is actually generated by an earlier SN by assuming a plain Hobbs' kick. This simplification of focusing on single SN explosion is helpful for analysing final outcomes of random kicks acting on a binary population. But when we are trying to match and fit observed gravitational wave transients, which consist of two compact SNRs, it becomes necessary to consider a double SN explosions configuration. That is, the binary system undergoes two SN events respectively, and it has to survive both explosions to finally merge and send gravitational wave signals. To do this, one have to work out the exact method that can transfer the post-1st-SN configurations onto the binary evolution models that can describe the secondary star with the 1st-SNR evolution. Theoretically, there is another possibility, the preexist companion compact object can also be a primordial black hole (PBH). But the binary evolution that contains a PBH can be more complicated and new models might be required to be introduced.

Confirming by eccentricity distributions in Section 3.1.2, a binary system is eccentric after an asymmetric SN explosion. Along with the double SN configuration, the assumption of pre-SN orbit being circular may also need to be removed. We would not advise to set a non-circular orbit previous to the fist SN explosion as the immediately next step, since it will arise a new initial parameter thus rise complexity, and circularised orbits are also acceptable approximations to initially formed binary stars. However, it is still inevitable to consider carefully how to prepare the second SN explosion in a survival eccentric orbit. For SN survivors of the first explosion, the evolutionary time interval between the two SN events is also crucial, as this age must also be considered in calculating the GW permissible time τ . The accretion and subsequent mass transfer

between the first SNR and the remaining star should also be considered in the intermediate binary evolution, but fortunately, this process has already been included in the BPASS model. This development would be a significant improvement to investigations of dependence between explosion sequence and GW massive distinction.

4.2 Further Steps of Methods

In consideration of limit time and computational resources available to this research project, when we create the giant look-up table of τ , we used relatively large step sizes in each kick parameters for GW archaeology. Just like any numerical methods, the fitting accuracy can be increased by using smaller step sizes, and this is a typical further progress. Kick speeds w would have stronger demand of reducing step sizes, especially for kick magnitudes $0.5\sigma_w \leq w \leq 2\sigma_w$. A suggested step size shall be $0.1\sigma_w = 26.5$ km/s, or alternatively, we can use even smaller step sizes for $0.5\sigma_w \leq w \leq 2\sigma_w$ and for outside values use successively larger step sizes. In any case, smaller step sizes can give us more accurate fit and even be able to match systems that can only meet the time constraints for very strict kick parameters, which can then significantly increase confidence level of matching results.

One essential objective of this research project is to balance efficiency and accuracy. Even we really want very clear and confidential results, it is generally not applicable and acceptable to wait for each matching result for several hours or even several days. We barely solved the efficiency problem by pre-computing τ then recording relevant outcomes, so that we only have to wait for once. Even though it may still cost some time to import and read the printed data, the process of reading data is still much more quicker than computing those complicated data. But increasing step sizes can also decrease efficiencies. For instance, if we change the step size of the kick speed w from $0.5\sigma_w$ to $0.1\sigma_w$, then the efficiency will also be reduced by one fifth, since there are five times more amounts of data to process. One feasible way is to firstly match GW transients using relatively large step sizes, to find the best fit. If the best fit has a renormalised weight (RNW) greater than 50%, then we can focus on this particular system and calculate its τ precisely using very smaller step sizes for all kick parameters, similar to what we have done in Section 3.2.1. The practicability of this method is based on that, in general, we would not expect a system with very low RNW values in large-step-sizes matching to become dominant in small-step-sizes matching. Another way is to code in relatively more efficient programming languages, for example **FORTRAN**. **Python** is easier to learn and use, but it is not the most suitable tool for data computation and analysis. Based on different operational logic, when computing data of such large sizes, **FORTRAN** can be much more faster. Our **Python** codes are published in Kaggle notebook, its link can be found in Appendix B.1.

The point-like typical formation time simplification that we made as explained in Section 2.5.2.3 was not a completely appropriate assumption. Star formation is a complex process and cannot in general be modeled by single time points, we only do this as using the full mass-time distributions will rise complexity too much at the current stage. Therefore for next development, we would suggest to using weighted discrete time points for each metallicity that obey formation history distributions, as what we did to kick speeds. Now one clever modification can be taken is to remove the formation time from τ and calculate it separately for its own giant matrix, then adding them together when matching. If higher complexities are affordable, one can even look for other formation time-metallicity dependence in different galaxies or clusters.

Another improvement can be constructing distributions in the error bars of detected values of GW transients. For example, in Figure 3.8, the green triangle almost coincides the detection, while the magenta triangle approaches the boundary of allowed masses. An intuitive estimation would not suggest that these two values have the same weight with respect to mass constraints,

being closer to the exact detection should have slightly higher significance. However, in our primary version of GW archaeology, we treat all candidates that lie in the error bars equally, for both mass constraints and time constraints. So we would advise to consider creating an appropriate weight distributions in error bars, the distributional intensity shall not be too strong. One possible shape of distribution could be pyramid, that is, the detection (black square) lies on the tip, and all boundaries have equally but less weight than the tip, and intermediate regions are connected by straight lines.

Specific investigations on more accurate matching results are also necessary to be conducted in further studies. In this research project, we only present the mean values with standard deviations of kick speeds w and angles θ for all version 1 matching results as representatives, however this simplification will seriously omit information. We only decide to summarise our results in this way because time limitation. We advise future researchers to present their results in ways, for example 3D plots of fitting points of kick parameters, and even the level surface that enclosed all feasible values. We expect further studies can confirm distributions of suitable kicks for each GW transients, and such conclusions would provide stricter constraints on kick parameters, hence may further increase efficiency and accuracy of future versions of gravitational waves archaeology

Chapter 5

Conclusions

A crucial achievement and original study of this research project shall be the gravitational waves (GW) archaeology, includes its theory, hypothesis, method and a programming prototype that coded in a Python Notebook that linked in Appendix B.1. This program can efficiently compute possible initial parameters for unspecified gravitational wave transients as well as any astrophysical outcomes by an asymmetric supernova explosions, by pre-calculating the relevant time points or bins of a large sample of binary populations. By a few investigations, we can confirm this model and program works at an acceptable level of accuracy and efficiency.

The simplified model of asymmetric supernova explosions (SNe) has been tested and analysed successfully. As a generalised property, the runaway probability of a population can indicate the expected quantity of supernova survivors. After an asymmetric SN (the ‘kick’) under assumptions of the simplified model, if its orientation can be described by an isotropic distribution as well as its speed obeys a Maxwell-Boltzmann distribution with a Hobbs’ root-mean-square width $\sigma_w = 265$ km/s, then for a population of binary stars that can be modeled by BPASS codes, we would expect $\sim 88\%$ of all binaries will be disrupted, or equivalently, a single random binary system has $\sim 12\%$ of chance to survive such a SN explosion.

The significance and dependence of the kick parameters are also confirmed via several aspects including specific probabilities, final eccentricities, reduced final velocities (RFVs) and gravitational decay time T_{GD} . The kick speed (magnitude) w usually has a strong and clear dependence on most results, with higher speed, a system has higher chance to be unbounded in general. Thus when we are looking for suitable kicks to produce a specific T_{GD} , we need its speed lies in an appropriate range, rather than seeking for exceptionally higher or lower ones. Effects of direction parameters are more complicated. In general, the variation of θ dose not take remarkable effects for $0^\circ \leq \theta \leq 90^\circ$, the changes in patterns are gradual until θ cross over the 90° boundary. The impact magnitudes by θ variations reach maximum around $\theta \approx 105^\circ$, then keep slow decreasing but the general magnitudes are still stronger. This is a result by reversal kick direction compared to pre-SN orbital velocity \mathbf{v} . For survival cases, except around the neighborhood of $\theta \sim 135^\circ$, for where the effects of ϕ reach maximum, higher θ usually implies higher T_{GD} . Thus, expect around $\theta \sim 135^\circ$, contributions of ϕ can be safely omitted if necessary. For ϕ -family $\phi^* \sim 0^\circ$ ($\phi \approx 0^\circ$ or $\phi \approx 180^\circ$, $\cos^2 \phi^* \approx 1$ and $|w_y| \gg |w_z|$), the eccentricity is closer to $e = 1$ and T_{GD} might be able to reach minimum values of a few minutes or even a few seconds; for $\phi^* \sim 90^\circ$ ($\phi \approx 90^\circ$ or $\phi \approx 270^\circ$, $\cos^2 \phi^* \approx 0$ and $|w_z| \gg |w_y|$), the eccentricity is further from $e = 1$ and T_{GD} lies on a stable plain and can reach maximum.

Comparisons between constant Hobbs’ kick and Bray’s SN-dependent kick model are also remarkable. We set a standard group of constant kick speed with values of the Hobbs’ MB root-mean-square width $w = \sigma_w = 265$ km/s, and a comparison group of Bray’s kick $w =$

$100(m_1 - 1)$ km/s, where $m_1 = M_1/M_3$ and this formula has equivalent IMF-weighted mean speed as σ_w , for a binary population generated by BPASS model. Plots of eccentricities and reduced final velocities (RFV) in Appendix C draw a conclusion that the constant speed model has stronger dependence on pre-SN separation r , but the Bray's equivalence depends on primary star mass M_1 more apparently than on separations. Bray's model also predicts more survivors than constant kick models for lower θ of both less massive neutron stars (NS) and more massive black holes (BH), which has better astrophysical reasonableness. Furthermore, the Hobbs' kick also prevents binary systems with longer pre-SN separations to survive the explosion, while Bray's model agrees that more survivors should have shorter separations but also allows a considerable amount of survivors of longer separations at all orientations. Even more investigations are advised to be conducted in order to confirm the results at more extreme cases, at this stage, a conclusion follows from dependence on M_1 and r of the two model suggests that the Bray's SN-dependent kick model has higher consistency to observations.

By combining the physics from the simplified model, ideal kick distributions and populations from the BPASS model, we successfully construct and operate the exploratory methods and programs of gravitational wave archaeology. We successfully matched all 89 matchable gravitational wave transients in GWTC [16] by searching in a giant look-up table of pre-computed GW permissible time τ . Some GW events can only be generated under strict kick conditions, while some can be caused by a wide range of kicks. Matching results of version 1 GW transients indicate the most preferable kick speed is $w = 343.4 \pm 88.7$ km/s $\approx 1.3\sigma_w$ and the kick angle θ concentrates about $143.5^\circ \pm 16.8^\circ$. By focusing on version 2 and 3 matching results and visualising their mass transfers of a few theoretical binaries with the highest weights, we find that some events like GW170817 and GW190814 can be only fitted under weaker time constraints, and the rest of them implies a fact that the more massive compact object in a GW transient is very likely to be the companion which is a compact remnant from an earlier supernova event, and the new born SNR is usually less massive. While exceptions and especial results are also expected. In addition, inspections of successful kick speeds also suggest, that in the case without sufficient resources, focusing on kick speed $\sigma \leq w \leq 2\sigma$ might be a feasible strategy.

As a final summary and future expectation, at the primary stage of gravitational wave archaeology, its methodology successfully generates a considerable amount of remarkable results, and future improvements (as explained in Chapter 4) are also expected to operate and generate more accurate and confident outcomes. Such developments include but not limit to using complicated but more realistic kick models, coding in more suitable and efficient languages like **FORTRAN**, extending searching ranges, optimising distributions etc. We believe the ideas and constructions of gravitational wave archaeology would build new paths for binary star astrophysicists and gravitational wave experimenters to study binary evolution and search potential binary candidates for future observations.

Acknowledgement

Great thanks to Professor Jan Jamie Eldridge, who provides me a priceless opportunity to conduct this research project, and who lead me to explore the world and study of astrophysics and binary star evolution. Thanks also go to Dr David Krovcheck, who provides significant supports to all Honours students in the Department of Physics.

Under the circumstances of COVID-19 pandemic, this research project was entirely conducted in my home and online. Thanks to my parents who both mentally and financially support my undergraduate and honours study.

References

- [1] Dan Maoz. *Astrophysics in a Nutshell: Second Edition*. Princeton University Press, 2016.
- [2] T. M. Tauris and R. J. Takens. Runaway velocities of stellar components originating from disrupted binaries via asymmetric supernova explosions. *Astronomy and Astrophysics*, 330:1047–1059, February 1998.
- [3] T. M. Tauris, R. P. Fender, E. P. J. van den Heuvel, H. M. Johnston, and K. Wu. Circinus X-1: survivor of a highly asymmetric supernova. *Monthly Notices of the Royal Astronomical Society*, 310(4):1165–1169, December 1999.
- [4] J. J. Eldridge, E. R. Stanway, L. Xiao, L. A. S. McClelland, G. Taylor, M. Ng, S. M. L. Greis, and J. C. Bray. Binary Population and Spectral Synthesis Version 2.1: Construction, Observational Verification, and New Results. *Publications of the Astronomical Society of Australia*, 34:e058, November 2017.
- [5] E. R. Stanway and J. J. Eldridge. Re-evaluating old stellar populations. *Monthly Notices of the Royal Astronomical Society*, 479(1):75–93, September 2018.
- [6] Pavel Kroupa, Christopher A. Tout, and Gerard Gilmore. The Distribution of Low-Mass Stars in the Galactic Disc. *Monthly Notices of the Royal Astronomical Society*, 262:545–587, June 1993.
- [7] Maxwell Moe and Rosanne Di Stefano. Mind Your Ps and Qs: The Interrelation between Period (P) and Mass-ratio (Q) Distributions of Binary Stars. *The Astrophysical Journal Supplement Series*, 230(2):15, June 2017.
- [8] G. Hobbs, D. R. Lorimer, A. G. Lyne, and M. Kramer. A statistical study of 233 pulsar proper motions. *Monthly Notices of the Royal Astronomical Society*, 360(3):974–992, July 2005.
- [9] J. C. Bray and J. J. Eldridge. Neutron star kicks - II. Revision and further testing of the conservation of momentum ‘kick’ model. *Monthly Notices of the Royal Astronomical Society*, 480(4):5657–5672, November 2018.
- [10] C. S. Kochanek. Supernovae producing unbound binaries and triples. *Monthly Notices of the Royal Astronomical Society*, 507(4):5832–5846, November 2021.
- [11] David W. Hogg. Distance measures in cosmology. *arXiv e-prints*, pages astro-ph/9905116, May 1999.
- [12] Planck Collaboration, N. Aghanim, Y. Akrami, M. Ashdown, J. Aumont, C. Baccigalupi, M. Ballardini, A. J. Banday, R. B. Barreiro, N. Bartolo, S. Basak, R. Battye, K. Benabed, J. P. Bernard, M. Bersanelli, P. Bielewicz, J. J. Bock, J. R. Bond, J. Borrill, F. R. Bouchet, F. Boulanger, M. Bucher, C. Burigana, R. C. Butler, E. Calabrese, J. F. Cardoso, J. Carron, A. Challinor, H. C. Chiang, J. Chluba, L. P. L. Colombo, C. Combet, D. Contreras, B. P. Crill, F. Cuttaia, P. de Bernardis, G. de Zotti, J. Delabrouille, J. M. Delouis, E. Di

- Valentino, J. M. Diego, O. Doré, M. Douspis, A. Ducout, X. Dupac, S. Dusini, G. Efstathiou, F. Elsner, T. A. Enßlin, H. K. Eriksen, Y. Fantaye, M. Farhang, J. Fergusson, R. Fernandez-Cobos, F. Finelli, F. Forastieri, M. Frailis, A. A. Fraisse, E. Franceschi, A. Frolov, S. Galeotta, S. Galli, K. Ganga, R. T. Génova-Santos, M. Gerbino, T. Ghosh, J. González-Nuevo, K. M. Górski, S. Gratton, A. Gruppuso, J. E. Gudmundsson, J. Hamann, W. Handley, F. K. Hansen, D. Herranz, S. R. Hildebrandt, E. Hivon, Z. Huang, A. H. Jaffe, W. C. Jones, A. Karakci, E. Keihänen, R. Keskitalo, K. Kiiveri, J. Kim, T. S. Kisner, L. Knox, N. Krachmalnicoff, M. Kunz, H. Kurki-Suonio, G. Lagache, J. M. Lamarre, A. Lasenby, M. Lattanzi, C. R. Lawrence, M. Le Jeune, P. Lemos, J. Lesgourgues, F. Levrier, A. Lewis, M. Liguori, P. B. Lilje, M. Lilley, V. Lindholm, M. López-Caniego, P. M. Lubin, Y. Z. Ma, J. F. Macías-Pérez, G. Maggio, D. Maino, N. Mandolesi, A. Mangilli, A. Marcos-Caballero, M. Maris, P. G. Martin, M. Martinelli, E. Martínez-González, S. Matarrese, N. Mauri, J. D. McEwen, P. R. Meinhold, A. Melchiorri, A. Mennella, M. Migliaccio, M. Millea, S. Mitra, M. A. Miville-Deschénes, D. Molinari, L. Montier, G. Morgante, A. Moss, P. Natoli, H. U. Nørgaard-Nielsen, L. Pagano, D. Paoletti, B. Partridge, G. Patanchon, H. V. Peiris, F. Perrotta, V. Pettorino, F. Piacentini, L. Polastri, G. Polenta, J. L. Puget, J. P. Rachen, M. Reinecke, M. Remazeilles, A. Renzi, G. Rocha, C. Rosset, G. Roudier, J. A. Rubiño-Martín, B. Ruiz-Granados, L. Salvati, M. Sandri, M. Savelainen, D. Scott, E. P. S. Shellard, C. Sirignano, G. Sirri, L. D. Spencer, R. Sunyaev, A. S. Suur-Uski, J. A. Tauber, D. Tavagnacco, M. Tenti, L. Toffolatti, M. Tomasi, T. Trombetti, L. Valenziano, J. Valivita, B. Van Tent, L. Vibert, P. Vielva, F. Villa, N. Vittorio, B. D. Wandelt, I. K. Wehus, M. White, S. D. M. White, A. Zacc hei, and A. Zonca. Planck 2018 results. VI. Cosmological parameters. *Astronomy and Astrophysics*, 641:A6, September 2020.
- [13] P. C. Peters. Gravitational radiation and the motion of two point masses. *Phys. Rev.*, 136:B1224–B1232, Nov 1964.
- [14] Ilya Mandel. An accurate analytical fit to the gravitational-wave inspiral duration for eccentric binaries. *Research Notes of the American Astronomical Society*, 2021.
- [15] Andrew R. Wetzel, Philip F. Hopkins, Ji-hoon Kim, Claude-André Faucher-Giguère, Dušan Kereš, and Eliot Quataert. Reconciling Dwarf Galaxies with Λ CDM Cosmology: Simulating a Realistic Population of Satellites around a Milky Way-mass Galaxy. *The Astrophysical Journal Letters*, 827(2):L23, August 2016.
- [16] The LIGO Scientific Collaboration, the Virgo Collaboration, and the KAGRA Collaboration. GWTC-3: Compact Binary Coalescences Observed by LIGO and Virgo During the Second Part of the Third Observing Run. *arXiv e-prints*, page arXiv:2111.03606, November 2021.

Appendix A

BPASS Populations

In this appendix, dozens of theoretical binary systems that generated by the BPASS model are listed in the tables according to their metallicities. There are totally 41755 binary systems provided to this research project by the BPASS model. In details, they can be classified to:

- 41717 *physically possible* samples, for which all columns are real numbers (that is, a few unusable samples have "nan" columns).
- 38802 *statistically possible* samples, for which have non-zeros IMF values.
- 36045 *statistically expected* samples, for which have IMF values $\geq 10^{-6}$. Systems with IMF values below 10^{-6} are extremely rare, binaries beyond this level of weights will be majorly used in our research whenever analysing large samples is feasible.
- 9089 *statistically effective* samples, for which have IMF values ≥ 0.1 . Binary systems with this level of weights are expected to be common in typical galaxies and will be used when analysing median-size samples is appropriate.
- 1654 *statistically significant* samples, for which have IMF values ≥ 0.5 . These systems are very common in typical galaxies, they are used when analysing smaller-size samples is optimal.
- 224 *statistically principal* samples, for which have IMF values ≥ 1 . We will only use these samples when we have to analyse smallest-size populations due to restrictions of resources.

Since the available sample has dozens of thousand expected systems, it is unreasonable and non-applicable to attach and list all generated binaries on this paper. As an optimisation, we only list the top ten theoretical systems with the highest IMF weights for each metallicities. This can be seen as an illustration of what typical binaries of each epoch look like for our major population model. Recall that the IMF value is “the number of systems one would expect for $10^6 M_\odot$ of stars being born”. Hence, these binaries are ranked in terms of their probabilities to exist.

The first column of the table is the IMF weight, the second to the fifth columns are the binary system parameter sets **B**. The sixth column is the evolutionary age of each system, from their initial formation to the asymmetric SN explosion event. The last column is the runaway probability of each system, over distributions of the kick parameter set **w**, computed by using the formula 2.29.

As we can see from below tables (A.1 to A.13), at all metallicities, the most likely compact SNRs (M_3) are neutron stars. This is a direct result of that the initial mass function expects more

lower-mass stars to form. However, the companion compact objects (M_2) have an metallicity-dependent trend. For lower metallicities, which are corresponding to earlier (but not the earliest) stages in the cosmic history, more massive objects like black holes are expected for the candidates of the companion star. Along the increasing of metallicity, more neutron stars are expected, since there are more neutron stars formed at earlier stages, as SNRs from such explosions that previously introduced as kicks.

Table A.1: Population Sample for $Z = 0.00001$

IMF weight	$M_1 (M_\odot)$	$M_2 (M_\odot)$	$\log_{10}(r/R_\odot)$	$M_3 (M_\odot)$	$t_{\text{evo}} (\text{Myr})$	$P_{\text{run}} (\%)$
2.095	2.019	2.213	0.384	1.444	26.00	39.12
2.028	1.612	2.315	0.428	1.440	31.20	37.17
1.607	2.573	2.129	0.380	1.452	22.25	44.40
1.565	4.900	1.266	2.837	1.452	63.88	99.92
1.371	4.228	12.897	2.266	1.466	19.12	94.26
1.371	4.218	12.897	1.999	1.449	19.12	88.03
1.347	4.223	12.886	2.132	1.464	19.12	91.60
1.339	2.072	1.482	1.053	1.440	46.79	78.53
1.269	4.239	13.455	2.419	1.461	19.12	96.18
1.265	3.798	8.157	1.778	1.463	21.80	86.62

Table A.2: Population Sample for $Z = 0.0001$

IMF weight	$M_1 (M_\odot)$	$M_2 (M_\odot)$	$\log_{10}(r/R_\odot)$	$M_3 (M_\odot)$	$t_{\text{evo}} (\text{Myr})$	$P_{\text{run}} (\%)$
1.512	4.308	12.846	2.133	1.456	19.45	91.67
1.478	4.310	12.785	2.264	1.469	19.45	94.29
1.363	3.812	20.750	2.180	1.463	19.51	87.59
1.337	2.709	13.084	2.168	1.441	37.62	92.19
1.322	4.313	13.000	2.404	1.470	19.45	96.17
1.290	4.275	20.293	2.235	1.455	19.48	89.54
1.272	3.893	10.279	1.960	1.454	22.18	89.47
1.265	3.329	17.252	2.882	1.444	37.62	98.80
1.251	3.454	15.851	1.553	1.451	19.57	63.97
1.238	2.109	14.642	1.851	1.442	38.25	80.18

Table A.3: Population Sample for $Z = 0.001$

IMF weight	$M_1 (M_\odot)$	$M_2 (M_\odot)$	$\log_{10}(r/R_\odot)$	$M_3 (M_\odot)$	$t_{\text{evo}} (\text{Myr})$	$P_{\text{run}} (\%)$
1.671	3.382	13.396	1.877	1.455	19.90	83.05
1.664	3.347	13.389	1.745	1.452	19.92	77.35
1.549	3.420	13.437	2.017	1.449	19.88	87.99
1.481	5.574	18.078	2.093	1.480	14.51	86.77
1.449	3.463	13.498	2.163	1.440	19.87	91.84
1.440	5.615	18.828	2.337	1.455	14.52	92.81
1.419	2.740	16.470	2.100	1.447	26.55	87.95
1.384	2.784	17.170	2.285	1.444	26.52	92.37
1.376	1.969	13.696	2.146	1.442	39.38	91.20
1.364	2.275	6.842	1.767	1.440	31.90	88.05

Table A.4: Population Sample for $Z = 0.002$

IMF weight	$M_1 (M_\odot)$	$M_2 (M_\odot)$	$\log_{10}(r/R_\odot)$	$M_3 (M_\odot)$	$t_{\text{evo}} (\text{Myr})$	$P_{\text{run}} (\%)$
1.145	2.660	16.318	2.086	1.444	26.75	87.62
1.124	2.689	16.716	2.251	1.444	26.72	91.86
1.106	5.299	19.038	2.201	1.462	14.50	89.40
1.105	11.611	16.849	1.494	3.975	6.97	61.03
1.042	9.313	13.399	1.437	1.523	8.24	67.15
1.022	4.026	20.327	3.051	1.466	19.87	99.15
1.009	7.304	13.671	1.591	1.484	10.36	71.82
0.989	6.955	22.903	2.437	1.462	11.65	93.23
0.971	6.896	23.094	2.306	1.463	11.65	90.17
0.970	7.011	23.000	2.589	1.469	11.65	95.64

Table A.5: Population Sample for $Z = 0.003$

IMF weight	$M_1 (M_\odot)$	$M_2 (M_\odot)$	$\log_{10}(r/R_\odot)$	$M_3 (M_\odot)$	$t_{\text{evo}} (\text{Myr})$	$P_{\text{run}} (\%)$
9.289	5.832	2.274	0.707	1.467	67.68	72.38
1.321	5.249	18.149	2.394	1.461	14.68	94.14
1.261	5.244	18.208	2.418	1.468	14.53	94.50
1.241	1.831	1.910	0.605	1.442	27.64	51.25
1.187	1.709	2.009	0.467	1.442	27.92	42.20
1.136	5.765	24.318	3.118	1.467	14.50	99.13
1.062	2.429	1.599	1.132	1.449	27.22	81.58
1.025	4.635	20.871	3.053	1.441	26.67	99.12
1.015	4.366	10.795	1.394	1.466	14.59	65.15
1.009	6.846	22.311	2.568	1.474	11.69	95.52

Table A.6: Population Sample for $Z = 0.004$

IMF weight	$M_1 (M_\odot)$	$M_2 (M_\odot)$	$\log_{10}(r/R_\odot)$	$M_3 (M_\odot)$	$t_{\text{evo}} (\text{Myr})$	$P_{\text{run}} (\%)$
5.074	7.357	2.115	0.524	1.507	55.91	77.15
1.605	1.985	1.260	2.574	1.460	72.34	99.80
1.210	1.764	1.940	0.613	1.442	27.78	50.99
1.179	1.882	1.833	0.726	1.444	27.64	58.61
1.173	4.619	13.834	2.026	1.454	14.53	88.04
1.139	4.737	13.352	1.983	1.490	14.51	87.13
1.116	1.668	2.011	0.482	1.440	28.06	42.69
1.111	4.683	13.562	2.136	1.472	14.52	91.24
1.098	3.044	6.761	1.125	1.441	20.20	59.75
1.084	2.091	1.737	0.901	1.442	27.50	69.46

Table A.7: Population Sample for $Z = 0.006$

IMF weight	$M_1 (M_\odot)$	$M_2 (M_\odot)$	$\log_{10}(r/R_\odot)$	$M_3 (M_\odot)$	$t_{\text{evo}} (\text{Myr})$	$P_{\text{run}} (\%)$
3.516	7.323	2.050	0.492	1.503	52.90	77.45
2.328	3.009	2.028	1.575	1.485	19.45	92.99
1.384	2.084	1.772	0.820	1.442	27.75	65.04
1.318	2.965	1.582	0.877	1.451	20.26	72.27
1.306	3.031	1.553	1.026	1.444	20.21	78.74
1.269	1.761	1.915	0.659	1.443	27.93	53.66
1.195	2.865	1.616	0.726	1.451	20.31	65.32
1.159	2.321	1.595	1.128	1.441	27.53	81.32
1.102	4.472	10.638	2.090	1.468	14.47	92.35
1.090	4.535	10.592	2.226	1.447	14.47	94.87

Table A.8: Population Sample for $Z = 0.008$

IMF weight	$M_1 (M_\odot)$	$M_2 (M_\odot)$	$\log_{10}(r/R_\odot)$	$M_3 (M_\odot)$	$t_{\text{evo}} (\text{Myr})$	$P_{\text{run}} (\%)$
6.095	4.600	2.384	0.713	1.523	87.62	66.29
3.294	7.918	2.061	0.514	1.639	57.14	78.34
2.620	2.161	2.217	1.639	1.442	26.10	93.68
2.479	2.808	2.042	1.611	1.441	20.25	93.70
2.017	2.478	2.127	1.622	1.460	22.78	93.58
1.343	1.959	1.849	0.816	1.444	27.90	63.68
1.307	1.878	1.732	0.938	1.443	27.77	70.69
1.193	2.868	1.639	0.807	1.456	20.29	68.51
1.174	2.735	1.703	0.660	1.442	20.37	61.25
1.173	2.568	1.606	0.997	1.442	23.42	76.22

Table A.9: Population Sample for $Z = 0.01$

IMF weight	$M_1 (M_\odot)$	$M_2 (M_\odot)$	$\log_{10}(r/R_\odot)$	$M_3 (M_\odot)$	$t_{\text{evo}} (\text{Myr})$	$P_{\text{run}} (\%)$
3.976	8.114	2.013	0.469	1.917	55.95	76.42
3.889	11.121	1.400	0.998	1.442	20.18	90.59
3.579	7.693	1.400	0.948	1.444	41.71	86.01
3.469	10.229	1.400	0.987	1.499	23.39	89.33
2.895	8.514	1.400	0.961	1.445	33.27	87.34
2.545	11.933	1.400	1.008	1.493	17.81	91.14
2.224	13.605	1.400	1.028	1.496	14.45	92.51
1.720	12.741	1.400	1.018	1.500	15.92	91.82
1.240	1.781	1.811	0.935	1.441	27.84	69.68
1.213	15.481	1.400	1.053	1.535	11.44	93.60

Table A.10: Population Sample for $Z = 0.014$

IMF weight	$M_1 (M_\odot)$	$M_2 (M_\odot)$	$\log_{10}(r/R_\odot)$	$M_3 (M_\odot)$	$t_{\text{evo}} (\text{Myr})$	$P_{\text{run}} (\%)$
3.926	2.735	1.675	0.794	1.457	20.91	67.12
3.673	9.136	2.022	0.527	3.052	54.75	68.71
2.871	5.978	2.084	0.557	1.502	66.96	71.60
1.360	2.819	1.521	1.040	1.449	20.48	79.08
1.277	2.370	1.652	0.992	1.443	23.87	75.21
1.261	2.872	1.496	1.188	1.453	20.43	84.76
1.261	2.728	1.575	0.886	1.457	20.54	71.90
1.202	1.976	1.814	0.810	1.448	23.96	63.66
1.184	1.763	1.940	0.963	1.442	28.46	70.16
1.149	2.484	1.563	1.150	1.444	23.80	82.61

Table A.11: Population Sample for $Z = 0.02$

IMF weight	$M_1 (M_\odot)$	$M_2 (M_\odot)$	$\log_{10}(r/R_\odot)$	$M_3 (M_\odot)$	$t_{\text{evo}} (\text{Myr})$	$P_{\text{run}} (\%)$
3.418	6.237	2.022	0.550	1.469	54.58	73.57
2.265	5.977	2.249	0.705	1.449	78.56	73.23
2.195	8.993	2.088	0.577	3.088	63.12	67.85
1.329	2.519	1.559	0.762	1.467	20.35	65.55
1.226	2.334	1.528	0.636	1.457	20.44	59.07
1.220	2.742	1.516	0.939	1.469	20.28	74.57
1.197	2.029	1.853	0.753	1.465	23.80	60.41
1.135	2.144	1.732	0.888	1.450	23.71	68.93
1.134	1.652	1.527	0.723	1.443	28.49	59.73
1.117	1.900	1.488	0.610	1.461	23.93	55.22

Table A.12: Population Sample for $Z = 0.03$

IMF weight	$M_1 (M_\odot)$	$M_2 (M_\odot)$	$\log_{10}(r/R_\odot)$	$M_3 (M_\odot)$	$t_{\text{evo}} (\text{Myr})$	$P_{\text{run}} (\%)$
2.996	10.280	1.400	0.998	1.482	19.01	89.54
2.814	8.767	1.400	0.975	1.470	26.47	87.66
2.770	8.171	1.994	0.557	2.366	82.43	72.21
2.514	7.352	1.259	3.378	1.440	41.08	99.99
2.174	7.346	1.400	0.949	1.444	41.11	85.48
1.792	11.083	1.400	1.009	1.452	16.63	90.55
1.669	6.317	2.283	0.709	1.478	87.82	74.00
1.439	6.263	1.400	0.872	1.453	32.32	82.22
1.357	5.010	1.906	0.483	1.485	69.04	67.02
1.324	12.660	1.400	1.028	1.473	13.37	91.90

Table A.13: Population Sample for $Z = 0.04$

IMF weight	$M_1 (M_\odot)$	$M_2 (M_\odot)$	$\log_{10}(r/R_\odot)$	$M_3 (M_\odot)$	$t_{\text{evo}} (\text{Myr})$	$P_{\text{run}} (\%)$
2.368	5.779	1.963	0.549	1.483	63.07	71.69
2.240	8.516	1.400	0.976	1.467	25.33	87.35
2.149	9.195	1.400	0.986	1.470	21.24	88.30
1.872	9.416	1.259	3.714	1.451	20.73	100.00
1.871	9.409	1.259	3.581	1.443	20.74	99.99
1.861	9.409	1.259	3.447	1.443	20.74	99.99
1.621	5.282	1.400	0.841	1.442	39.37	79.37
1.370	10.735	1.400	1.009	1.445	15.91	90.26
1.339	7.813	1.400	0.961	1.451	30.90	86.31
1.215	11.520	1.400	1.019	1.470	14.11	90.91

Appendix B

Additional Methods

We are going to give several methods that we have used in our research, but for some reasons that have not been covered and explained in details in the main chapters.

B.1 Codes

The final version of the notebook of our Python codes has been published on Kaggle website via the following link:

- <https://www.kaggle.com/code/jsun419/phys-789-v3-0/notebook>

The published date of codes is 06th June 2022. The majority of our programs and outcomes can be found in this notebooks in details.

B.2 Keep-only algorithm

When we are computing a long array and we want to keep only the values for a certain continuous interval $[b, a]$ ($b < a$), using `if` loops or `while` loops will not work properly. So we want to figure out a simple mathematical algorithm to keep only the values we want without using any statements. Furthermore, for dimensional completeness, we want to transform the values we do not want into "nan" (abbreviation for "not a number").

One coding trick is that without specifying, the program will recognise complex numbers as "nan". So for a basic example, if we want to keep only positive numbers of an array x and turn all its negative numbers into "nan", we can use $\langle x \rangle \equiv (\sqrt{x})^2$. Similarly, if we want to keep all values above a number b , we can use $\langle x - b \rangle + b$ to do so. If we want to keep all values below a number a , we can use $a - \langle a - x \rangle$ to do so. Together, if we want to keep all values in an interval $[b, a]$ and turn all other values into "nan", one can use $K(x, a, b) = a - \langle a - \langle x - b \rangle - b \rangle$. In coding form, this is given by `Keep_Only(x,a,b) = a-np.sqrt(a-np.sqrt(x-b)**2-b)**2`.

B.3 Determination of true peaks of the formation time

The formation history is determined by the Milky Way on Feedback in Realistic Environments (FIRE) simulation provided by Latte Project [15]. However, the given data only contains information of mass yields at time bins, it dose not directly indicate a typical formation time point for each metallicities. Thus, we need to figure out an algorithm to transform the distribution into a single number, similar to the relationship between MB distribution and the root-mean-square

width. For simplicity, we choose to find the true single peaks for each mass distributions, and use the corresponding time point at those peaks as our typical formation time $T_{\text{for}}(Z)$.

For each metallicities, they have similar shapes of mass distributions over $\log_{10}(\text{time})$, and they all have a single global maximum, at some discrete time bin. But the time bins are given in the steps like 9.8, 9.9, 10.0 etc. Since these are values of $\log_{10}(\text{time})$, a tiny difference can cause a great difference of billion years in the formation history, so to reach an acceptable accuracy, we cannot directly use the discrete peaks and we will use a mathematical approximation to find the actual peaks. Even we cannot use discrete peaks, we are confident about the fact that the true peaks must lie in one side closed to the discrete peaks. Our method is to pick up three values, the discrete peak and the two values beside it. We assume that in this neighborhood, the true peak can be approximated as a quadratic function $m(t) = -a(t - t_0)^2 + b$. A simple mathematical theorem is that “any three points on a plane could determine a quadratic function”, thus we can use `curve_fit` function from `scipy.optimize` on Python to fit an exact value of t_0 , and this is the location of the true peak.

B.4 Data reduction process of printed outcomes

After we print the giant matrix (as described in Section 2.5.3) of τ as a file, we may reduce the size of the file for accelerating the processing speed. The downloaded file which includes the giant matrix should be in the format of text (`.txt`), CSV (`.csv`) or data (`.dat`). For accessibility, we used text files. The recommended delimiter is comma `,`. In our practice, we have 450 sets of kick parameters and 36045 sets of binary system parameters, and the generated text file is about 66.5 MB.

Recall that the majority of the giant matrix are "nan". Thus the first quick operation we can take is to replace `nan` with a single irrelevant character. In our practice, we use the English letter "`z`". This optimisation can be simply done by `edit/replace` function of the notepad on any computer system. The next powerful tool is Excel. We then import the text file with `delimiter = ','` in Excel. We start by setting all cells in the format of scientific notation. Since the data importation will automatically set the widths of the columns, we are able to observe that a lot of columns have obviously narrower widths compare to other columns, as shown in Figure B.1. This is because there are no numbers in those columns (that is, there are only "nan"). We are confident with this conclusion as scientific notation ensures any number will appear with the same length.

E	F	G	H	I	J	K	L	M
z	z	z	z	z	z	z	z	
z	z	z	z	z	z	z	z	
z	z	z	z	z	z	z	z	
z	z	z	z	z	z	z	11701.74781362	6157.17832729
z	z	z	z	z	z	z	11759.00955874	6755.44376524
z	z	z	z	z	z	z	z	
z	z	z	z	z	z	z	z	
z	z	z	z	z	z	z	z	
z	z	z	z	z	z	z	z	

Figure B.1: A screenshot of what a tabulated giant matrix looks like in Excel. Some columns like F to K have obviously narrower widths, these columns have no real values and full of "z".

Before we delete these "nan"-only columns, we need to arrange index (remember, both row and column index run from 0 rather than 1) to each row and columns. After we correspond these parameter indexes for each rows and columns, we can delete those narrower columns. Then

reduce the rows. We can use the `sum` function to sum all numbers of a row to see if there are any numbers in a certain row (be careful, do not include the index column to the `sum` function). Since any entry can be either a positive value or an "`nan`", if the sum of a row is zero, it means the row must contain no numbers. Then use the `rank` function of Excel to rank these sums from high to low, and next we are able to delete all rows with zero sums at once. Then rank again but with respect to the row index. The remain reduced giant matrix is what we want and what we are going to use. The final size of our exported text file has been reduced to 15.7 MB, a reducing efficiency of 76.4% is observed.

Appendix C

All Plots of Distributions

Here we attach all plots yielded for Section 3.1.2 and 3.1.3. Same as the original sequence that we describe our results for eccentricity distributions first then velocity distributions, in this appendix, we list the eccentricities (Figure C.1 to C.10) first, then velocities (Figure C.11 to C.23). The full results of velocities run over the whole domain, from $\theta = 0^\circ$ to $\theta = 180^\circ$ with a step size of 15° . However, since eccentricities are mainly used to investigate influences of ϕ -families, and effects of ϕ^* tend to be negligible when $\sin \theta \rightarrow 0$, eccentricity plots run only from $\theta = 30^\circ$ to $\theta = 165^\circ$ with the same step size of 15° .

Each of figures has four panels, the upper two assume constant Hobbs' kick $w = 265$ km/s, and the lower two assume Bray's kick with $\alpha = 100$ km/s and zero β , that is $w = 100(m_1 - 1)$ km/s. The left two are distributions with respect to primary star mass M_1 , while on the right-hand-side are with respect to pre-SN separation r . Each of panels has a black dashed reference line. For eccentricities, this line is a boundary line of $e = 1$, all data points below this line represent a bounded system (of $e < 1$), all above dots are unbounded (of $e \geq 1$). For velocities, this line is a unit line of the pre-SN orbital velocity for each system (keep in mind in the context, when we say “velocities”, we mean a reduced velocity that divided by its pre-SN orbital velocity v , as a velocity ratio). So all velocities below this unit line means their velocities of this kind is lower than its pre-SN orbital velocity, while over the line means its final velocity is greater than before. More details were described in Section 3.1.2 and 3.1.3. In additional to eccentricity plots, we will also record the *IMF-weighted overall runaway probability* for Hobbs' \mathcal{R}_H and Bray's kick \mathcal{R}_B in each velocity figure at each θ .

For eccentricity plots, we used statistically significant (1654 systems of $\text{IMF} \geq 0.5$) samples for clarity. Specifically, they have five types of data points at each panel, red plus for $\phi^* = 0^\circ$ ($c_2 = 1$), yellow for $\phi^* = 30^\circ$ ($c_2 = 0.75$), green for $\phi^* = 45^\circ$ ($c_2 = 0.5$), blue for $\phi^* = 60^\circ$ ($c_2 = 0.25$) and magenta for $\phi^* = 90^\circ$ ($c_2 = 0$). In general, in considering their physical relationship to Q and e , we would expect for all cases, with a higher ϕ^* , its eccentricity will be further from the $e = 1$ boundary line than lower ϕ^* .

And for reduced final velocities (RFVs), we used statistically effective (9089 systems of $\text{IMF} \geq 0.1$) samples for sufficiently representative distributions. Specifically, we put all three types of final velocities in the same plot, both unbounded two types and bounded systematic velocities. For disrupted cases, yellow plus for RFVs of SN compact remnants $\eta_3 = |\boldsymbol{\eta}_3|$ (Eq 2.19) and blue plus for RFVs of the pre-exist compact objects $\eta_2 = |\boldsymbol{\eta}_2|$ (Eq 2.20); for survival cases, there is only one type of RFV which is the systematic velocity η_{sys} (Eq 2.21) as a result of conservation of momentum, represented by red pluses. Again from physical relationships, we expect a stronger linearity for RFVs when versus the pre-SN separation r .

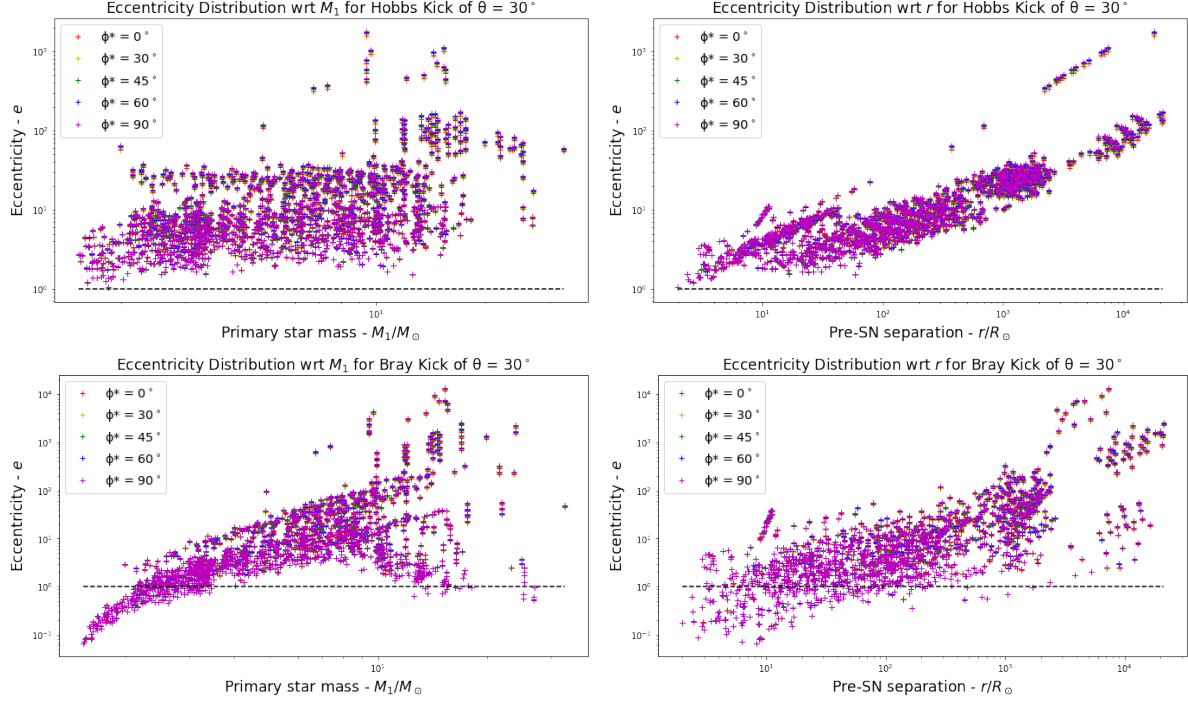


Figure C.1: The Hobbs' model shows no clear pattern with respect to primary star mass M_1 , but Bray's kick show a weak logarithm relationship with respect to M_1 , this is because a Bray's kick is M_1 -dependent. Both kick models' eccentricities show a linearity when versus separation r , Hobbs' linearity (upper right) is stronger but Bray's one (lower right) is weaker.

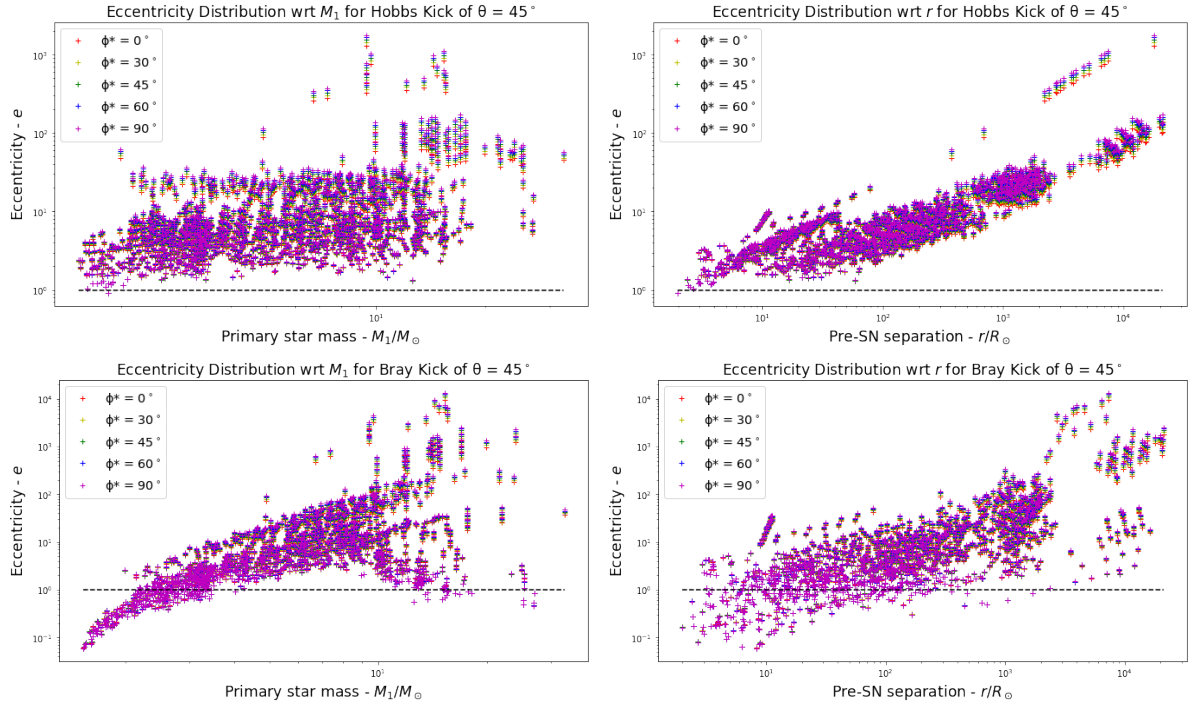


Figure C.2: General patterns remain. Unlike for $\theta \leq 30^\circ$, the contributions of ϕ^* start being remarkable for large eccentricities, with keeping linearity for Hobbs' kick with respect to r (upper right).

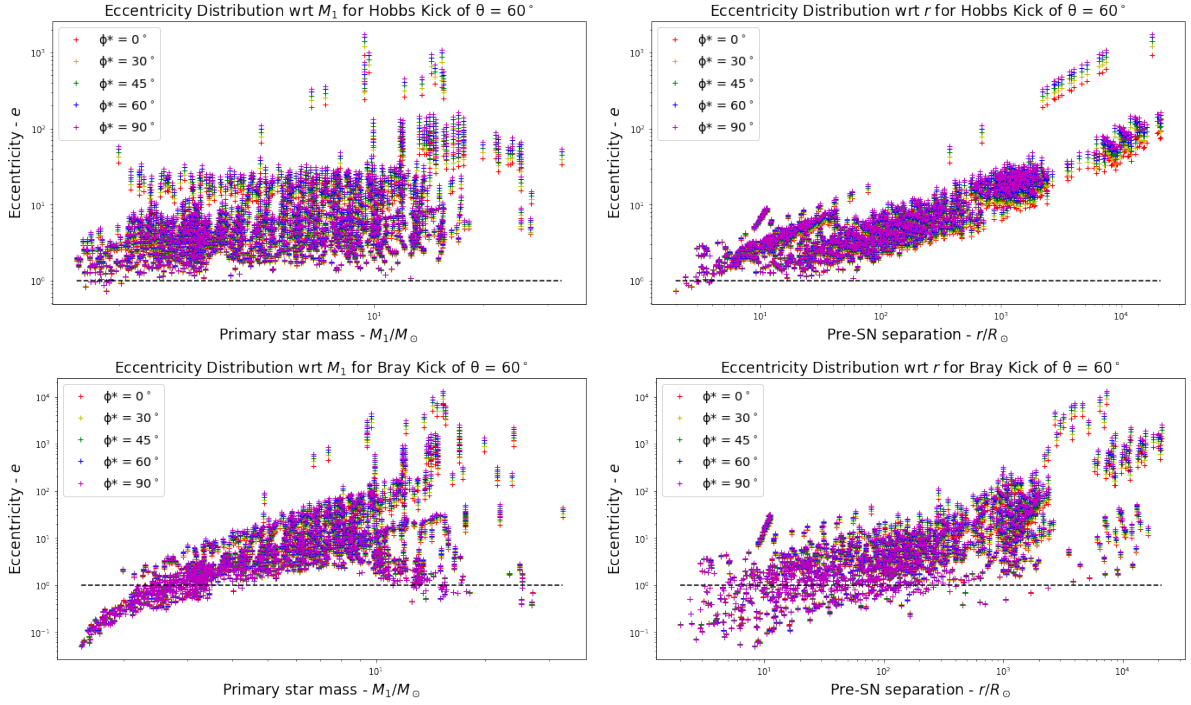


Figure C.3: General patterns remain. The contributions of ϕ^* keep growing for relatively high eccentricities, while more systems start crossing the $e = 1$ boundary line (black dashed), especially for Hobbs' model.

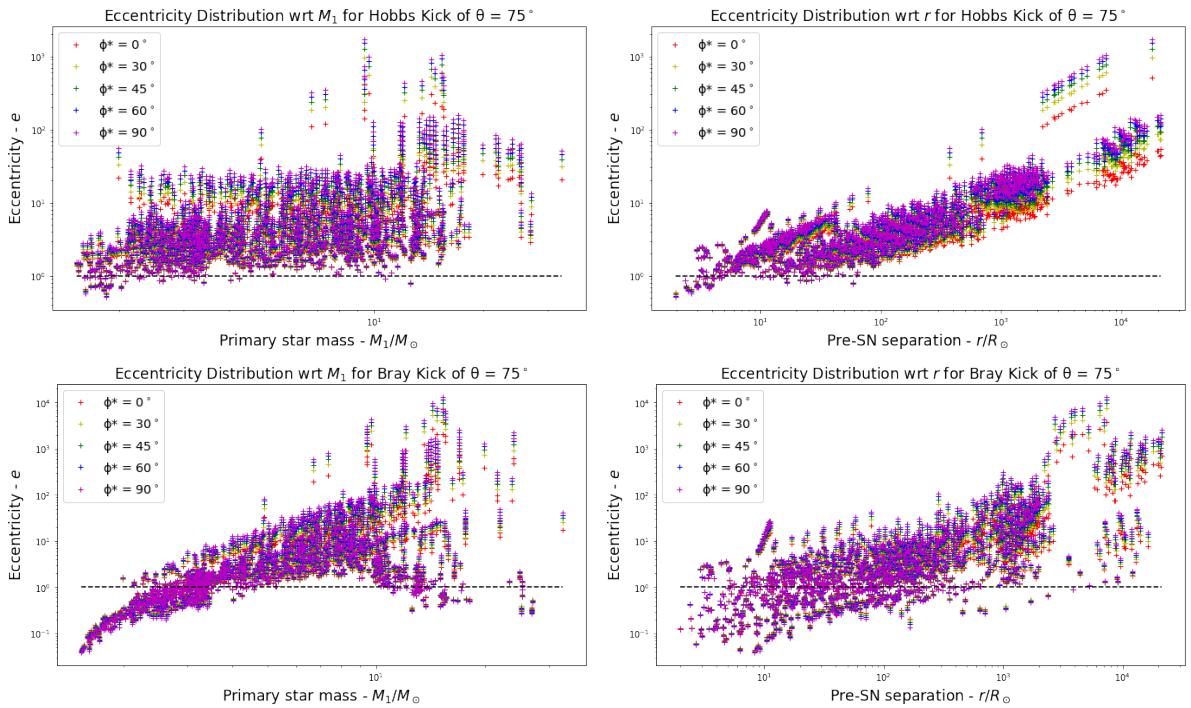


Figure C.4: General patterns remain. The effects of ϕ^* are clear for $e > 2$, that with a higher ϕ^* will imply a higher final eccentricity.

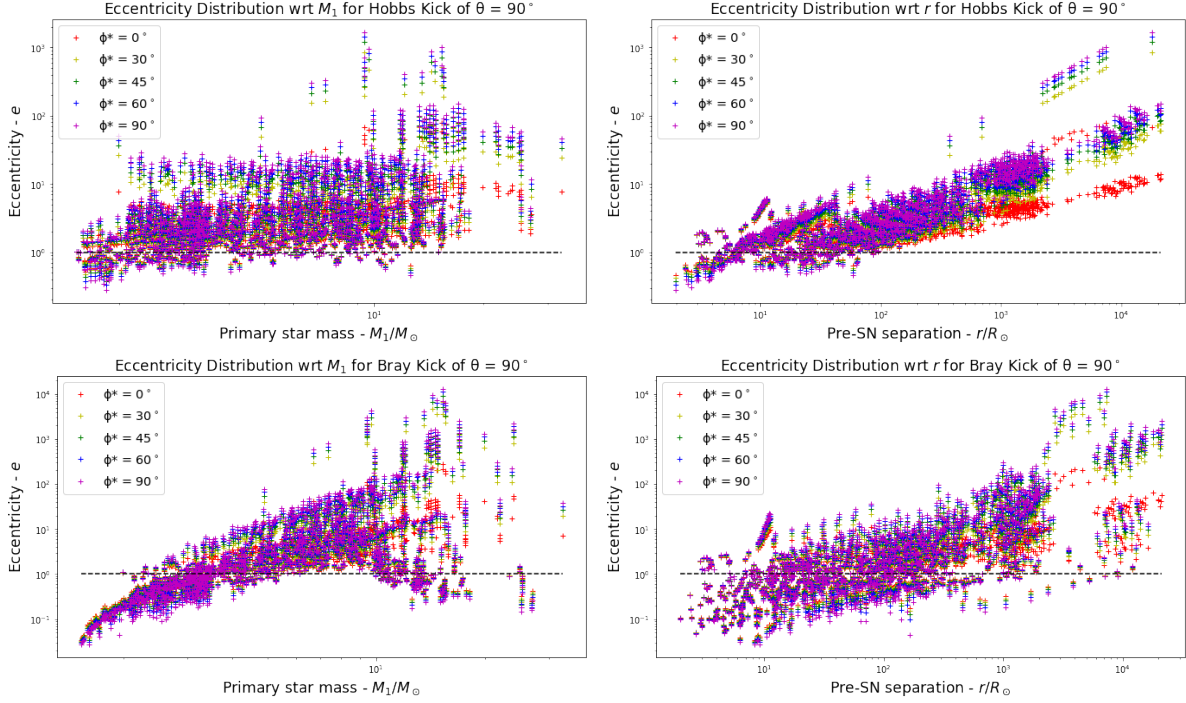


Figure C.5: General patterns start changing. For both kicks, linearity for $\phi^* = 0^\circ$ with respect to r is breaking down, especially for $e \sim 10$. Furthermore, influences caused by ϕ^* begin to reveal for all survival systems (for $e < 1$, the populations below the black dashed line).

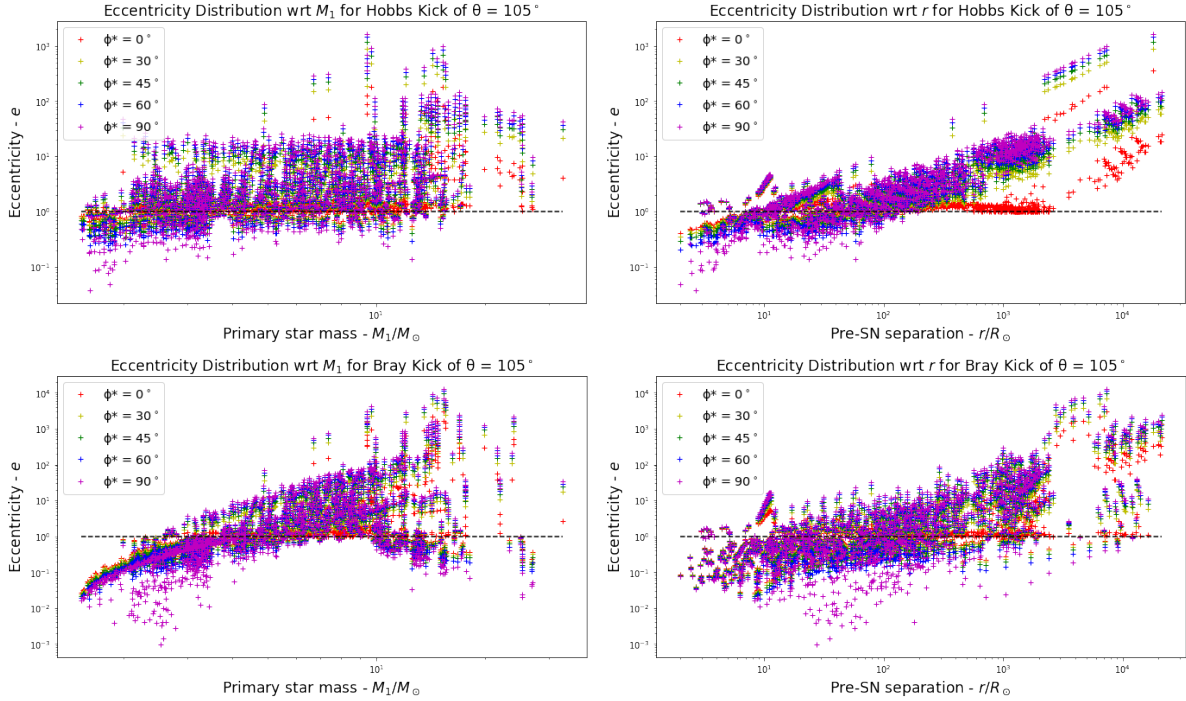


Figure C.6: General patterns change apparently. Much more binaries become bounded, for both bounded and unbounded systems, their eccentricities of $\phi^* = 0^\circ$ get closer to the $e = 1$ line (black dashed), except for those have very high eccentricities. Both kick models predict specially lower eccentricities at $\phi^* = 90^\circ$ that closed to zero.

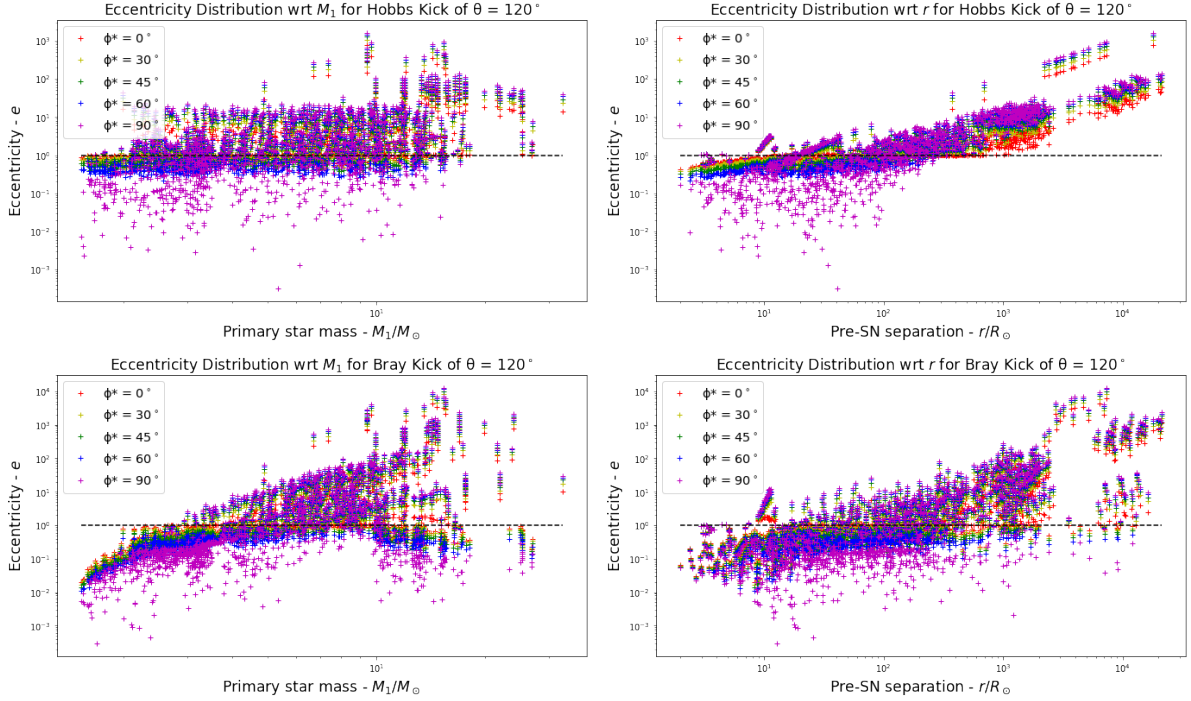


Figure C.7: The general trends from previous figure keep growing. Linearity versus r is recovering, and much more survival binaries have lower eccentricities $e \leq 0.1$ for Hobbs' kick at $\phi^* = 90^\circ$, for Bray's kick this result even gets lower. For all survivors with $\phi^* \leq 60^\circ$, Hobbs' model predicts their eccentricities lie in $0.2 \leq e < 1.0$, but Bray's kick predict a much lower bound at $e \sim 0.01$ for lowest M_1 systems.

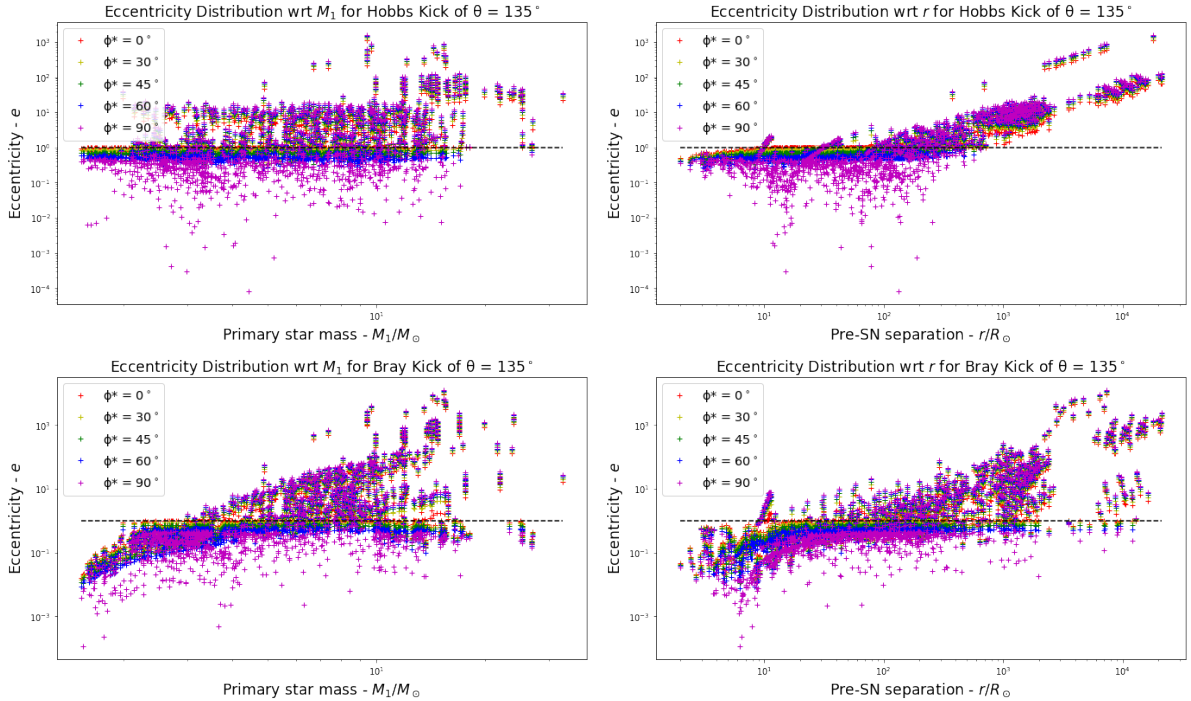


Figure C.8: As increasing of θ , the linearity recovers for Hobbs with higher r (upper right), and all dots get closer, except for the extremely lower e systems that in the bottom of each panel. An interesting result is now the lowest bound for Hobbs's kick is lower than for Bray's.

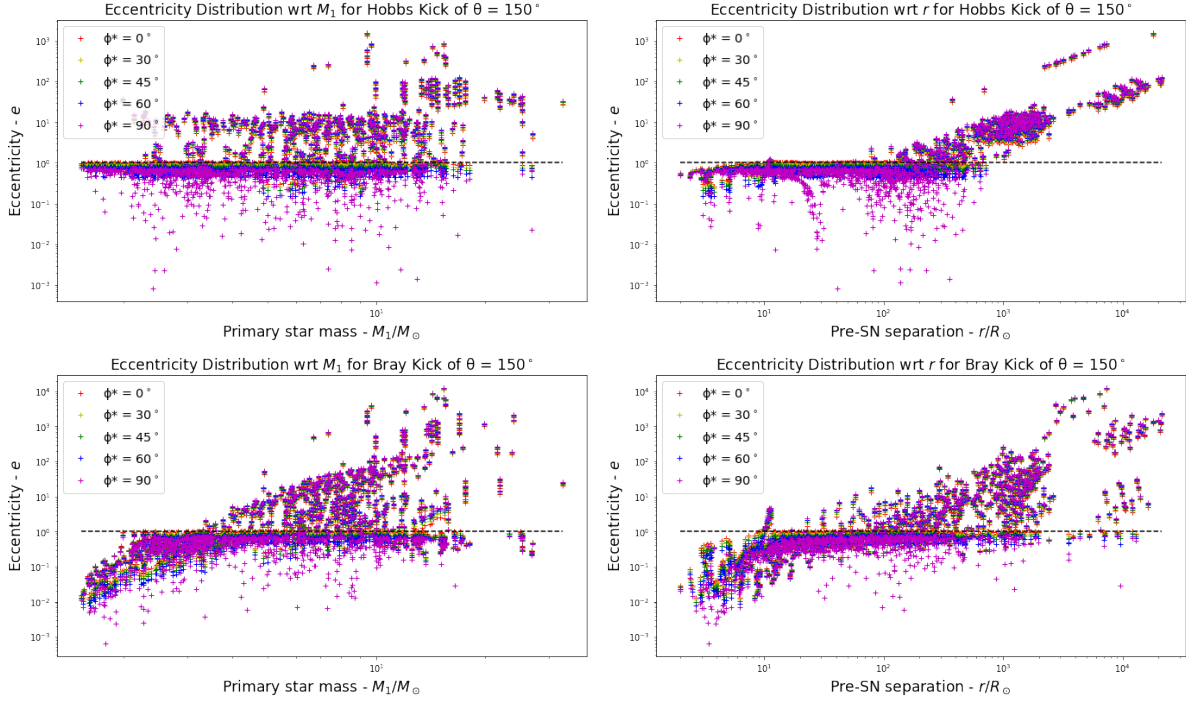


Figure C.9: At $\theta = 150^\circ$, its $\sin \theta$ is the same as for $\theta = 30^\circ$, so for majority systems we would expect they have a compact relationship over ϕ^* . But different from $\theta = 30^\circ$, we have a remarkable amount of survivors who have lower eccentricities closed to zero at $\theta^* = 90^\circ$, since the effects $\cos \theta$ keep growing.

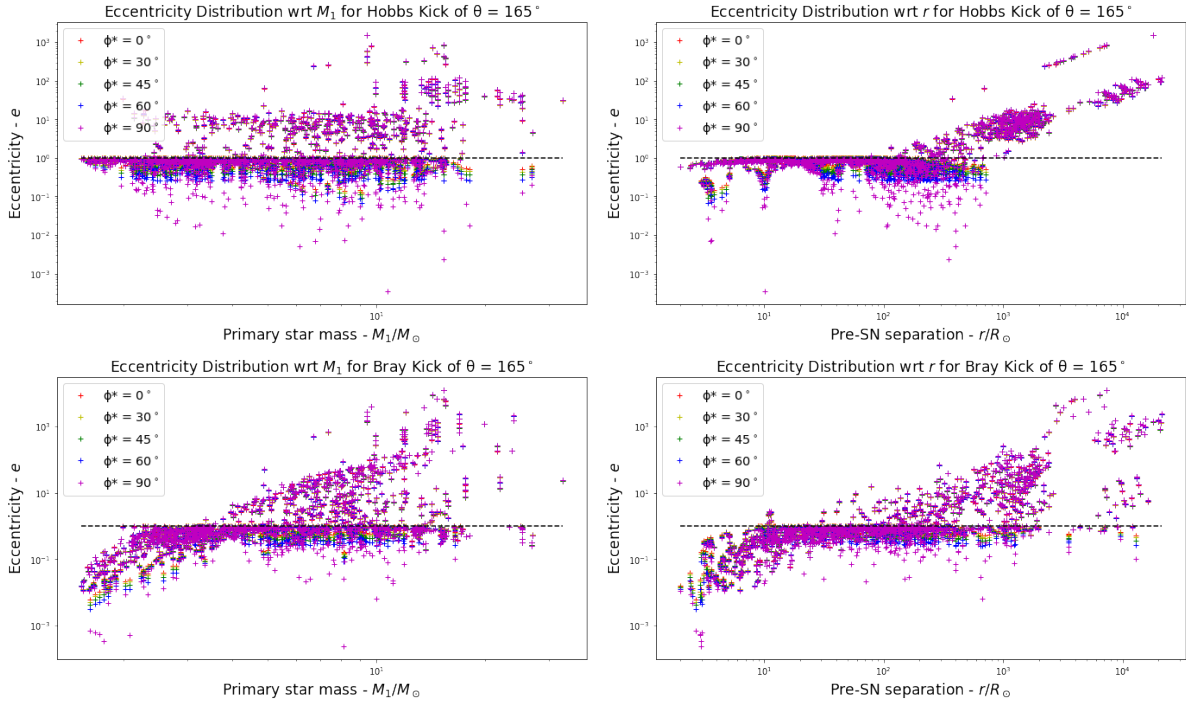


Figure C.10: For both kick models, systems above the boundary line (black dashed) have coincident eccentricities over ϕ^* , and for majority of survivors, they have $e \geq 0.1$, but there are still extremely lower eccentricities.

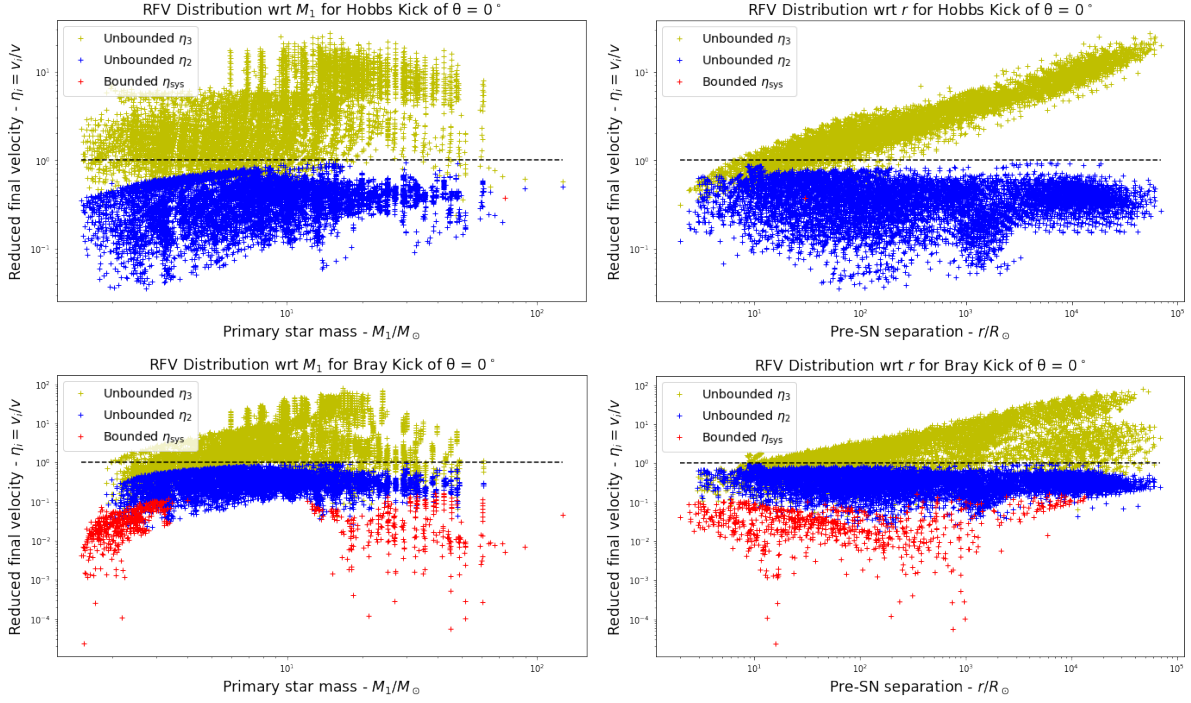


Figure C.11: $\mathcal{R}_H = 100.0\%$ and $\mathcal{R}_B = 89.93\%$. Bray's kick model apparently predicts more survival systems (red) with very lower and very higher M_1 , but with specially lower systematic velocities. Only one system survives for Hobbs' kick, it has a very high M_1 .

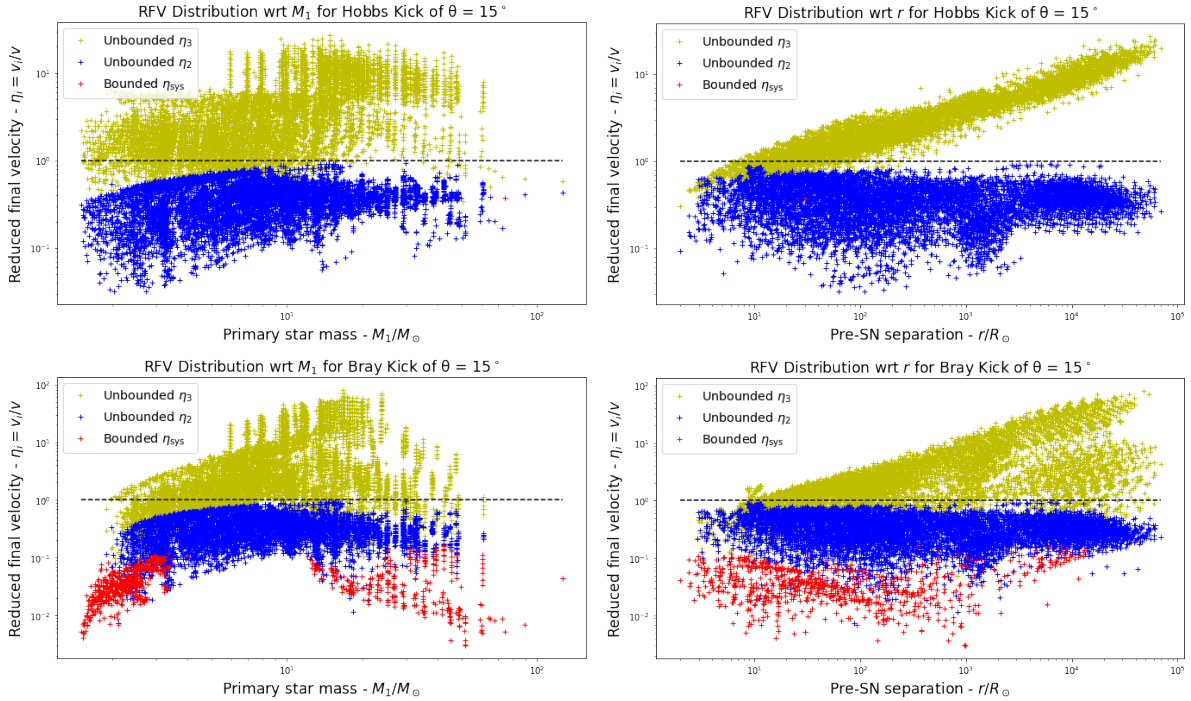


Figure C.12: $\mathcal{R}_H = 100.0\%$ and $\mathcal{R}_B = 89.59\%$. The general patterns remain as for 0° . The same only one survivor (red) for Hobbs' kick, but this time the survivors for a Bray's kick have higher systematic velocities.

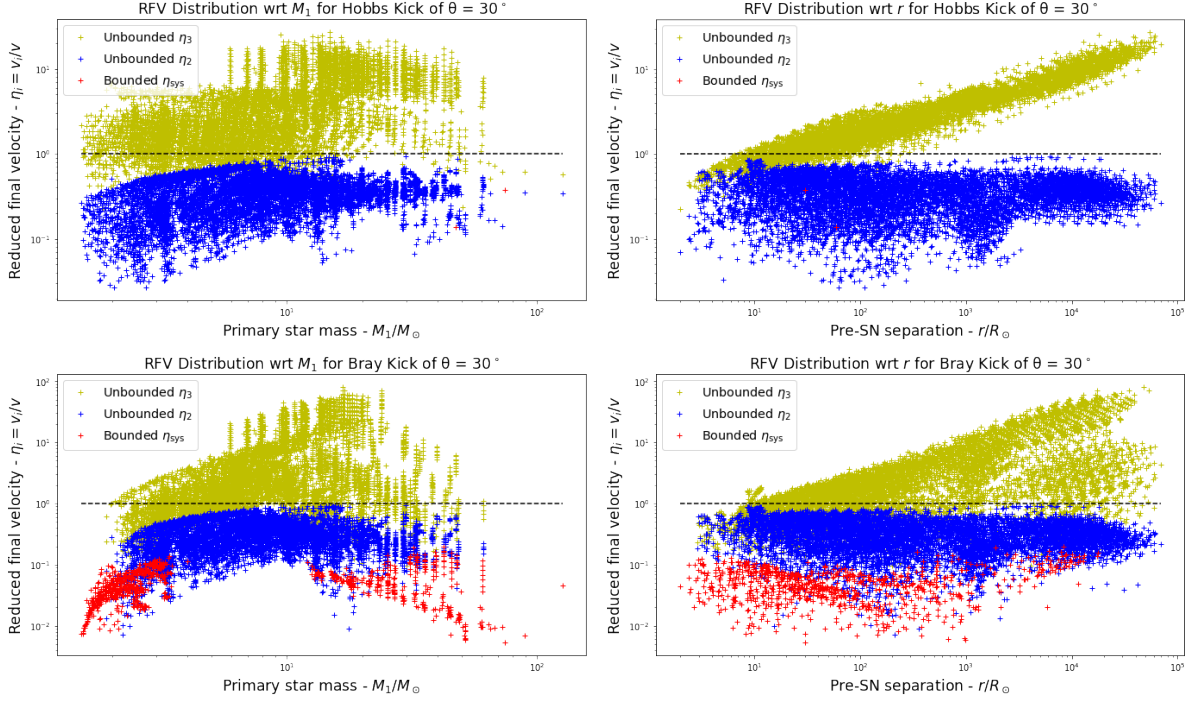


Figure C.13: $\mathcal{R}_H = 99.99\%$ and $\mathcal{R}_B = 88.56\%$. General patterns remain. One more similar survivor (red) appears for Hobbs' kick, Bray's survivors get a little bit more compact in final systematic velocities (red).

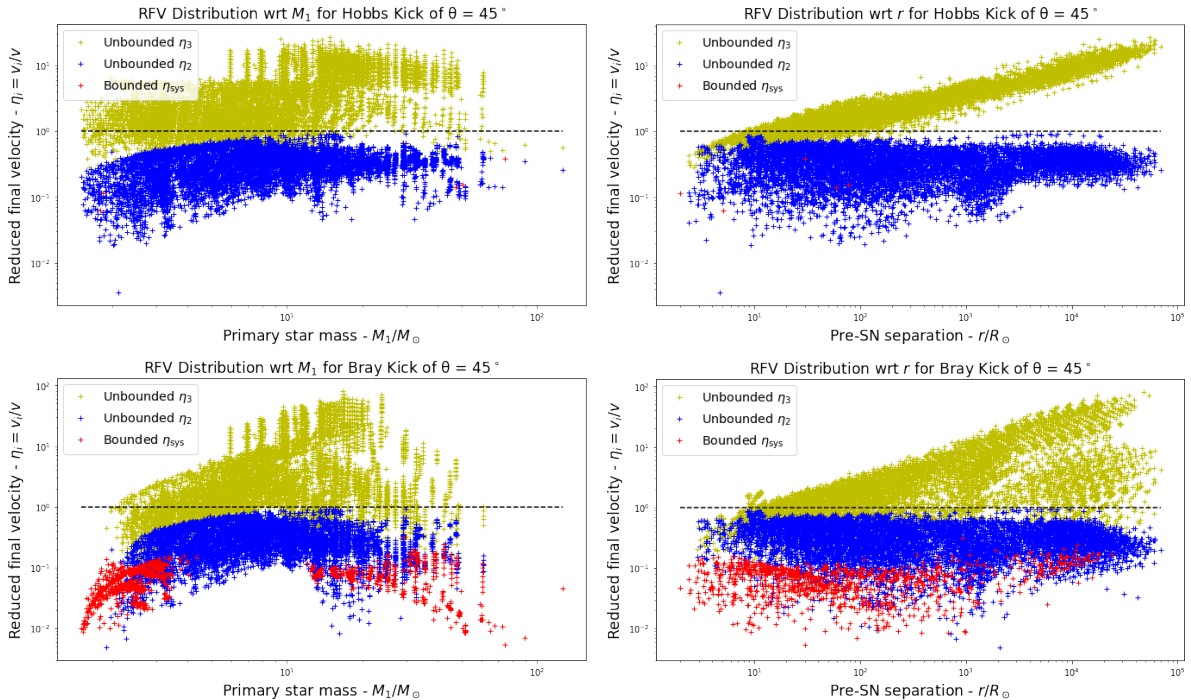


Figure C.14: $\mathcal{R}_H = 99.95\%$ and $\mathcal{R}_B = 86.36\%$. General patterns remain. For Hobbs' kick model, one more survivor (red) similar to previous two appears, but two more survivors of a new type (NS) also arise.

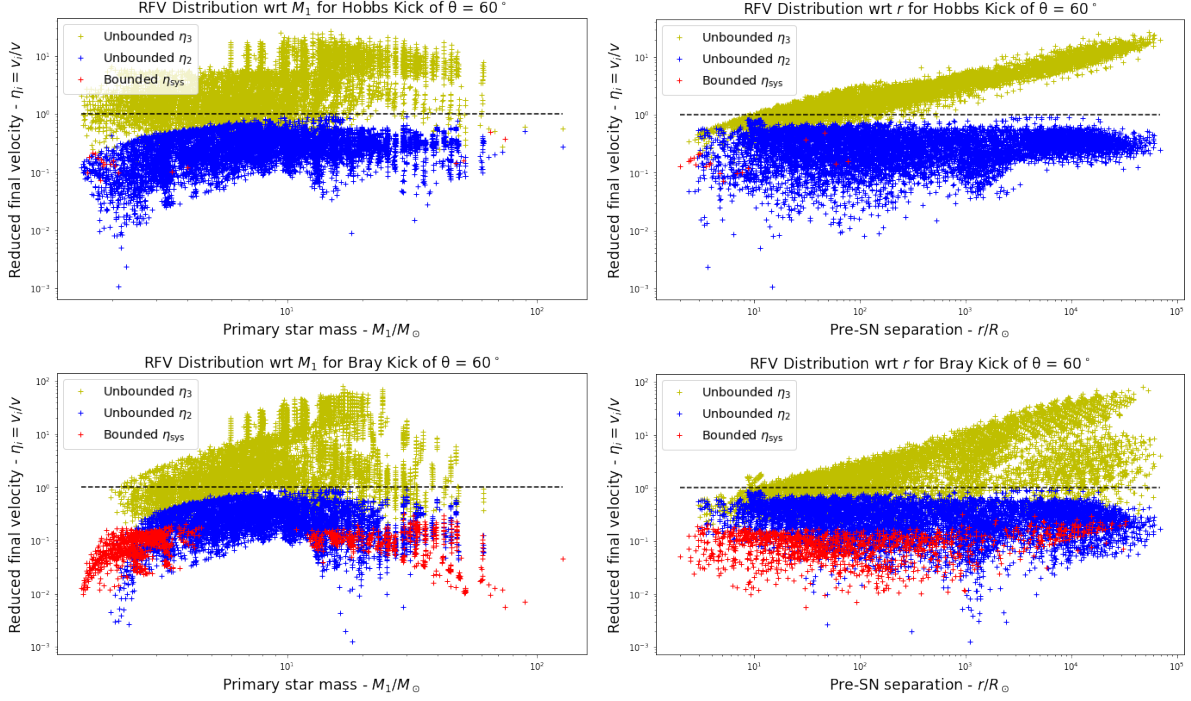


Figure C.15: $\mathcal{R}_H = 99.61\%$ and $\mathcal{R}_B = 82.86\%$. General patterns remain but start changing. Survivors (red) for both kick models keep increasing, but the disrupted final velocities (blue) of the companion star begin reaching lower ratios.

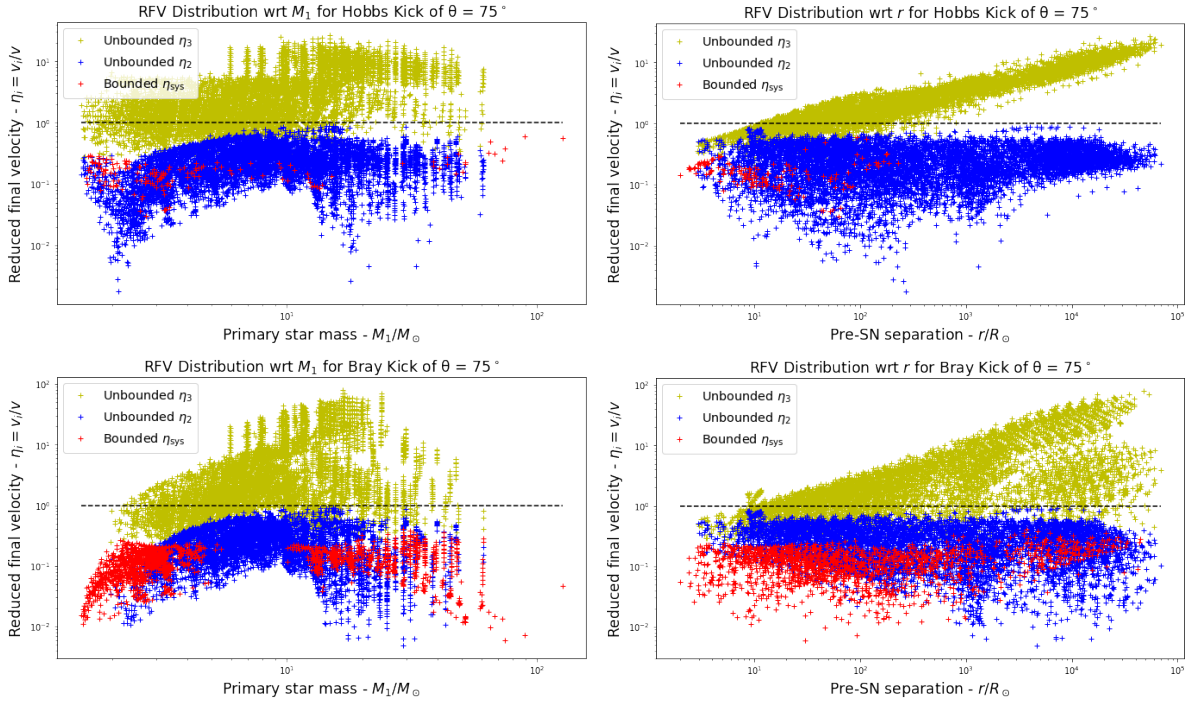


Figure C.16: $\mathcal{R}_H = 97.86\%$ and $\mathcal{R}_B = 77.46\%$. General patterns slightly change. More survivors (red), but for the Hobbs' kick, systems of both lower and higher M_1 can survive the SN explosion, but only with lower pre-SN separation.

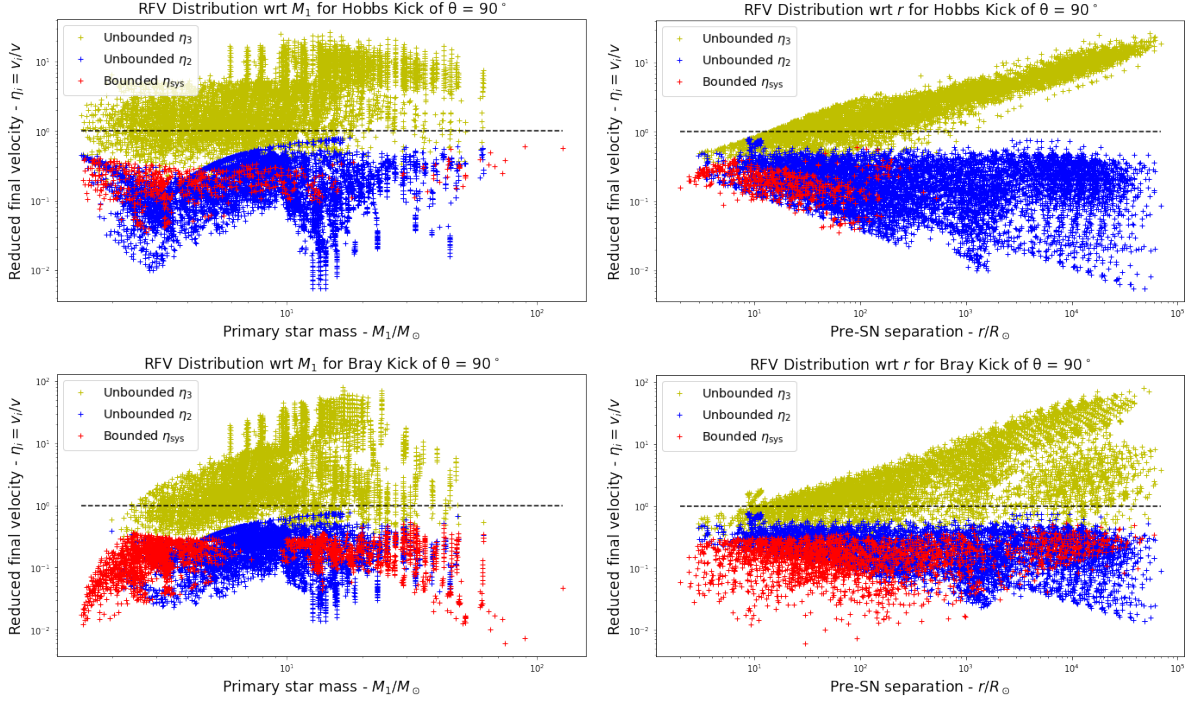


Figure C.17: $\mathcal{R}_H = 92.05\%$ and $\mathcal{R}_B = 69.43\%$. General patterns change. A valley (blue) forms at $M_1 \approx 3M_\odot$ for Hobbs' kick, both kick models' disrupted companion velocities (blue) show a new weak linearity with respect to r .

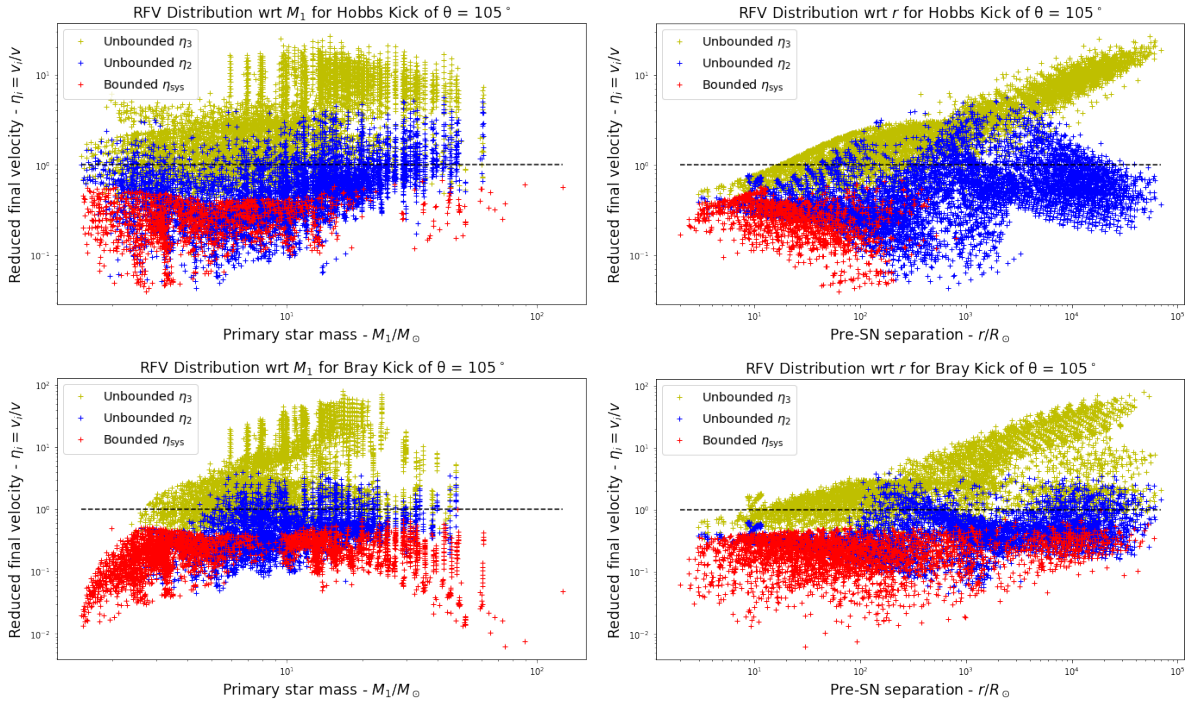


Figure C.18: $\mathcal{R}_H = 80.42\%$ and $\mathcal{R}_B = 59.07\%$. General patterns apparently change. It is the first time that the final velocity of companions (blue) of disrupted case beyond their pre-SN orbital velocities (black dashed line), with high ratios.

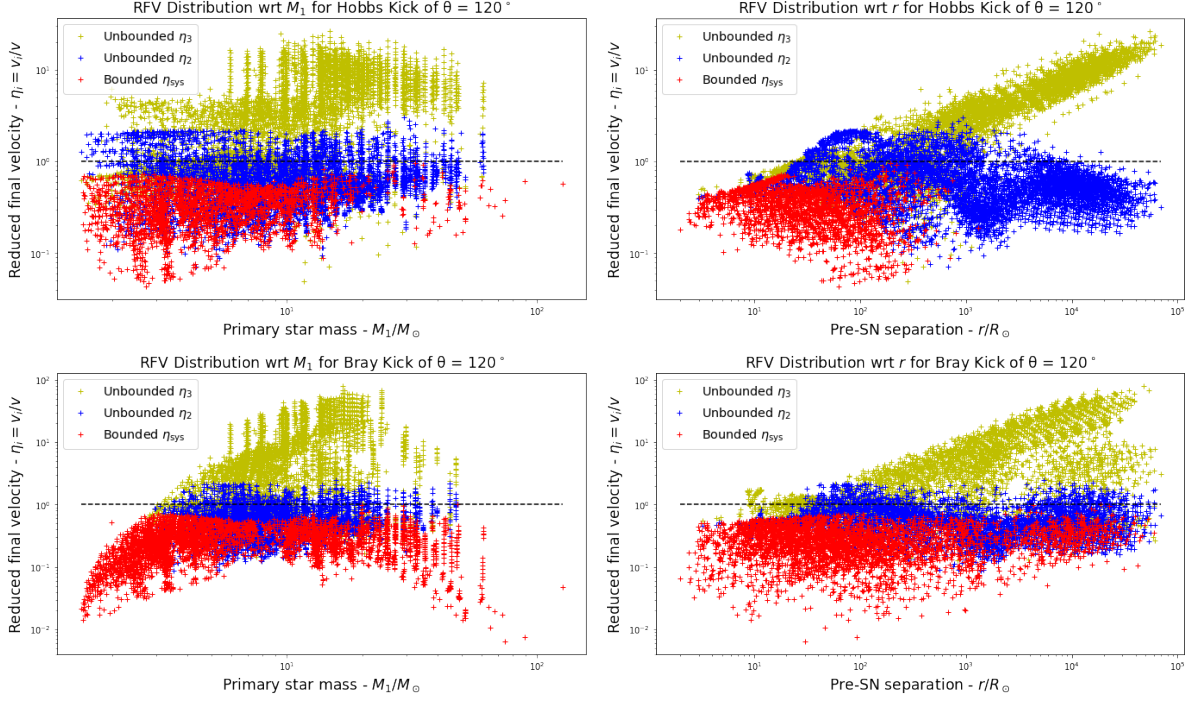


Figure C.19: $\mathcal{R}_H = 64.87\%$ and $\mathcal{R}_B = 48.28\%$. General patterns get flatter than for $\theta = 105^\circ$. Slightly more companion velocities (blue) over the pre-SN orbital velocity line (black dashed), but get moderate in ratios.

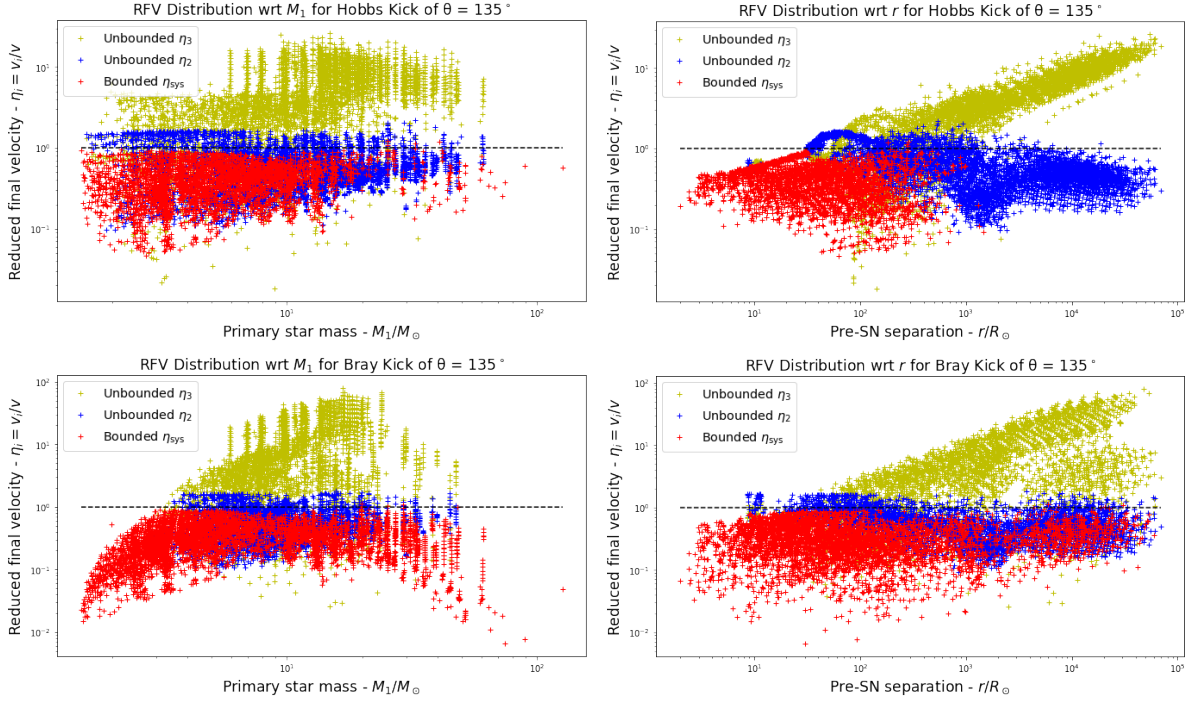


Figure C.20: $\mathcal{R}_H = 51.90\%$ and $\mathcal{R}_B = 40.98\%$. General patterns similar to previous one. Survival population (red) reaches about a half for both kick models. For the first time, a few survival systematic velocities beyond the unit line (black dashed). Companion velocities (blue) get more moderate in ratios.

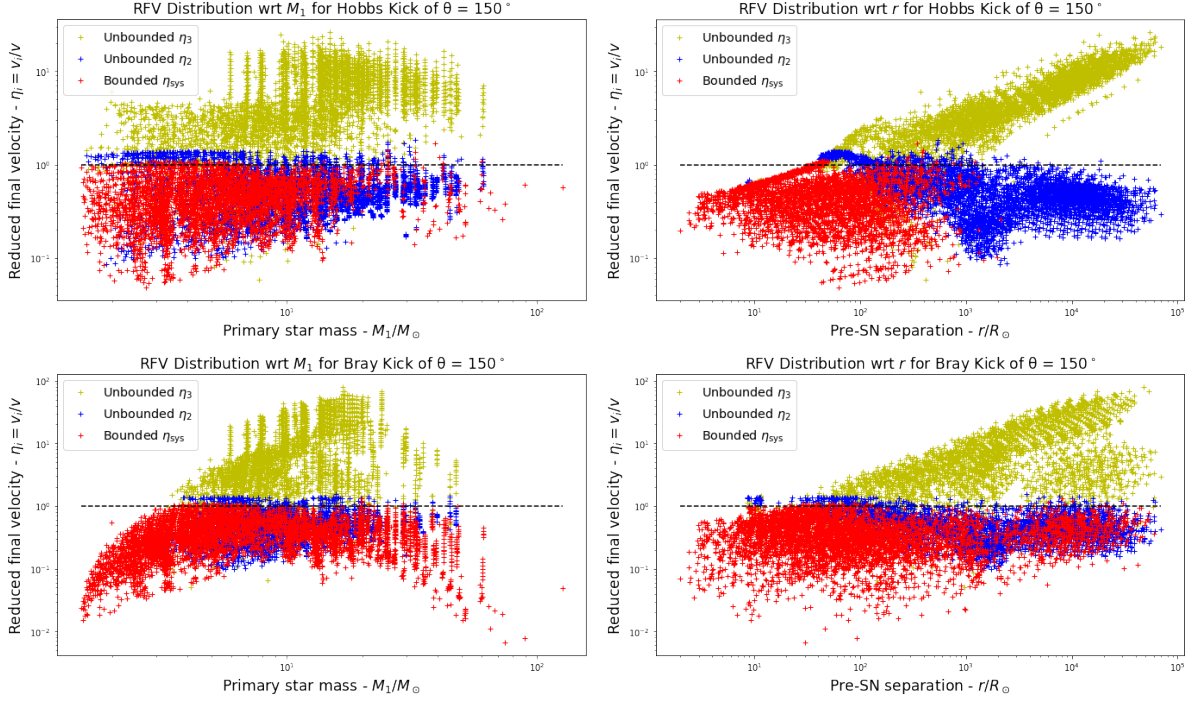


Figure C.21: $\mathcal{R}_H = 43.95\%$ and $\mathcal{R}_B = 35.83\%$. General patterns remain from previous one. Companion velocities (blue) keep slightly decreasing in general.

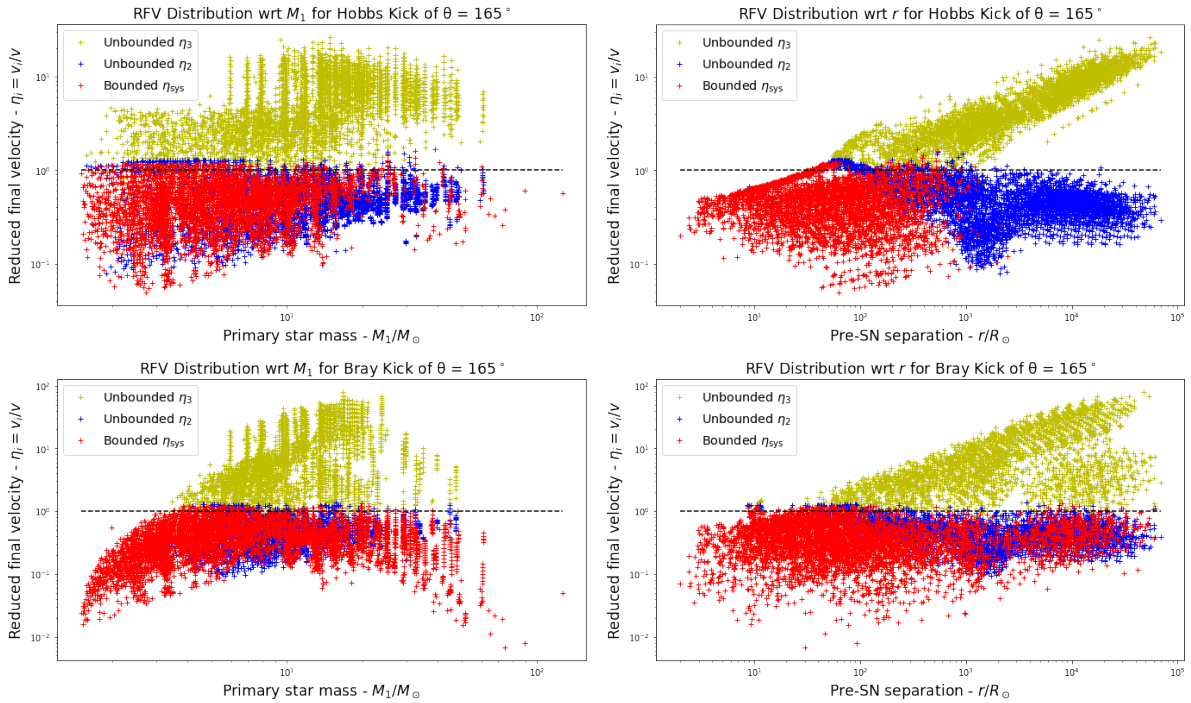


Figure C.22: $\mathcal{R}_H = 40.31\%$ and $\mathcal{R}_B = 33.13\%$. General patterns remain. Less companion velocities (blue) but more systematic velocities (red) beyond the pre-SN unit line (black dashed).

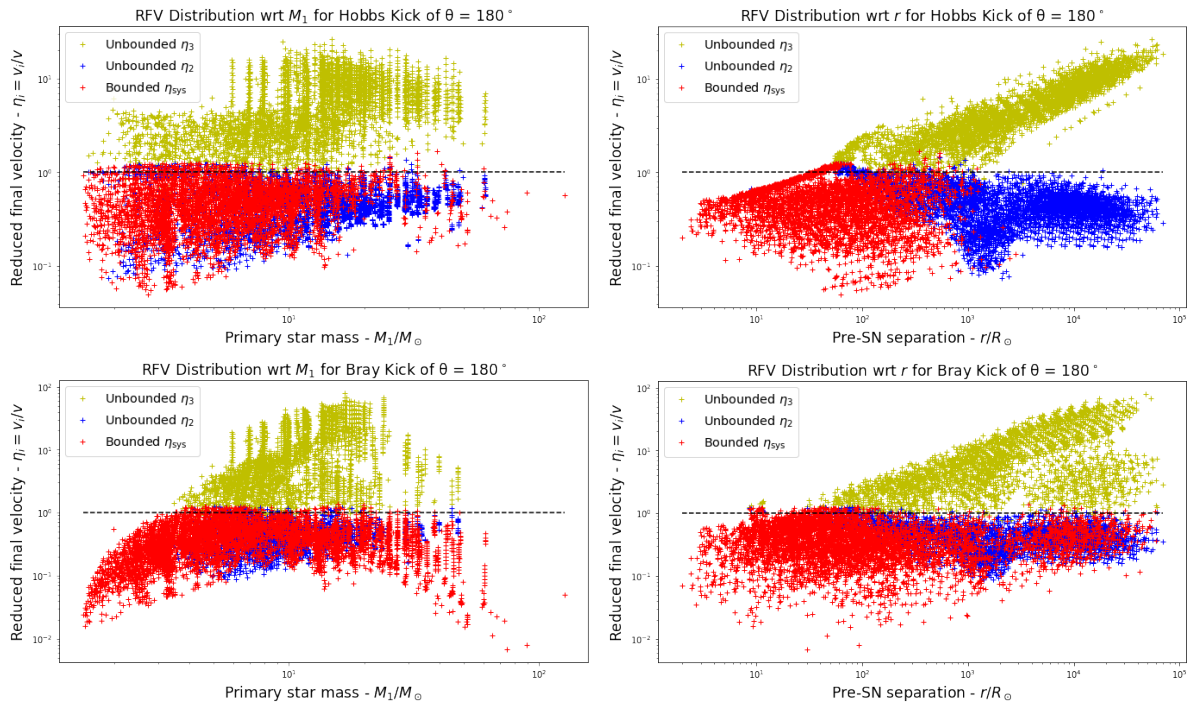


Figure C.23: $\mathcal{R}_H = 39.33\%$ and $\mathcal{R}_B = 32.23\%$. General patterns remain. At this stage, we can confirm that only systems with lower pre-SN separation can survive in a Hobbs' kick, but this conclusion gets much weaker for a Bray's kick.

Appendix D

Full Results of GW Archaeology

In the final appendix, we tabulate all matching results of our prototype for gravitational wave (GW) archaeology. As we explain in Section 3.2.2, due to limitation of time available to this project, we only progress detailed investigation for the version 2 and version 3 gravitational wave transients from GWTC [16]. For the majority of detection, which are of version 1, we list their best matches in the landscape tables.

We have investigated 90 GW events, seven version 3 events, five version 2 events, and the rest of them are version 1. In summary, 87 events were successfully matched in the BPASS population, where each one of the three version were unsuccessful. In particular, GW170817 (version 3) and GW190814 (version 2) were only successfully matched with a weaker time constraint, for which we remove the upper bound of the look-back time. GW191219_163120 (version 1) were unable to match, since its $M_b = 1.17^{+0.07}_{-0.06} M_\odot$, with upper bound even lower than the minimum neutron star mass predicted by the BPASS model, $\sim 1.259 M_\odot$.

We tabulate the matching results for version 2 and version 3 transients separately, while for version 1 we delete several columns that are not strongly relevant and put all of them in a long landscape table. If an event name in the table caption is marked with an asterisk ‘*’, then it means this result is achieved by a weaker time constraint. The most significant values are matching renormalised weight (RNW), recall these are measures of confidence of our matching results. In the table, binary RNW is the probability of this theoretical system being the original binary stars of the detected transient, and kick RNW is the probability of the following kick being “the kick” to lead to the detection. For other values, all masses are in units of solar masses M_\odot , all orbital periods are in units of days, all cosmic-level time are in units of million years, all velocities are in units of kilometers per second, angles are in units of degree. Particularly, luminosity distances d_L are in Mega parsec, orbital separations r are in solar radii R_\odot , while eccentricities e are dimensionless.

Due to the width limit of the landscape table, we remove several columns of the original tables of version 2 & 3 ones:

- We delete the luminosity distance, since its directly useful and comparable equivalence is the look-back time, which we have presented.
- We also remove the evolution age t_{evo} , since its contribution has already been included in the GW permissible time τ .
- The IMF weight is also taken, since its combined weight is the Binary RNW. Note that, we also shorten the name of the Binary RNW to “B” in the landscape table, for saving spaces.

For conciseness, we also simplified the kick parameters into single values for these version 1 results. For the kick magnitude w , θ and resulting τ , we transfer their values into their weighted mean, so now all these three values are statistically average values, as representatives of the kick. After this, we proceed a further column deletion:

- Since now all kick parameters are mean values, the Kick RNW is no longer important, we can safely remove it.
- As we emphasised in Section 3.1.1 and 3.1.2, several results suggest that ϕ^* are not significant in the final configuration. Hence, we delete the ϕ^* column.
- The patterns of eccentricities can be found in Section 3.1.2, and the final eccentricity was also a significant parameter in the gravitational decay time, which is already contained in τ . So we also remove the eccentricity column in landscape tables.

Furthermore, some transients can only be fitted by the theoretical system with a single certain kick, but some of them can survive for lots of kick combinations. We present the result by separate kick parameters for the first 12 tables, if the kick RNW is 100%, then it simply means only this kick coincides the detection. While for events like GW190521, they can have many possible suitable combinations of kick parameters. For the final landscape table, you can still distinguish between these two kinds of result by inspecting their w and θ columns. If both of these two values are the integer-like values that we set up in Section 2.5.3, for instance $w = 265$ km/s and $\theta = 138.6^\circ$, then it is very likely this is the only possible combination of kick parameters to give rise to that GW event.

Table D.1: GW Archaeology Match Result for GW150914

Event name	Version	$M_a (M_\odot)$	$M_b (M_\odot)$	d_L (Mpc)	t_{LB} (Myr)
GW150914	3	$35.6^{+4.7}_{-3.1}$	$30.6^{+3.0}_{-4.4}$	440^{+150}_{-170}	1256^{+363}_{-447}
Binary RNW (%)	$M_1 (M_\odot)$	$M_2 (M_\odot)$	$M_3 (M_\odot)$	$r (R_\odot)$	t_{evo} (Myr)
78.28	41.34	27.25	35.76	172.52	2.87
IMF weight	$M_{1,i} (M_\odot)$	$M_{2,i} (M_\odot)$	P_i (day)	P (day)	Z
0.090	150.0	10.0	63.21	31.74	0.008
Kick RNW (%)	w (km/s)	θ	ϕ^*	e	τ (Myr)
100.0	397.5	180°	-	0.785	898.50

Table D.2: GW Archaeology Match Result for GW151012

Event name	Version	$M_a (M_\odot)$	$M_b (M_\odot)$	d_L (Mpc)	t_{LB} (Myr)
GW151012	3	$23.2^{+14.9}_{-5.5}$	$13.6^{+4.1}_{-4.8}$	1080^{+550}_{-490}	2641^{+930}_{-1022}
Binary RNW (%)	$M_1 (M_\odot)$	$M_2 (M_\odot)$	$M_3 (M_\odot)$	$r (R_\odot)$	t_{evo} (Myr)
18.39	17.53	22.37	11.61	100.05	5.53
IMF weight	$M_{1,i} (M_\odot)$	$M_{2,i} (M_\odot)$	P_i (day)	P (day)	Z
0.396	40.0	19.95	39.88	18.38	0.002
Kick RNW (%)	w (km/s)	θ	ϕ^*	e	τ (Myr)
100.0	397.5	180°	-	0.771	2412.05

Table D.3: GW Archaeology Match Result for GW170608

Event name	Version	$M_a (M_\odot)$	$M_b (M_\odot)$	d_L (Mpc)	t_{LB} (Myr)
GW170608	3	$11.0^{+5.5}_{-1.7}$	$7.6^{+1.4}_{-2.2}$	320^{+120}_{-110}	945^{+311}_{-304}
Binary RNW (%)	$M_1 (M_\odot)$	$M_2 (M_\odot)$	$M_3 (M_\odot)$	$r (R_\odot)$	t_{evo} (Myr)
33.66	12.69	13.62	5.58	119.08	6.97
IMF weight	$M_{1,i} (M_\odot)$	$M_{2,i} (M_\odot)$	P_i (day)	P (day)	Z
0.395	30.0	12.59	39.88	29.39	0.003
Kick RNW (%)	w (km/s)	θ	ϕ^*	e	τ (Myr)
100.0	265.0	180°	-	0.884	754.05

Table D.4: GW Archaeology Match Result for GW170814

Event name	Version	$M_a (M_\odot)$	$M_b (M_\odot)$	$d_L (\text{Mpc})$	$t_{\text{LB}} (\text{Myr})$
GW170814	3	$30.6^{+5.6}_{-3.0}$	$25.2^{+2.8}_{-4.0}$	600^{+150}_{-220}	1642^{+335}_{-539}
Binary RNW (%)	$M_1 (M_\odot)$	$M_2 (M_\odot)$	$M_3 (M_\odot)$	$r (R_\odot)$	$t_{\text{evo}} (\text{Myr})$
77.08	30.68	27.69	24.61	344.35	3.08
IMF weight	$M_{1,i} (M_\odot)$	$M_{2,i} (M_\odot)$	$P_i (\text{day})$	$P (\text{day})$	Z
0.0394	120.0	12.59	100.18	97.01	0.01
Kick RNW (%)	$w (\text{km/s})$	θ	ϕ^*	e	$\tau (\text{Myr})$
100.0	132.5	180°	-	0.923	1474.26

Table D.5: GW Archaeology Match Result for GW170817*

Event name	Version	$M_a (M_\odot)$	$M_b (M_\odot)$	$d_L (\text{Mpc})$	$t_{\text{LB}} (\text{Myr})$
GW170817	3	$1.46^{+0.12}_{-0.1}$	$1.27^{+0.09}_{-0.09}$	40^{+7}_{-15}	129^{+22}_{-48}
Binary RNW (%)	$M_1 (M_\odot)$	$M_2 (M_\odot)$	$M_3 (M_\odot)$	$r (R_\odot)$	$t_{\text{evo}} (\text{Myr})$
100.0	11.72	1.34	1.46	31.66	6.97
IMF weight	$M_{1,i} (M_\odot)$	$M_{2,i} (M_\odot)$	$P_i (\text{day})$	$P (\text{day})$	Z
0.0718	30.0	1.26	10.02	5.72	0.003
Kick RNW (%)	$w (\text{km/s})$	θ	ϕ^*	e	$\tau (\text{Myr})$
100.0	265.0	180°	-	0.986	9747.01

Table D.6: GW Archaeology Match Result for GW190412

Event name	Version	$M_a (M_\odot)$	$M_b (M_\odot)$	$d_L (\text{Mpc})$	$t_{\text{LB}} (\text{Myr})$
GW190412	3	$30.1^{+4.7}_{-5.1}$	$8.3^{+1.6}_{-0.9}$	740^{+140}_{-170}	1956^{+294}_{-384}
Binary RNW (%)	$M_1 (M_\odot)$	$M_2 (M_\odot)$	$M_3 (M_\odot)$	$r (R_\odot)$	$t_{\text{evo}} (\text{Myr})$
77.93	15.64	34.19	9.23	108.81	6.16
IMF weight	$M_{1,i} (M_\odot)$	$M_{2,i} (M_\odot)$	$P_i (\text{day})$	$P (\text{day})$	Z
0.448	35.0	31.62	39.88	18.65	0.001
Kick RNW (%)	$w (\text{km/s})$	θ	ϕ^*	e	$\tau (\text{Myr})$
100.0	397.5	138.6°	30°	0.867	2053.72

Table D.7: GW Archaeology Match Result for GW190521

Event name	Version	$M_a (M_\odot)$	$M_b (M_\odot)$	d_L (Mpc)	t_{LB} (Myr)
GW190521	3	$95.3^{+28.7}_{-18.9}$	$69.0^{+22.7}_{-23.1}$	3920^{+2190}_{-1950}	6125^{+1462}_{-2063}
Binary RNW (%)	$M_1 (M_\odot)$	$M_2 (M_\odot)$	$M_3 (M_\odot)$	$r (R_\odot)$	t_{evo} (Myr)
35.36	50.59	86.47	47.97	77.38	2.68
IMF weight	$M_{1,i} (M_\odot)$	$M_{2,i} (M_\odot)$	P_i (day)	P (day)	Z
0.170	200.0	31.62	15.88	6.74	0.002
Kick RNW (%)	w (km/s)	θ	ϕ^*	e	τ (Myr)
16.78	397.5	104.5°	$0^\circ, 30^\circ$	~ 0.595	~ 5931.2
16.78	397.5	120.0°	$60^\circ, 90^\circ$	~ 0.293	~ 6635.4
13.92	265.0	104.5°	$0^\circ, 30^\circ$	~ 0.416	~ 5023.1
13.92	265.0	120.0°	$60^\circ, 90^\circ$	~ 0.278	~ 6835.8
12.73	132.5	120.0°	all	~ 0.217	~ 5484.4
12.73	132.5	138.6°	all	~ 0.301	~ 7368.2
5.70	530.0	120.0°	60°	0.416	6065.70
3.58	662.5	104.5°	0°	0.936	7482.85
2.51	662.5	120.0°	45°	0.663	7113.92
1.34	795.0	138.6°	90°	0.164	5192.45

Table D.8: GW Archaeology Match Result for GW151226

Event name	Version	$M_a (M_\odot)$	$M_b (M_\odot)$	d_L (Mpc)	t_{LB} (Myr)
GW151226	2	$13.7^{+8.8}_{-3.2}$	$7.7^{+2.2}_{-2.5}$	450^{+180}_{-190}	1281^{+430}_{-500}
Binary RNW (%)	$M_1 (M_\odot)$	$M_2 (M_\odot)$	$M_3 (M_\odot)$	$r (R_\odot)$	t_{evo} (Myr)
22.55	11.69	16.78	5.24	178.04	6.96
IMF weight	$M_{1,i} (M_\odot)$	$M_{2,i} (M_\odot)$	P_i (day)	P (day)	Z
0.827	30.0	15.85	63.21	51.65	0.004
Kick RNW (%)	w (km/s)	θ	ϕ^*	e	τ (Myr)
100.0	132.5	180°	-	0.925	1662.80

Table D.9: GW Archaeology Match Result for GW170104

Event name	Version	$M_a (M_\odot)$	$M_b (M_\odot)$	d_L (Mpc)	t_{LB} (Myr)
GW170104	2	$30.8^{+7.3}_{-5.6}$	$20.0^{+4.9}_{-4.6}$	990^{+440}_{-430}	2469^{+785}_{-920}
Binary RNW (%)	$M_1 (M_\odot)$	$M_2 (M_\odot)$	$M_3 (M_\odot)$	$r (R_\odot)$	t_{evo} (Myr)
23.19	26.95	26.34	20.69	1260.08	3.30
IMF weight	$M_{1,i} (M_\odot)$	$M_{2,i} (M_\odot)$	P_i (day)	P (day)	Z
0.0516	100.0	15.85	398.84	710.72	0.008
Kick RNW (%)	w (km/s)	θ	ϕ^*	e	τ (Myr)
100.0	132.5	138.6°	0°	0.994	2615.57

Table D.10: GW Archaeology Match Result for GW190425

Event name	Version	$M_a (M_\odot)$	$M_b (M_\odot)$	$d_L (\text{Mpc})$	$t_{\text{LB}} (\text{Myr})$
GW190425	2	$2.0^{+0.6}_{-0.3}$	$1.4^{+0.3}_{-0.3}$	160^{+70}_{-70}	495^{+202}_{-210}
Binary RNW (%)	$M_1 (M_\odot)$	$M_2 (M_\odot)$	$M_3 (M_\odot)$	$r (R_\odot)$	$t_{\text{evo}} (\text{Myr})$
7.28	6.24	2.02	1.47	3.54	54.58
IMF weight	$M_{1,i} (M_\odot)$	$M_{2,i} (M_\odot)$	$P_i (\text{day})$	$P (\text{day})$	Z
3.418	10.0	1.4	1.1	0.29	0.02
Kick RNW (%)	$w (\text{km/s})$	θ	ϕ^*	e	$\tau (\text{Myr})$
100.0	265.0	138.6°	30°	0.436	606.07

Table D.11: GW Archaeology Match Result for GW190814*

Event name	Version	$M_a (M_\odot)$	$M_b (M_\odot)$	$d_L (\text{Mpc})$	$t_{\text{LB}} (\text{Myr})$
GW190814	2	$23.2^{+1.1}_{-1.0}$	$2.59^{+0.08}_{-0.09}$	240^{+40}_{-50}	725^{+111}_{-142}
Binary RNW (%)	$M_1 (M_\odot)$	$M_2 (M_\odot)$	$M_3 (M_\odot)$	$r (R_\odot)$	$t_{\text{evo}} (\text{Myr})$
95.46	9.37	23.56	2.53	40.8	4.70
IMF weight	$M_{1,i} (M_\odot)$	$M_{2,i} (M_\odot)$	$P_i (\text{day})$	$P (\text{day})$	Z
0.0389	50.0	6.31	15.88	5.27	0.014
Kick RNW (%)	$w (\text{km/s})$	θ	ϕ^*	e	$\tau (\text{Myr})$
100.0	397.5	138.6°	45°	0.718	1210.03

Table D.12: GW Archaeology Match Result for GW200115_042309

Event name	Version	$M_a (M_\odot)$	$M_b (M_\odot)$	$d_L (\text{Mpc})$	$t_{\text{LB}} (\text{Myr})$
GW200115_042309	2	$5.9^{+2.0}_{-2.5}$	$1.44^{+0.85}_{-0.29}$	290^{+150}_{-100}	863^{+393}_{-281}
Binary RNW (%)	$M_1 (M_\odot)$	$M_2 (M_\odot)$	$M_3 (M_\odot)$	$r (R_\odot)$	$t_{\text{evo}} (\text{Myr})$
2.53	3.02	4.26	1.45	7.06	20.17
IMF weight	$M_{1,i} (M_\odot)$	$M_{2,i} (M_\odot)$	$P_i (\text{day})$	$P (\text{day})$	Z
0.618	12.0	3.98	3.99	0.81	0.002
Kick RNW (%)	$w (\text{km/s})$	θ	ϕ^*	e	$\tau (\text{Myr})$
47.81	397.5	104.5°	0°	0.890	934.14
39.65	265.0	120.0°	90°	0.031	599.79
12.53	132.5	120.0°	30°	0.252	1243.48

Table D.13: GW Archaeology Match Result for All Version 1 Events

Event name	M_a	M_b	t_{LB}	B	M_1	M_2	M_3	r	P	Z	w	θ (°)	τ	$M_{1,i}$	$M_{2,i}$	P_i
GW170729	50.2 ^{+16.2} _{-10.2}	34.0 ^{+9.1} _{-10.1}	51.12 ⁺¹²⁶⁸ ₋₁₇₇₇	23.06	48.5	41.64	43.81	92.87	10.9	0.004	322.4	136.1	4411	150	25.12	39.9
GW170809	35.0 ^{+8.3} _{-5.9}	23.8 ^{+5.1} _{-5.2}	2546 ⁺⁵⁷⁵ ₋₈₁₂	48.74	41.34	27.25	35.76	172.5	31.7	0.008	265.0	138.6	2392	150	10	63.2
GW170818	35.4 ^{+7.5} _{-4.7}	26.7 ^{+4.3} _{-5.2}	2603 ⁺⁷³² ₋₇₇₉	46.07	41.34	27.25	35.76	172.5	31.7	0.008	265.0	138.6	2392	150	10	63.2
GW170823	39.5 ^{+11.2} _{-6.7}	29.0 ^{+6.7} _{-7.8}	4021 ⁺¹¹⁶⁵ ₋₁₄₅₆	22.27	28.85	43.52	22.58	87.73	11.2	0.006	337.4	138.6	3263	100	15.85	25.2
GW190403_051519	88.0 ^{+28.2} _{-32.9}	22.1 ^{+23.8} _{-9.0}	8470 ⁺²⁵²⁷ ₋₂₂₇₂	12.14	47.13	77.76	44.21	59.62	4.78	0.003	410.1	134.3	8870	200	19.95	25.2
GW190408_181802	24.6 ^{+5.1} _{-3.4}	18.4 ^{+3.3} _{-3.6}	3446 ⁺⁵⁸⁸ ₋₁₀₅₆	73.78	26.93	25.51	20.66	326.2	94.4	0.008	132.5	180	3751	100	19.95	63.2
GW190413_052954	34.7 ^{+12.6} _{-8.1}	23.7 ^{+7.3} _{-6.7}	5806 ⁺¹⁶¹⁹ ₋₁₈₅₅	9.42	25.28	44.42	19.45	510.5	160	0.01	132.5	180	6546	100	25.12	100
GW190413_134308	47.5 ^{+13.5} _{-10.7}	31.8 ^{+11.7} _{-10.8}	6358 ⁺¹⁴⁶⁴ ₋₂₀₁₀	8.87	48.5	41.64	43.81	92.87	10.9	0.004	325.2	138.6	6805	150	25.12	39.9
GW190421_213856	41.3 ^{+10.4} _{-6.9}	31.9 ^{+8.0} _{-8.8}	5155 ⁺¹²³³ ₋₁₇₈₇	19.29	43.82	49.34	38.43	103.8	12.7	0.006	453.5	147.9	5776	150	15.85	39.9
GW190426_190642	106.9 ^{+41.6} _{-25.2}	76.6 ^{+26.2} _{-33.6}	6464 ⁺¹⁸⁸³ ₋₂₀₉₈	29.21	50.59	86.47	47.97	77.38	6.74	0.002	345.8	117.4	6681	200	31.62	15.9
GW190503_185404	43.3 ^{+9.2} _{-8.1}	28.4 ^{+7.7} _{-8.0}	3287 ⁺¹⁰⁰² ₋₁₁₆₀	35.18	28.85	43.52	22.58	87.73	11.2	0.006	387.2	138.6	3075	100	15.85	25.2
GW190512_180714	23.3 ^{+5.3} _{-5.8}	12.6 ^{+3.6} _{-2.5}	3254 ⁺⁸²² ₋₁₀₀₄	38.58	17.53	22.37	11.61	100.1	18.4	0.002	365.8	170.1	2690	40	19.95	39.9
GW190513_205428	35.7 ^{+9.5} _{-9.2}	18.0 ^{+7.7} _{-4.1}	4184 ⁺¹⁰³⁴ ₋₁₂₁₇	21.79	28.85	43.52	22.58	87.73	11.2	0.006	337.4	138.6	3263	100	15.85	25.2
GW190514_065416	39.0 ^{+14.7} _{-8.2}	28.4 ^{+9.3} _{-8.8}	6294 ⁺¹⁶³⁶ ₋₂₂₄₆	11.82	39.21	42.0	34.59	118.4	16.6	0.004	373.7	133.4	6562	120	19.95	25.2
GW190517_055101	37.4 ^{+11.7} _{-7.6}	25.3 ^{+7.0} _{-7.3}	3909 ⁺¹⁸³⁴ ₋₁₃₈₂	21.84	28.85	43.52	22.58	87.73	11.2	0.006	360.1	138.6	3594	100	15.85	25.2
GW190519_153544	66.0 ^{+10.7} _{-12.0}	40.5 ^{+11.0} _{-11.1}	4767 ⁺¹⁷⁰⁴ ₋₁₂₂₇	15.03	48.68	70.51	44.05	185.9	26.9	0.004	482.2	163.6	5225	150	31.62	39.9
GW190521_074359	42.2 ^{+5.9} _{-4.8}	32.8 ^{+5.4} _{-6.4}	2931 ⁺⁶⁵⁵ ₋₁₁₃₀	70.66	34.58	44.21	28.84	95.2	12.1	0.006	580.2	138.6	2742	150	15.85	25.2
GW190527_092055	36.5 ^{+16.4} _{-9.0}	22.6 ^{+10.5} _{-8.1}	4721 ⁺²¹⁸² ₋₁₇₇₂	8.5	25.28	44.42	19.45	510.5	160	0.01	132.5	180	6546	100	25.12	100
GW190602_175927	69.1 ^{+15.7} _{-13.0}	47.8 ^{+14.3} _{-17.4}	4949 ⁺¹⁶¹¹ ₋₁₄₇₁	20.19	47.13	77.76	44.21	59.62	4.78	0.003	283.7	100.7	5129	200	19.95	25.2
GW190620_030421	57.1 ^{+16.0} _{-12.7}	35.5 ^{+12.2} _{-12.3}	5080 ⁺¹⁴⁸⁸ ₋₁₇₁₃	9.29	43.97	49.08	38.55	141.6	20.3	0.006	454.7	157.2	5544	150	15.85	63.2
GW190630_185205	35.1 ^{+6.9} _{-5.6}	23.7 ^{+5.2} _{-5.1}	2270 ⁺¹⁰¹⁶ ₋₈₁₇	45.76	41.34	27.25	35.76	172.5	31.7	0.008	265.0	138.6	2392	150	10	63.2
GW190701_203306	53.9 ^{+11.8} _{-8.0}	40.8 ^{+8.7} _{-12.0}	4184 ⁺⁹⁰⁷ ₋₁₀₉₇	10.05	47.02	55.95	42.2	69.87	6.68	0.004	353.3	115.5	4241	150	25.12	63.2

Event name	M_a	M_b	t_{LB}	B	M_1	M_2	M_3	r	P	Z	w	$\theta(^{\circ})$	τ	$M_{1,i}$	$M_{2,i}$	P_i
GW190706_222641	67.0 ^{+14.6} _{-16.2}	38.2 ^{+14.6} _{-13.3}	65.16 ⁺¹⁵²⁴ ₋₁₇₉₅	11.03	47.13	77.76	44.21	59.62	4.78	0.003	317.3	108.5	6609	200	19.95	25.2
GW190707_093326	11.6 ^{+3.3} _{-1.7}	8.4 ^{+1.4} _{-1.7}	2020 ⁺⁷⁵⁰ ₋₈₆₆	28.87	13.26	10.12	6.82	49.17	8.27	0.004	337.4	138.6	1830	40	10	25.2
GW190708_232457	17.6 ^{+4.7} _{-2.3}	13.2 ^{+2.0} _{-2.7}	2250 ⁺⁶²⁸ ₋₈₇₀	65.46	19.06	16.4	12.06	87.57	16.0	0.003	365.8	170.1	2482	50	15.85	39.9
GW190719_215514	36.5 ^{+18.0} _{-10.3}	20.8 ^{+9.0} _{-7.2}	6141 ⁺¹⁶⁶⁵ ₋₂₁₂₀	8.27	28.7	54.36	22.65	198.1	35.5	0.006	397.5	161.1	5559	100	25.12	39.9
GW190720_000836	13.4 ^{+6.7} _{-3.0}	7.8 ^{+2.3} _{-2.2}	2063 ⁺¹²⁷² ₋₇₃₂	17.61	12.55	17.56	5.69	63.13	10.6	0.002	337.4	138.6	1858	30	15.85	25.2
GW190725_174728	11.5 ^{+6.2} _{-2.7}	6.4 ^{+2.0} _{-2.0}	2584 ⁺⁹⁷¹ ₋₉₆₅	8.95	11.26	10.1	4.91	94.67	23.1	0.008	265.0	180	2740	40	10	63.2
GW190727_060333	38.0 ^{+9.5} _{-6.2}	29.4 ^{+7.1} _{-8.4}	5576 ⁺¹²³⁹ ₋₁₇₅₂	17.57	44.97	25.21	42.28	144.6	24.1	0.004	337.4	138.6	6345	150	25.12	25.2
GW190728_064510	12.3 ^{+7.2} _{-2.2}	8.1 ^{+1.7} _{-2.6}	2230 ⁺⁵⁰⁴ ₋₈₂₅	22.74	12.55	17.56	5.69	63.13	10.6	0.002	337.4	138.6	1858	30	15.85	25.2
GW190731_140936	41.5 ^{+12.2} _{-9.0}	28.8 ^{+9.7} _{-9.5}	5576 ⁺¹⁷⁷⁵ ₋₂₀₈₂	11.13	43.82	49.34	38.43	103.8	12.7	0.006	436.3	146.2	6041	150	15.85	39.9
GW190803_022701	37.3 ^{+10.6} _{-7.0}	27.3 ^{+7.8} _{-8.2}	5547 ⁺¹⁵¹⁸ ₋₁₈₈₆	13.64	39.21	42.0	34.59	118.4	16.6	0.004	364.4	138.6	6036	120	19.95	25.2
GW190805_211137	48.2 ^{+17.5} _{-12.5}	32.0 ^{+13.4} _{-11.4}	7122 ⁺¹⁸⁶⁵ ₋₂₅₅₆	6.48	44.3	51.97	39.06	193.7	31.9	0.006	395.7	151.4	8054	150	19.95	63.2
GW190828_063405	32.1 ^{+5.8} _{-4.0}	26.2 ^{+4.6} _{-4.8}	4276 ⁺⁷⁸³ ₋₁₄₁₅	49.96	41.5	26.51	35.91	245.0	53.9	0.008	397.5	138.6	3508	150	10	100
GW190828_065509	24.1 ^{+7.0} _{-7.2}	10.2 ^{+3.6} _{-2.1}	3524 ⁺⁸⁶⁷ ₋₁₀₃₆	18.32	17.93	23.34	11.98	189.3	47.0	0.002	265.0	180	3937	40	19.95	100
GW190910_112807	43.9 ^{+7.6} _{-6.1}	35.6 ^{+6.3} _{-7.2}	3303 ⁺¹⁴¹⁸ ₋₁₀₅₃	56.86	48.5	41.64	43.81	92.87	10.9	0.004	369.3	135.6	3778	150	25.12	39.9
GW190915_235702	35.3 ^{+9.5} _{-6.4}	24.4 ^{+5.6} _{-6.1}	3555 ⁺⁹⁷³ ₋₁₀₄₈	34.09	28.85	43.52	22.58	87.73	11.2	0.006	387.2	138.6	3075	100	15.85	25.2
GW190916_200658	44.3 ^{+21.2} _{-13.3}	23.9 ^{+12.7} _{-10.2}	6546 ⁺²⁰²⁴ ₋₂₅₂₅	5.63	39.21	42.0	34.59	118.4	16.6	0.004	401.0	146.7	7282	120	19.95	25.2
GW190917_114630	9.3 ^{+3.4} _{-4.4}	2.1 ^{+1.5} _{-0.5}	1912 ⁺⁶⁹¹ ₋₇₃₂	11.72	9.17	10.25	2.7	64.15	13.5	0.008	397.5	138.6	2163	30	10	39.9
GW190924_021846	8.9 ^{+7.0} _{-2.0}	5.0 ^{+1.4} _{-1.9}	1572 ⁺⁴⁹¹ ₋₅₄₈	14.46	11.09	8.07	4.55	29.58	4.26	0.003	397.5	120	1502	30	7.94	15.9
GW190925_232845	21.2 ^{+6.9} _{-3.1}	15.6 ^{+2.6} _{-3.6}	2351 ⁺⁷⁰² ₋₇₅₅	41.37	26.89	12.02	20.46	90.82	16.1	0.008	265.0	138.6	2631	100	10	25.2
GW190926_050336	39.8 ^{+20.6} _{-11.1}	23.2 ^{+10.8} _{-9.7}	6007 ⁺²⁰⁰⁴ ₋₂₂₁₃	4.88	28.7	54.36	22.65	198.1	35.5	0.006	397.5	161.1	5559	100	25.12	39.9
GW190929_012149	80.8 ^{+33.0} _{-33.2}	24.1 ^{+19.3} _{-10.6}	4276 ⁺³¹²⁷ ₋₁₆₃₅	12.0	40.51	79.8	36.05	115.3	13.1	0.003	336.6	136.6	4513	120	39.81	15.9
GW190930_133541	12.3 ^{+12.4} _{-2.3}	7.8 ^{+1.7} _{-3.3}	1999 ⁺⁷¹⁶ ₋₇₄₃	11.44	12.48	13.35	5.47	52.43	8.67	0.002	361.4	131.2	1973	30	12.59	25.2
GW191103_012549	11.8 ^{+6.2} _{-2.2}	7.9 ^{+1.7} _{-2.4}	2469 ⁺⁸⁸² ₋₁₀₁₆	18.6	12.55	17.56	5.69	63.13	10.6	0.002	337.4	138.6	1858	30	15.85	25.2

Event name	M_a	M_b	t_{LB}	B	M_1	M_2	M_3	r	P	Z	w	$\theta (\circ)$	τ	$M_{1,i}$	$M_{2,i}$	P_i
GW191105_143521	$10.7^{+3.7}_{-1.6}$	$7.7^{+1.4}_{-1.9}$	2770^{+723}_{-968}	14.19	14.73	12.83	8.73	29.0	3.45	0.004	309.8	138.0	2618	50	12.59	10
GW191109_010717	$65.0^{+11.0}_{-11.0}$	$47.0^{+15.0}_{-13.0}$	3018^{+1619}_{-1284}	17.07	43.56	73.08	40.07	121.2	14.3	0.003	330.5	135.8	3125	150	39.81	15.9
GW191113_071753	$29.0^{+12.0}_{-14.0}$	$5.9^{+4.4}_{-1.3}$	3154^{+1601}_{-1177}	7.51	15.03	35.72	8.73	53.08	6.3	0.001	309.8	142.6	2951	35	31.62	10
GW191126_115259	$12.1^{+5.5}_{-2.2}$	$8.3^{+1.9}_{-2.4}$	3555^{+1010}_{-1305}	7.78	13.56	10.43	7.56	342.4	150	0.006	132.5	167.0	3452	35	10	159
GW191127_050227	$53.0^{+47.0}_{-20.0}$	$24.0^{+17.0}_{-14.0}$	5670^{+2122}_{-2302}	6.63	40.51	79.8	36.05	115.3	13.1	0.003	353.1	138.9	5100	120	39.81	15.9
GW191129_134029	$10.7^{+4.1}_{-2.1}$	$6.7^{+1.5}_{-1.7}$	2063^{+521}_{-757}	35.18	12.48	13.35	5.47	52.43	8.67	0.002	361.4	131.2	1973	30	12.59	25.2
GW191204_110529	$27.3^{+11.0}_{-6.0}$	$19.3^{+5.6}_{-6.0}$	3823^{+1938}_{-1955}	40.58	26.91	25.67	20.63	236.8	58.3	0.008	265.0	180	4431	100	19.95	39.9
GW191204_171526	$11.9^{+3.3}_{-1.8}$	$8.2^{+1.4}_{-1.6}$	1757^{+411}_{-602}	40.56	13.26	10.12	6.82	49.17	8.27	0.004	337.4	138.6	1830	40	10	25.2
GW191215_223052	$24.9^{+7.1}_{-4.1}$	$18.1^{+3.8}_{-4.1}$	4007^{+1084}_{-1385}	36.83	26.91	25.67	20.63	236.8	58.3	0.008	265.0	180	4431	100	19.95	39.9
GW191216_213338	$12.1^{+4.6}_{-2.3}$	$7.7^{+1.6}_{-1.9}$	998^{+305}_{-358}	42.02	13.46	12.99	8.02	75.01	14.7	0.004	265.0	138.6	692	35	12.59	39.9
GW191222_033537	$45.1^{+10.9}_{-8.0}$	$34.7^{+9.3}_{-10.5}$	5279^{+1439}_{-2244}	22.02	48.5	41.64	43.81	92.87	10.9	0.004	322.4	136.1	4411	150	25.12	39.9
GW191230_180458	$49.4^{+14.0}_{-9.6}$	$37.0^{+11.0}_{-12.0}$	6426^{+1314}_{-1812}	8.58	49.3	59.49	44.63	161.1	22.7	0.004	450.3	151.1	7113	150	31.62	25.2
GW200112_155838	$35.6^{+6.7}_{-4.5}$	$28.3^{+4.4}_{-5.9}$	2949^{+698}_{-886}	39.43	41.5	26.51	35.91	245.0	53.9	0.008	397.5	138.6	3508	150	10	100
GW200128_022011	$42.2^{+11.6}_{-8.1}$	$32.6^{+9.5}_{-9.5}$	5670^{+1568}_{-2145}	20.4	48.5	41.64	43.81	92.87	10.9	0.004	318.4	141.3	5180	150	25.12	39.9
GW200129_065458	$34.5^{+9.9}_{-3.2}$	$28.9^{+3.4}_{-9.3}$	2291^{+552}_{-838}	30.8	28.85	43.52	22.58	87.73	11.2	0.006	530	138.6	2535	100	15.85	25.2
GW200202_154313	$10.1^{+3.5}_{-1.4}$	$7.3^{+1.1}_{-1.7}$	1180^{+368}_{-427}	63.85	12.29	13.01	5.63	53.3	8.97	0.004	343.7	127.5	1334	35	12.59	25.2
GW200208_130117	$37.8^{+9.2}_{-6.2}$	$27.4^{+6.1}_{-7.4}$	4404^{+1104}_{-1233}	25.97	28.85	43.52	22.58	87.73	11.2	0.006	317.3	138.6	3861	100	15.85	25.2
GW200208_222617	$51.0^{+104.0}_{-30.0}$	$12.3^{+9.0}_{-5.7}$	6270^{+2394}_{-1904}	3.46	15.03	27.76	8.71	84.07	13.7	0.002	361.4	131.2	6254	35	25.12	25.2
GW200209_085452	$35.6^{+10.5}_{-6.8}$	$27.1^{+7.8}_{-7.8}$	5670^{+1446}_{-2145}	13.41	39.21	42.0	34.59	118.4	16.6	0.004	364.4	138.6	6036	120	19.95	25.2
GW200210_092254	$24.1^{+7.5}_{-4.6}$	$2.83^{+0.47}_{-0.42}$	2371^{+784}_{-729}	23.69	10.09	30.21	3.14	274.7	83.2	0.002	204.7	157.4	1818	24	25.12	100
GW200216_220804	$51.0^{+22.0}_{-13.0}$	$30.0^{+14.0}_{-16.0}$	6024^{+1916}_{-2201}	8.53	48.5	41.64	43.81	92.87	10.9	0.004	331.9	140.8	5607	150	25.12	39.9
GW200219_094415	$37.5^{+10.1}_{-6.9}$	$27.9^{+7.4}_{-8.4}$	5670^{+1318}_{-1704}	13.05	39.21	42.0	34.59	118.4	16.6	0.004	400.2	138.6	5683	120	19.95	25.2
GW200220_0611928	$87.0^{+40.0}_{-23.0}$	$61.0^{+26.0}_{-25.0}$	7527^{+1915}_{-2351}	13.68	47.13	77.76	44.21	59.62	4.78	0.003	348.4	119.4	8034	200	19.95	25.2

Event name	M_a	M_b	t_{LB}	B	M_1	M_2	M_3	r	P	Z	w	$\theta(^{\circ})$	τ	$M_{1,i}$	$M_{2,i}$	P_i
GW200220_124850	$38.9^{+14.1}_{-8.6}$	$27.9^{+9.2}_{-9.0}$	6190^{+1750}_{-2367}	10.21	39.21	42.0	34.59	118.4	16.6	0.004	373.7	133.4	6562	120	19.95	25.2
GW200224_222234	$40.0^{+6.9}_{-4.5}$	$32.5^{+5.0}_{-7.2}$	3691^{+675}_{-1069}	51.91	41.5	26.51	35.91	245.0	53.9	0.008	397.5	138.6	3508	150	10	100
GW200225_060421	$19.3^{+5.0}_{-3.0}$	$14.0^{+2.8}_{-3.5}$	2770^{+846}_{-1082}	31.99	17.53	22.37	11.61	100.1	18.4	0.002	365.8	170.1	2690	40	19.95	39.9
GW200302_015811	$37.8^{+8.7}_{-8.5}$	$20.0^{+8.1}_{-5.7}$	3335^{+1397}_{-1293}	28.87	28.85	43.52	22.58	87.73	11.2	0.006	387.2	138.6	3075	100	15.85	25.2
GW200306_093714	$28.3^{+17.1}_{-7.7}$	$14.8^{+6.5}_{-6.4}$	4236^{+1788}_{-1748}	10.92	15.03	35.72	8.73	53.08	6.3	0.001	277.8	147.5	3744	35	31.62	10
GW200308_173609	$36.4^{+11.2}_{-9.6}$	$13.8^{+7.2}_{-3.3}$	7177^{+1333}_{-2108}	8.65	19.23	28.46	12.39	53.08	6.5	0.01	409.8	153.8	7505	80	7.94	25.2
GW200311_115853	$34.2^{+6.4}_{-3.8}$	$27.7^{+4.1}_{-5.9}$	2806^{+480}_{-786}	63.63	41.34	27.25	35.76	172.5	31.7	0.008	265.0	138.6	2392	150	10	63.2
GW200316_215756	$13.1^{+10.2}_{-2.9}$	$7.8^{+1.9}_{-2.9}$	2715^{+794}_{-891}	10.97	12.48	13.35	5.47	52.43	8.67	0.002	397.5	128.4	2189	30	12.59	25.2
GW200322_091133	$34.0^{+48.0}_{-18.0}$	$14.0^{+16.8}_{-8.7}$	5851^{+3517}_{-2327}	2.77	12.56	55.93	5.88	58.45	6.26	0.001	378.2	137.9	6339	30	50.12	6.32